An Integrated Geophysical Approach to Investigating Thermal and Chemical Variations in Earth's Mantle

by

Ross Ronan Maguire

A dissertation submitted in partial fulfillment
of the requirements for the degree of
Doctor of Philosophy
(Earth and Environmental Sciences)
in the University of Michigan
2018

Doctoral Committee:

Professor Jeroen E. Ritsema, Chair
Associate Professor Brian K. Arbic
Associate Professor Jeremy N. Bassis
Associate Professor Eric A. Hetland
Adjunct Professor Peter E. van Keken

Ross R. Maguire
romaguir@umich.edu
ORCID ID: 0000-0002-0822-8849

ACKNOWLEDGMENTS

I would like to thank my advisers Jeroen Ritsema and Peter van Keken for all of their support and scientific training. Their guidance has contributed greatly to my professional development, and I consider myself lucky to have had the opportunity to work with both of them. I also thank my other committee members Eric Hetland, Jeremy Bassis, and Brian Arbic, who provided much valuable feedback on this dissertation. I have also been fortunate to have worked with excellent and inspiring scientific collaborators. I thank Andreas Fichtner (ETH Zürich) for hosting me at ETH and training me in the use of spectral element software for modeling seismic wave propagation. I also thank Mickaël Bonnin (University of Nantes), for teaching me about finite-frequency tomography during my visit to Nantes. Thanks to Saskia Goes (Imperial College London), who effectively served as an additional thesis advisor to me.

I have benefited from being part of a rich and lively geophysics research environment at the University of Michigan, and I learned much from discussions with fellow graduate students and postdocs. I would like to thank in particular, Sam Haugland, Carlos Chaves, and Trever Hines for valuable discussions.

I am grateful to my family and friends for all of their love and encouragement. Special thanks to my mom and dad, Mary and Ray Maguire, my brother Evin Maguire and his partner Jessica Tashman, my sister Alanna Maguire and my sister-in-law Dana Nessel, my nephews Alex and Zach Nessel, my mother-in-law and father-in-law Hannah and Jim Volk, my brother-in-law Charlie Volk and his partner Allison Simms, and my aunt and uncle Karen and Joe Tomczak. Last, but not least, I owe a debt of gratitude to my wife Kate who helped me persevere through my degree.

This research was enabled by National Science Foundation grants EAR-1246700 awarded to Peter van Keken and EAR-1565511 awarded to Jeroen Ritsema. Additionally, the Extreme Science and Engineering Discovery Environment (XSEDE) provided access to vital supercomputing resources.

TABLE OF CONTENTS

LIST OF FIGURES

LIST OF TABLES

ABSTRACT

The Earth's mantle is heterogeneous as a result of melting, differentiation, plate subduction, and whole-mantle convection throughout geologic time. Our current picture of the mantle has been informed largely by mapping variations in seismic wavespeed. However, it is challenging to infer the thermochemical nature of the mantle from seismic images because they are often poorly resolved, and velocity variations cannot be uniquely related to either temperature or composition.

In this thesis, I take a multi-disciplinary approach that combines constraints from geodynamics, mineral physics, and seismology, in order to investigate how thermal and compositional Earth models are compatible with seismic observations. I focus primarily on thermal upwellings (i.e., mantle plumes), and assess how these features can be seismically imaged. In chapter 2, I model plume development in a compressible mantle using physics-based simulations of flow in the mantle, and calculate the travel time delays of P waves and S waves propagating through the narrow plume tails in the lower mantle. In chapter 3, I investigate whether or not mantle plume tails can be seismically imaged using common seismic tomography approaches. I analyze how imaging artifacts can affect our interpretations of the deep mantle below hotspots and find optimal imaging configurations that will maximize resolution of plume tails. In chapter 4, I analyze images of the mantle beneath the Samoa hotspot in global tomography model S40RTS (Ritsema et al., 2011). Specifically, I explore the range of temperatures and compositions that can explain the observed seismic velocity variations and determine if observations are consistent with a lower mantle plume origin of Samoan volcanism. In chapter 5 I investigate the origin of large low velocity provinces (LLVPs) above the core-mantle-boundary beneath Africa and the Pacific, which are thought to be anomalously hot and compositionally distinct mantle domains. I test the hypothesis that the anomalies represent an accumulation of recycled oceanic crust above the core by comparing LLVPs resolved in S40RTS to dynamic mantle mixing simulations of Brandenburg et al. (2008). Chapter 6 focuses on how lateral variations of temperature and composition affect the seismic structure of the mantle transition zone (MTZ). I use P-to-S receiver functions to image the strengths and depths of mineralogical phase changes in the MTZ beneath the United States, and relate these observations to the physical conditions of the transition zone using constraints from experimental and theoretical mineral physics.

CHAPTER 1

Introduction

Heat from the Earth's interior drives solid state convection which dynamically stirs the mantle over geologic time. At the Earth's surface, plate tectonics is the primary expression of mantle convection. Many important geologic phenomena, such as mountain building, volcanism, and fault related earthquakes, result from the gradual motion of tectonic plates and processes occurring at their boundaries. Below the tectonic plates, where we can not make direct observations, we must rely on geophysical methods to understand the nature of convection.

One such method, called seismic tomography, has helped reveal fundamental aspects of mantle convection by mapping the variations in seismic wavespeed associated with changes in mantle temperature and composition. On a global scale, the field rapidly developed in the early 1980s (*Masters et al.*, 1982; *Nakanishi and Anderson*, 1982; *Woodhouse and Dziewonski*, 1984; *Dziewonski*, 1984) after the proliferation of digital global seismic networks. The earliest models showed coherent 1000-km scale heterogeneity related to plate tectonic processes in the upper mantle and sluggish convection in the lower mantle. As spatial resolution improved, tomographic images revealed ancient tectonic plates sinking into the lower mantle (*van der Hist et al.*, 1991; *Grand*, 1994), which helped settle the longstanding debate about whether the upper and lower mantle convect as separate layers, or if the mantle convects as a whole. Other studies show that the pattern of wavespeed variations changes abruptly from the upper to lower mantle (e.g., *Su et al.*, 1994), likely reflecting an increase in mantle viscosity with depth. This is supported by seismic images that show subducted tectonic plates stagnating in the transition zone or in the mid mantle (*Fukao et al.*, 2001; *Fukao and Obayashi*, 2013). Seismic tomography has also uncovered two broad regions of low seismic velocity above the core-mantle boundary beneath Africa and the Pacific ocean, which may represent upwellings of anomalously hot or chemically distinct mantle (e.g., *Dziewonski*, 1984; *Garnero et al.*, 2016).

Although tomographically mapping the Earth's interior has improved our understanding of mantle properties, as well as the nature of mantle convection, important gaps in our

knowledge remain. One topic of much debate concerns the ultimate origin of anomalous volcanism that does not fit the plate tectonic paradigm. This style of volcanism, referred to as 'hotspot volcanism', is characterized by melting within plate interiors (Hawaii for example), or excessive melt production at mid ocean ridges (Iceland for example). The growing consensus is that hotspot volcanism is driven by deep thermal upwellings known as mantle plumes but this idea is still challenged by some researchers, in large part due to the lack of conclusive seismic evidence of the presence of plumes (see *Ballmer et al.* (2015) for a review). Over the past several decades, continually improving seismic datasets and theoretical advances have allowed seismologists to map finer and finer details of deep Earth structure, yet definitive detection of lower mantle plumes has remained elusive.

1.0.1 Limitations of seismic tomography

Seismic tomography is one of the most powerful tools available to study the Earth's interior. Analogous to CAT-scans in medical imaging, wherein X-rays are used to map variations in tissue density, seismic tomography uses seismic waves from large earthquakes to map variations in shear and compressional wavespeeds in Earth's mantle. The 3D images of wavespeed variation reflect the temperature and composition of mantle rocks and can be used to infer mantle flow. However, unlike medical imaging, in seismic tomography we have no control over the location of seismic sources, and we are limited in the number of sensors at which wave energy is recorded. The lack of perfect seismic data coverage, as well as uncertainties on earthquake locations and seismic measurements, leads to an ill-posed tomographic inverse problem that has infinitely many solutions. Choosing a best model requires 'regularizing' the inversion, in which subjective choices are made about the model characteristics. Typically, the optimal model is chosen according the principle of parsimony, which suggests that the simplest model that is capable of explaining the data is best. In tomography this means choosing the model with the smallest anomalies or with the smoothest variations. While model regularization is necessary, it introduces artifacts into the tomographic image. For example, a side effect choosing smooth models is to artificially elongate or 'smear' seismic anomalies. Similarly, choosing the model with the smallest anomalies results in underestimating the strength of the wavespeed variations in the true Earth. The result is a blurred or distorted image which may misguide our understanding of the Earth's interior.

In addition to limitations that arise from the lack of seismic data and inversion regularization, tomographic models may suffer from bias introduced by the effects of wave diffraction. When a seismic wave encounters a region of anomalously fast or slow mantle,

the waves will accelerate or decelerate, respectively. A wave traveling directly through the anomaly will be recorded with either an early or late travel time, thus preserving the signature of the anomaly and allowing it to be imaged tomographically. However, if the size of the anomaly is small compared to the wavelength of the seismic wave, energy will diffract around the edges of the anomaly. If the diffracted energy interferes with the direct through-going wave, it can diminish or erase the travel time signature of the anomaly recorded at the seismic station. This effect, known as wavefront healing, may make imaging narrow plume tails in the lower mantle particularly challenging (e.g., *Hwang et al.*, 2011).

The development of more sophisticated tomographic imaging techniques, which attempt to correct for the effects of wave diffraction (e.g., *Dahlen et al.*, 2000; *Hung et al.*, 2000), may provide increased resolution of small scale seismic anomalies. *Montelli et al.* (2004) first applied this methodology, referred to as 'finite frequency tomography' to global imaging, and found evidence for whole mantle plumes beneath many prominent hotspots. This result is still under considerable debate, and it is not clear if finite frequency tomography improves image resolution over classical approaches (e.g., *Trampert and Spetzler*, 2006).

1.0.2 Research objectives

The primary research goal in this dissertation is to investigate the limitations of seismic tomography in resolving thermal and chemical anomalies in Earth's mantle, with a primary focus on mantle upwellings. My aim is to quantitatively assess the resolution that can be achieved in tomography, and analyze artifacts that are introduced by incomplete data coverage and inversion regularization. The analysis will help us understand when we can confidently interpret mantle heterogeneity, and how we can design future seismic experiments to attain optimal image resolution.

1.0.3 Integrated geophysical approach

A robust assessment of the limitations of imaging mantle heterogeneity requires a multi-disciplinary approach. It is necessary to i) predict the length scale and seismic velocity of dynamic features in the mantle, and ii) design hypothetical seismic experiments which quantify how features are recovered in seismic images. Here, I use an integrated approach that combines constraints from geodynamics, mineral physics, and seismology. I use numerical simulations of mantle flow to inform the temperature structure of dynamic features such as mantle plumes, and use experimental constraints on the relationship between temperature and the elastic properties of mantle rock to calculate velocity structure of the

dynamic Earth models. I design hypothesis tests to determine how dynamic Earth models would be seismically recovered with modern imaging techniques. To quantify the effects of mantle heterogeneity on seismic waves, I use a forward modeling approach in which I solve the elastic wave equation in 3D with the spectral element method.

1.0.4 Thesis outline

In Chapter 2 I investigate the P and S wave travel-time delay time signature of geodynamically predicted mantle plume structures using computer simulations of the 3D teleseismic wavefield. The temperature and seismic structure of the plumes are consistent with our current understanding of flow in the mantle and mineral physics constraints. Chapter 3 expands upon this forward modeling by using the travel time signatures of plumes to estimate how well deep mantle plume tails can be imaged with our current capabilities. I explore imaging scenarios comparable to both previously completed and recently proposed seismic experiments, as well as investigate how well plumes can be imaged under optimal scenarios. In Chapter 4, I analyze tomographic images of the Samoa hotspot as seen in the global tomography model S40RTS (*Ritsema et al.*, 2011). More specifically, I explore the range of temperatures and compositions that are consistent with the observed shear velocity anomaly, and use new insight to propose a model of the Samoa hotspot which is fed by a lower mantle plume. In Chapter 5, I investigate the nature of the large low velocity provinces observed beneath Africa and the Pacific, which are thought to be anomalously hot and compositionally distinct mantle domains, and which may be source regions of mantle plumes. I test the hypothesis that these features are piles of ancient oceanic crust that has been sequestered at the core-mantle boundary and reheated. The modeling is informed by global scale mantle mixing simulations which predict how the temperature and composition of the mantle evolves through geologic time. In Chapter 6, I focus on how thermal and chemical heterogeneity affects the seismic velocity structure of the transition zone, and how seismically imaging mineral phase transformations can inform us about the temperature and composition of the mantle. I analyze data from the USArray to image the transition zone beneath North America, and use synthetic tests based on 3D spectral element waveform simulations to investigate imaging artifacts.

CHAPTER 2

P and S wave delays caused by thermal plumes *

Abstract

Many studies have sought to seismically image plumes rising from the deep mantle in order to settle the debate about their presence and role in mantle dynamics, yet the predicted seismic signature of realistic plumes remains poorly understood. By combining numerical simulations of flow, mineral-physics constraints on the relationships between thermal anomalies and wave speeds, and spectral-element method based computations of seismograms, we estimate the delay times of teleseismic S and P waves caused by thermal plumes. Wavefront healing is incomplete for seismic periods ranging from 10 s (relevant in travel-time tomography) to 40 s (relevant in waveform tomography). We estimate P wave delays to be immeasurably small (< 0.3 s). S wave delays are larger than 0.4 s even for S waves crossing the conduits of the thinnest thermal plumes in our geodynamic models. At longer periods (> 20 s), measurements of instantaneous phase misfit may be more useful in resolving narrow plume conduits. To detect S wave delays of 0.4–0.8 s and the diagnostic frequency dependence imparted by plumes, it is key to minimize the influence of the heterogeneous crust and upper mantle. We argue that seismic imaging of plumes will advance significantly if data from wide-aperture ocean-bottom networks were available since, compared to continents, the oceanic crust and upper mantle is relatively simple.

2.1 Introduction

Hotspots (*Wilson*, 1963) and mantle plumes (*Morgan*, 1971) have been important concepts in global geophysical and geochemical research (*Ballmer et al.*, 2015) for more than half

*Chapter 2 is published in *Geophysical Journal International*: Maguire, R., Ritsema, J., van Keken, P. E., Fichtner, A., & Goes, S. (2016). P-and S-wave delays caused by thermal plumes. Geophysical Journal International, 206(2), 1169-1178.

a century. In the classical view, plumes begin as thermal instabilities at the core-mantle boundary (CMB) and rise rapidly through the mantle. The voluminous plume head erupts as flood basalts to form large igneous provinces. The narrow plume tail is a persistent source of volcanism with a relatively fixed mantle position.

While plumes explain broad topographic swells, geoid highs, and the distinct geochemistry of basalts at hotspots, the plume hypothesis has not been universally accepted. A number of hotspots may not require a deep mantle origin (e.g., *King and Ritsema*, 2000), and plumes in a heterogeneous mantle with chemical and phase changes are predicted to be more complex than plumes in the classical models (e.g., *Samuel and Farnetani*, 2003; *Ballmer et al.*, 2013; *Lin and van Keken*, 2006). Seismic images (e.g., *Bijwaard and Spakman*, 1999; *Montelli et al.*, 2004; *Allen et al.*, 2002; *Wolfe et al.*, 2009; *Styles et al.*, 2011; *French and Romanowicz*, 2015) and statistical analyses (*Boschi et al.*, 2007, 2008) suggest that several low-velocity anomalies are continuous from the top to the bottom of the mantle. In addition, mantle transition zone thinning has been observed beneath a number of hotspots (e.g., *Schmandt et al.*, 2012; *Shen et al.*, 1998), potentially indicating a thermal anomaly extending to the lower mantle. Yet, it remains controversial to associate the complex seismic observations and models uniquely to thermal plumes.

Several factors complicate the resolution of the seismic structure of the mantle beneath hotspots. First, most regional seismic networks, and especially those covering oceanic hotspots (i.e., Hawaii and Iceland), have limited aperture. The sparse wave-path coverage in the lower mantle leads to overwhelming seismic modeling artifacts. Second, the deceleration of waves traversing a plume tail may not be recorded at seismic stations on the surface due to the destructive interference of direct and diffracted waves (i.e., wavefront healing) (*Nolet and Dahlen*, 2000; *Malcolm and Trampert*, 2011). These diffractions, recorded in the coda of P and S waves (*Rickers et al.*, 2012), are weaker than the coda signals produced by scattering in the crust.

To make meaningful interpretations of seismic data and models, it is important to understand the expected imprint of plumes in waveforms. In this paper we estimate the delay times of S and P waves, which are principal observations used in traveltime tomography. We develop seismic models of plumes by combining numerical simulations of flow and mineral-physics constraints on the relationships between thermal anomalies and wave speeds. We use 3D spectral-element method (SEM) computations to synthesize teleseismic S- and P wave propagation through plumes at frequencies up to 0.1 Hz, which are relevant in body-wave analyses. This work builds on analyses of uniform cylindrical anomalies (*Rickers et al.*, 2012) and on analyses of 2.5D axisymmetric synthetics (*Hwang et al.*, 2011).

Our seismic models of axisymmetric plumes are based on plume ascent in a compressible mantle with an isochemical pyrolitic composition and with phase changes. We vary the strength and width of plumes by varying the dynamic parameters. The plume buoyancy fluxes are about 2×10^3 kg/s in the lower mantle, which are within the range of the fluxes inferred from hotspot swell topography (*Sleep*, 1990). It is likely that plumes in the Earth deviate substantially from our idealized numerical models due to, for example, entrainment of compositionally distinct material (e.g., *Lin and van Keken*, 2006; *Samuel and Bercovici*, 2006; *Kumagai et al.*, 2008) and the shearing by the overriding plate (*Ballmer et al.*, 2015). However, we focus primarily on the structure of the narrow, vertical plume conduit, whose seismic resolvability in the lower mantle is uncertain. Any deviation from an idealized vertical conduit due to large scale flow is unlikely to significantly alter the width of the plume tail, or the amplitude of the seismic anomaly.

2.2 Numerical simulations

2.2.1 Thermal plumes in a compressible mantle

We simulate plumes closely following *Bossmann and van Keken* (2013), in which we solve the equations governing conservation of mass, momentum, and energy as defined by the anelastic liquid approximation (*Jarvis and McKenzie*, 1980). The equations are discretized via the finite-element method and solved in an axisymmetric spherical shell. We use a staggered grid refinement scheme to optimize the computations. The smallest grid spacing of 2.85 km is necessary to resolve the high temperature gradients in the plume head. The bottom boundary is a free-slip surface with a fixed temperature of 3270 K. The side wall is insulating, and the top boundary is fixed at 273.15 K. Rigid boundaries at the top and side of the domain limit large-scale horizontal flow and emphasize plume development.

The initial adiabatic temperature profile (Figure 2.1) is determined using the Adams-Williamson equation of state. Estimates of the temperature increase across the superadiabatic thermal boundary layer above the CMB range from 500 K to 1,800 K (*Lay and Buffett*, 2008). We vary the temperature contrast, ΔT_{CMB}, across the basal thermal boundary layer between 550 and 750 K. The depth-dependent thermal expansivity, α, decreases by a factor of three from the Earth's surface to the CMB. A surface value of thermal expansivity, $\alpha_0 = 3 \times 10^5$ K^{-1} and specific heat, $c_p = 1250$ J/kgK yield a dissipation number Di = 0.679 for all plume models.

Viscosity, η, varies as a function of temperature T and depth z

$$\eta(T, z) = \eta(z)\, e^{-b(T-\bar{T})}. \tag{2.1}$$

A linearization of the Arrhenius viscosity law for diffusion creep with $\mathrm{E} = 300 \frac{\mathrm{kJ}}{\mathrm{mol}}$ (e.g., *Karato and Wu*, 1993) yields a viscosity reduction between one and three orders of magnitude over the range of plume excess temperatures we consider (i.e., $b = ln(10)$ to $b = ln(1000)$). The depth dependent viscosity prefactor $\eta(z)$ is given by three layers (Figure 2.1c). The viscosity in the lower mantle, η_3, is 10^{22} Pa s. A stiff upper layer of $\eta_1 = 100\,\eta_{\mathrm{LM}}$ simulates a 120-km thick lithosphere. The viscosity η_2 in the upper mantle is either η_3 or $\eta_3/30$.

Plumes are initiated by applying a cosine perturbation to the basal thermal boundary layer. The peak perturbation at the symmetry axis is equal to half of the temperature difference between the surface and the CMB. We vary the structure of plumes by modifying the radial viscosity profile, the temperature-dependence of rheology, the temperature contrast across the basal thermal boundary layer, and phase changes in the mantle transition zone. Plumes are broad in a mantle with relatively high viscosity and localized when rheology is strongly temperature dependent. The endothermic phase transition at the base of the mantle transition zone can inhibit plume ascent.

Phase functions describe the relative fraction of each mineral phase as a function of excess pressure at the 410-km and 660-km phase transitions. For models considering phase changes, we assume that the Clapeyron slopes of the olivine-wadsleyite phase change (Γ_{410}) and the ringwoodite-perovskite phase change (Γ_{660}) are +3.8 MPa/K and -2.5 MPa/K, respectively. The effects of latent heat on temperature are included in the reference temperature profile.

Plume excess temperature in the upper mantle inferred from OIB major-element geochemistry is expected to be in the range of 100–300 K (e.g., *Courtier et al.*, 2007). Here, plume models slightly exceed this range ($\sim$ 350–500 K) for the upper mantle. This is potentially due to a lack of lateral motion imposed by the axisymmetry constraint. It may also be an indication that plumes in the Earth carry a fraction of the heat from the CMB to the surface, potentially due to chemical stratification of a dense layer above the core (e.g., *Farnetani*, 1997). Stagnation just below the transition zone may also promote cooling (e.g., *Ballmer et al.*, 2015). Our models neglect latent heat loss due to melting, but this is likely a second order effect.

We calculate the buoyancy flux B by integrating the product of mass flux and thermal expansion due to the plume excess temperature over a spherical surface S with a radius of

10 degrees, centered on the plume axis.

$$B = \int \rho \alpha w (T - T_A) \, \mathrm{d}S \tag{2.2}$$

where ρ is density, α is thermal expansivity, w is the upward velocity, T_A is the adiabatic reference temperature. Further details are provided in *Bossmann and van Keken* (2013).

2.2.2 Seismic velocity conversion

The P-wave (V_P) and S-wave (V_S) velocity structure of the plume is determined using thermodynamic first principles. We assume a pyrolite mantle composition (*Workman and Hart*, 2005) and the elastic parameter database described in *Stixrude and Lithgow-Bertelloni* (2011) for the six oxides SiO_2, MgO, FeO, CaO, Al_2O_3, Na_2O. Mineral parameters in the database are calculated for a third-order, finite- strain equation of state with Mie-Grüneisen temperature correction. We use the Perple_X software (*Connolly*, 2005) to compute an equilibrium mineral assemblage at each point in P and T. V_P and V_S of a bulk mineral assemblage is determined by Voigt-Reuss-Hill averaging of the velocities of each constituent phase (Figure 2.2a and 2.2b). The effects of anelasticity on shear wave velocity are incorporated using a model for the S-wave quality factor Q_S that varies with temperature T and depth z as $Q_S(z, T) = Q_o \omega^a \exp\left(\frac{a\xi T_m}{T}\right)$, where ω is frequency, a is exponential frequency dependence, ξ is a depth scaling factor, and T_m is the dry solidus melting temperature. Our anelasticity model, Q7g uses values of Q_o = 0.1, 0.5, 1.5 for the upper mantle, transition zone, and lower mantle respectively. ξ in these intervals is 38, 30, and 26. The frequency ω is assumed to be 1/20 Hz, and a is assumed to be 0.15. We use the dry solidus calculated in *Herzberg et al.* (2000) for the upper mantle and *Zerr and Diegeler* (1998) for the lower mantle. The calculation of V_P and V_S is not well defined where partial melt is present, which may occur in the shallow plume head. We estimate reductions in seismic velocity at temperatures above the dry solidus by linear extrapolation using the local temperature derivatives at the solidus.

A maximum plume temperature anomaly of 750 K in the lower mantle corresponds to shear-velocity reductions of up to 4%. Although plume excess temperature is smaller in the upper mantle, the shear-velocity reduction is, on average, about 10% along the plume axis. Maximum shear-velocity reductions of 15% near 410 and 660 km depth are due to perturbations of the phase-transition depth.

2.2.3 3D waveform computations

We compute the full 3D wavefield using the spectral element solver SES3D (*Gokhberg and Fichtner*, 2016), which solves the integral form of the elastic wave equation in a heterogeneous media. We simulate signals with periods between 10–200 s using a bandpass filtered Heaviside source time function. The simulation of T $>$ 10 s waveforms for 30-minute long seismograms is computed in approximately 30 minutes real time on 864 parallel compute nodes, each equipped with a GPU accelerator.

The computational domain is a spherical shell that spans 120 degrees in longitude, 70 degrees in latitude, and 2500 km in depth. The domain consists of 4.68×10^7 elements and 5.85×10^9 grid points to ensure that at least two elements sample the shortest wavelengths ($\approx$ 40 km).

We place the earthquake source at 400 km depth in order to avoid interference of direct waves and depth phases. The plume axis is 45° from the source (Figure 2.3) so direct S and P waves simulated for teleseismic distances (30–80°) do not interact with the core. We calculate seismograms for the reference background model and each plume model at a grid of stations behind the plume axis (Figure 2.3b). This geometry represents a hypothetical seismic experiment in the NE Pacific designed to image the mantle structure beneath Hawaii using recordings of earthquakes in the Tonga-Fiji region.

Synthetic seismograms for plume model R1b (Figure 2.4) show delays and waveform complexity as a function of distance, which are typical for all plume models. Waveform complexity near $X = 4°$ is due to multi-pathing as S interacts with the strong wavespeed gradients at the margins of the plume head. For $X > 8°$, when S crosses the plume axis in the lower mantle, waveforms for plume R1b and the background model are nearly identical except for a time offset (i.e., the traveltime delay). For increasing X, the traveltime delay diminishes from about 3 s at $X = 10°$ to about 0.5 s at $X = 40°$. Wave diffraction around the plume conduits is not clearly visible in the S coda at 10 s period.

2.3 Dynamical plume models

We simulate four seismic structures for three plumes with different morphologies by modifying the thermal Rayleigh number Ra, η, ΔT_{CMB}, and by incorporating phase changes (Figure 2.5 and Table 2.1). We choose a limited set of plumes because of the computationally expensive waveform simulations. However, they represent the range of widths and strengths of plume conduits in the lower mantle and the range of expected P-wave and S-wave delays.

Plume models R1a and R1b represent two stages of evolution of the same plume. This plume ascends in a mantle with moderately temperature-dependent rheology (b = $\ln(10^2)$), a thermal Rayleigh number of 2×10^6, and with phase transitions. $\Delta T_{\rm CMB}$ = 750 K, which renders an excess temperature in the upper mantle of ∼450 K. The viscosity in the upper mantle is $30\times$ smaller than the viscosity in the lower mantle, i.e., $\eta_2 = \eta_3/30$. At 45 Myr (model R1a), the broad plume head is still in the lower mantle. At 55 Myr (model R1b), the plume head has crossed the upper mantle transition zone and begins to spread beneath the lithosphere, and its conduit has narrowed due to the reduction in viscosity. Reductions of V_S are as large as 15% in the plume head. The tail has a diameter of 200 km and V_S has been reduced by up to 4%. We define plume tail width to be the point at which plume excess temperature diminishes to half of the maximum value at a given depth, as in *Goes et al.* (2004).

Plume R2 ascends in a mantle with weakly temperature-dependent viscosity (b = $\ln(10)$), a thermal Rayleigh number Ra = 10^6 and $\Delta T_{\rm CMB} = 750$ K. We omit the effect of phase changes and the viscosity $\eta_2 = \eta_3 = 10^{22}$ Pa s in both the upper and lower mantle, which leads to a more simple lower mantle structure in contrast to R1b. Plume R2 is sluggish because of the weak temperature-dependence of viscosity and the low Ra. Its rise time is ≈ 200 Myr as opposed to ≈ 50 Myr for R1b. The plume tail has a diameter of about 400 km in the lower mantle. Without the viscosity reduction in the upper mantle, the plume conduit remains broad after crossing the 660-km phase transition. Although the viscosity structure and Rayleigh number differ significantly, the temperature and V_S along the plume axis in models R1b and R2 are similar because the excess temperature in the upper mantle is primarily controlled by the dissipation number Di and $\Delta T_{\rm CMB}$ (*Albers and Christensen*, 1996).

The plume in model R3 has developed in a relatively weak thermal boundary layer ($\Delta T_{\rm CMB}$ = 550 K), and it has a relatively small excess temperature (≈ 350 K) at the base of the lithosphere. The mantle has a rheology with strong temperature dependence (b = $\ln(10^3)$). As in R1a and R1b, we incorporate a viscosity reduction by a factor of 30 in the upper mantle and the effects of phase changes in the transition zone. The thermal Rayleigh number Ra = 8×10^5. The plume tail is narrow (150 km in diameter) and V_S reductions are smaller than in R1a, R1b, and R2. The thin and weak tail of R3 may be the most challenging to image seismically. As plumes R1b and R3 evolve further in time the tails broaden slightly, as they no longer feel the pull of the buoyant plume head.

Figure 2.6 shows the depth-dependence of buoyancy flux B for each plume model. The variations of B with depth primarily reflects the position of the buoyant plume head. Buoyancy flux also increases from the lower mantle to the upper mantle if the viscosity in

the upper mantle is lower. The plume in model R1b has the largest upper mantle buoyancy flux of $B = 20 \times 10^3$ kg/s, which is more than twice as large as B estimated for Hawaii. R1b is not in steady state as the plume head is still rising in the upper mantle. We expect a transient reduction of B for a long-lived plume supported swell (such as Hawaii) after the plume head spreads and cools beneath the lithosphere. The values of B in Table 2.1 apply to the plume tail at 2500 km depth. These estimates may be most comparable to estimates of buoyancy flux beneath hotspots (*Goes et al.*, 2004).

2.4 Seismic wave propagation through plume models

We analyze the waveform differences between the background model and the four seismic models using two approaches. In the first approach, we measure S and P wave delay time by cross-correlation. In the second approach, we measure instantaneous phase differences (*Bozdağ et al.*, 2011), which allow for small amplitude diffracted arrivals to be analyzed.

2.4.1 Traveltime delays from waveform correlation

The P and S delay times (ΔT_{P} and ΔT_{S}) (Figure 2.7) are defined by waveform cross-correlation functions. We determine the delay using the first upswing and maximum, which correspond to about an 8 s long wave segment. Given the slight differences between the waveforms for the background and plume models, we modify the cross-correlation window to determine how the delay times vary as a function of window length. From the variability we estimate that our measurements of delay times have uncertainties of about $\pm$ 0.1 s at a period of 10 s. The uncertainties are slightly higher at longer periods.

For plumes R1b, R2, and R3, which have plume heads in the upper mantle, the form of ΔT_{P} and ΔT_{S} up to $X = 10^\circ$ is determined by the shape and width of the plume head in the upper mantle. The peak delay is recorded near the plume axis at about $X = 4^\circ$ when P and S propagate steeply through the center of the plume head. Model R2 produces the largest ($\Delta T_{\mathrm{S}} = 15$ s and $\Delta T_{\mathrm{P}} = 4$ s) and broadest imprints of ΔT_{P} and ΔT_{S} because it has the strongest and widest plume head beneath the lithosphere. At $X > 10^\circ$, ΔT_{P} and ΔT_{S} decrease smoothly as P and S traverse the plume tail at progressively larger depth. For plume model R3, the weakest and thinnest plume, S and P delays are approximately 0.4 s and 0.1 s, respectively. The P and S delays due to plume R1a begin at about $X = 10^\circ$ behind the plume axis when P and S turn in the lower mantle. For all models, the P delay is recorded slightly earlier than the S delay because, at the same period, Ps has a broader Fresnel zone than S.

Figure 2.8 shows ΔT_S as a function of X along the axis through the event and plume (i.e. $Y = 0$) for periods of $T > 10$ s, $T > 20$ s, and $T > 40$ s, and computed using ray-theory. The ray-theoretical delay times and the delay times determined from waveform correlation have the same character. The maxima in ΔT_S at $X < 10°$ reflect the complexity of the seismic structure of the plume head. Ray-theory predicts these maxima to be strongly peaked. The maxima in ΔT_S are smallest and smoothest when measured from the longest period waveforms because, at increasingly longer periods, the Fresnel zones widen.

At $X > 10°$, when S samples the plume tail in the lower mantle (for models R1b, R2, and R3), the ray-theoretical ΔT_S and ΔT_S determined by cross-correlation decrease monotonically with X for three reasons. First, for increasing X, S crosses the plume tail along a shorter path. Second, ΔV_S decreases with depth (see Figure 2.2), albeit slightly. Third, wave diffraction (i.e. wavefront healing) causes wave delays to diminish. This effect is strongest at the longest periods. Therefore, ΔT_S is smallest when determined from waves with the longest periods and the widest Fresnel zones.

For model R2, a relatively strong plume, ΔT_S at $X = 35°$ is 1.2 s, 1.0 s, and 0.8 s at periods of 10 s, 20 s, and 40 s, respectively. For model R3, the weakest and narrowest plume, ΔT_S at $X = 35°$ is 0.5 s, 0.4 s, and 0.3 s at periods of 10 s, 20 s, and 40 s, respectively. These delays are about half the delays predicted by ray theory.

2.4.2 Instantaneous phase misfit

The instantaneous phase analysis (*Rickers et al.*, 2012, 2013) is useful to isolate signals of wave diffraction around the plume tail. These diffractions have low amplitudes relative to direct arrivals and would contribute insignificantly to waveform cross-correlation functions. Instantaneous phase differences are independent of signal amplitude and thus not dominated by the high-amplitude direct arrival. Instantaneous phase misfits, $\Delta\phi(t)$ are calculated for S at periods T $>$ 20 s and T $>$ 40 s over an extended time window of 80 s to include signal due to plume diffraction. At this relatively long period and with water-level stabilization, the analysis is not complicated by large phase mismatches. Measurements of instantaneous phase misfit are visually inspected to ensure that $\Delta\phi(t)$ is well behaved.

Figure 2.8 (right column) shows the L2 norm of the instantaneous phase misfit, $||\Delta\phi(t)||$, as a function of X for the seismic models in Figure 2.5. The form of $||\Delta\phi(t)||$ resembles ΔT_S determined by cross correlation. However, $||\Delta\phi(t)||$ decays more slowly with distance because the small-amplitude diffractions contribute to the measurement of the delay. At periods of T $>$ 40 s, cross-correlation measurements of R3 decay to less than 2% of their maximum value at $X = 10°$. Equivalently large instantaneous phase misfits are still

observed up to $X = 40°$. In addition, non-zero instantaneous phase misfit values are recorded over a wider range in azimuth. These results demonstrate that, at low frequencies, the instantaneous phase measurement is more useful than time-domain waveform cross-correlation to resolve the narrow plume conduits in the lower mantle, in agreement with *Rickers et al.* (2012).

2.5 Discussion and Conclusions

Models R1b and R3 (see Figure 2.5) are our end-member estimates of V_P and V_S reductions within the conduits in the lower mantle. The seismic structure of R1b includes up to 2% and 4% reductions in V_P and V_S which delay teleseismic P and S waves by about 0.15 s and 0.7 s. V_P and V_S in the tail of R3 are reduced by as much as 1.8% and 3.5% and lead to P and S delays of about 0.1 s and 0.45 s. The delay times depend on the chosen frequency band in which P and S are analyzed because Fresnel zones broaden with decreasing frequency. S delays for model R1b (at a distance $X = 35°$ in Figure 2.8) are 0.7 s for $T > 10$ s and 0.4 s for $T > 40$ s. S delays for model R3 are 0.5 s for $T > 10$ s and 0.3 s for $T > 40$ s. These delays are up to 50% smaller than ray-theoretically predicted delays. To ensure that the presence of a plume head in the upper mantle is not biasing our results, in addition to the work shown, we separately modeled the upper and lower mantle expression of plume R1b (i.e., both just the head and just the tail). We find that delays induced by the plume head disappear entirely for distances larger than $X = 10°$, and that any delay signal beyond this distance can be attributed entirely to the plume tail.

Given that plumes may have a distinct composition (*Ballmer et al.*, 2013; *Lin and van Keken*, 2005; *Dannberg and Sobolev*, 2015) and that the conversion between temperature, composition, and wave speed structure is uncertain (*Styles et al.*, 2011; *Cobden et al.*, 2008), we estimate that the P and S wave reductions are uncertain by 30%. Waveform simulations indicate that the P and S delays depend linearly on the V_P and V_S reductions in agreement with previous modeling (*Mercerat and Nolet*, 2013). If V_P and V_S are enhanced or reduced by 30%, the delay times increase or decrease by 30% (Figure 2.9).

These delays are somewhat larger than the delays we have previously determined using 2D modeling (*Hwang et al.*, 2011). Nevertheless, we remain skeptical that faint delays in P (< 0.3 s) associated with thin thermal plumes are detectable in currently available seismic data sets. The 0.4–0.8 s delay of S waves by lower mantle plume conduits and the diagnostic frequency dependence should be observable when the influence of the heterogeneous crust and uppermost mantle is small. For example, recordings of abundant earthquakes in the Tonga-Fiji and Kermadec regions by a wide-aperture network of ocean-

bottom seismometers (OBS) in the northeast Pacific (as sketched in Figure 2.3b) would provide wave sampling of the lower mantle beneath Hawaii. Since the structure of the crust and lithosphere beneath the northeast Pacific is relatively simple, traveltime delays accrued in the lithosphere may be estimated using plate cooling models and from delay time measurements over a broad range of source azimuths. The traveltime dispersion due to reverberations in the crust (*Hwang et al.*, 2011) is different than the dispersion due to plumes and can be can be estimated from layered models of the oceanic crust. Ideally, such OBS network cover the ocean floor beyond the Hawaiian swell to ensure lower mantle sampling beneath Hawaii and to record the smooth and systematic decay of the traveltime delays.

2.6 Figures - Chapter 2

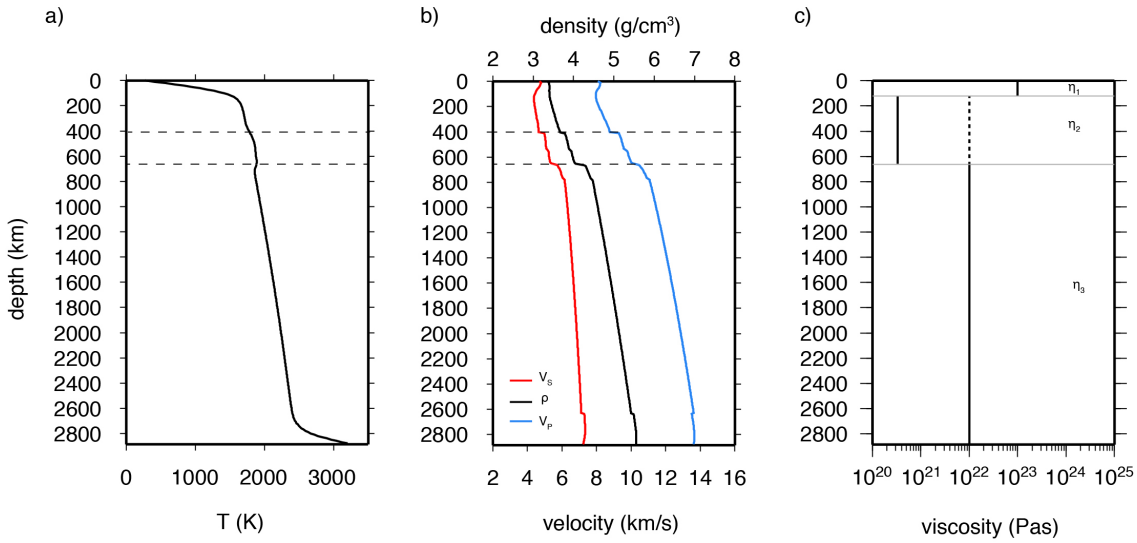

Figure 2.1: References profiles for (a) temperature and (b) V_S (red line), V_P (blue line), and density (black line). Reference values are calculated along the reference geotherm of the dynamic plume models. Note the anomalous changes in temperature, V_S, V_P, and density near the 410-km and 660-km phase transitions (dashed lines) due to latent heat effects. (c) Prefactors of three-layer viscosity profile $\eta(z)$: $\eta_3 = 10^{22}$ Pa s in the lower mantle, $\eta_1 = 100\,\eta_3$ in the lithosphere, $\eta_2 = \eta_3$ or $\eta_2 = \eta_3/30$ in the upper mantle.

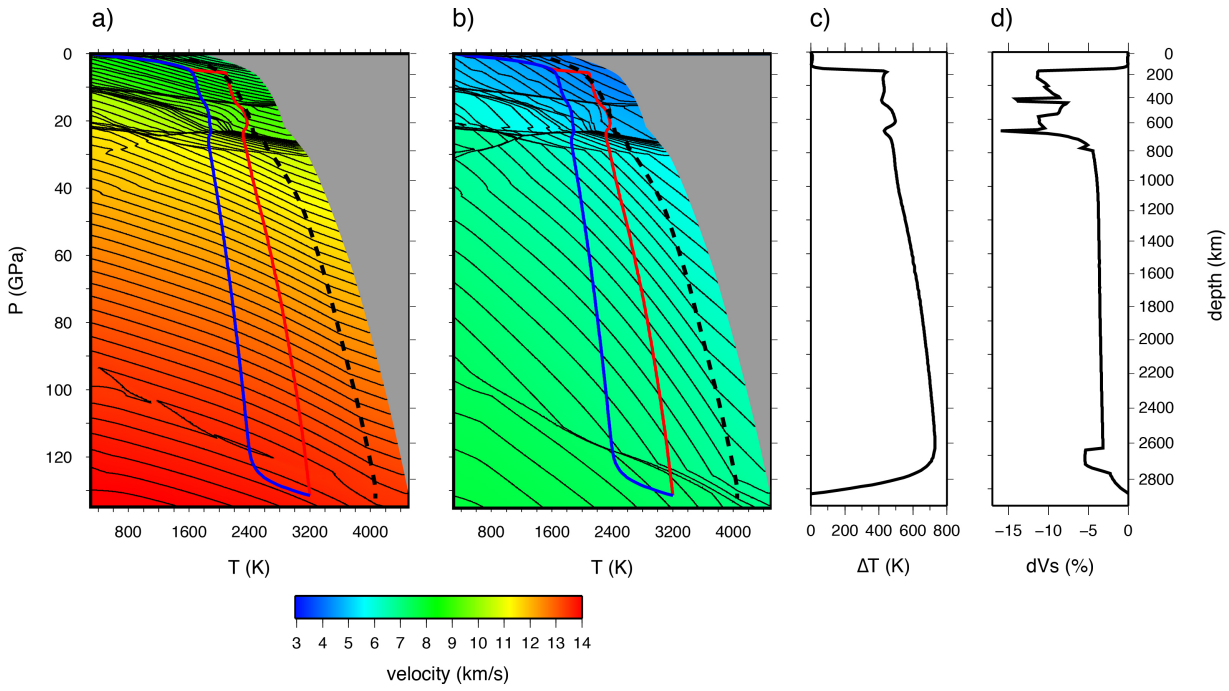

Figure 2.2: (a) V_P and (b) V_S as a function of pressure and temperature. The blue line is the geotherm for the reference structure. The red line is the geotherm along the plume axis of model R1b. The dry solidus of pyrolite is shown as a bold dashed line. Seismic velocity contours are shown every 0.1 km/s. (c) Plume excess temperature, ΔT, and (d) shear-velocity reduction along the axis of plume R1b. Peaks near 410 and 660 km depth are due to phase transitions.

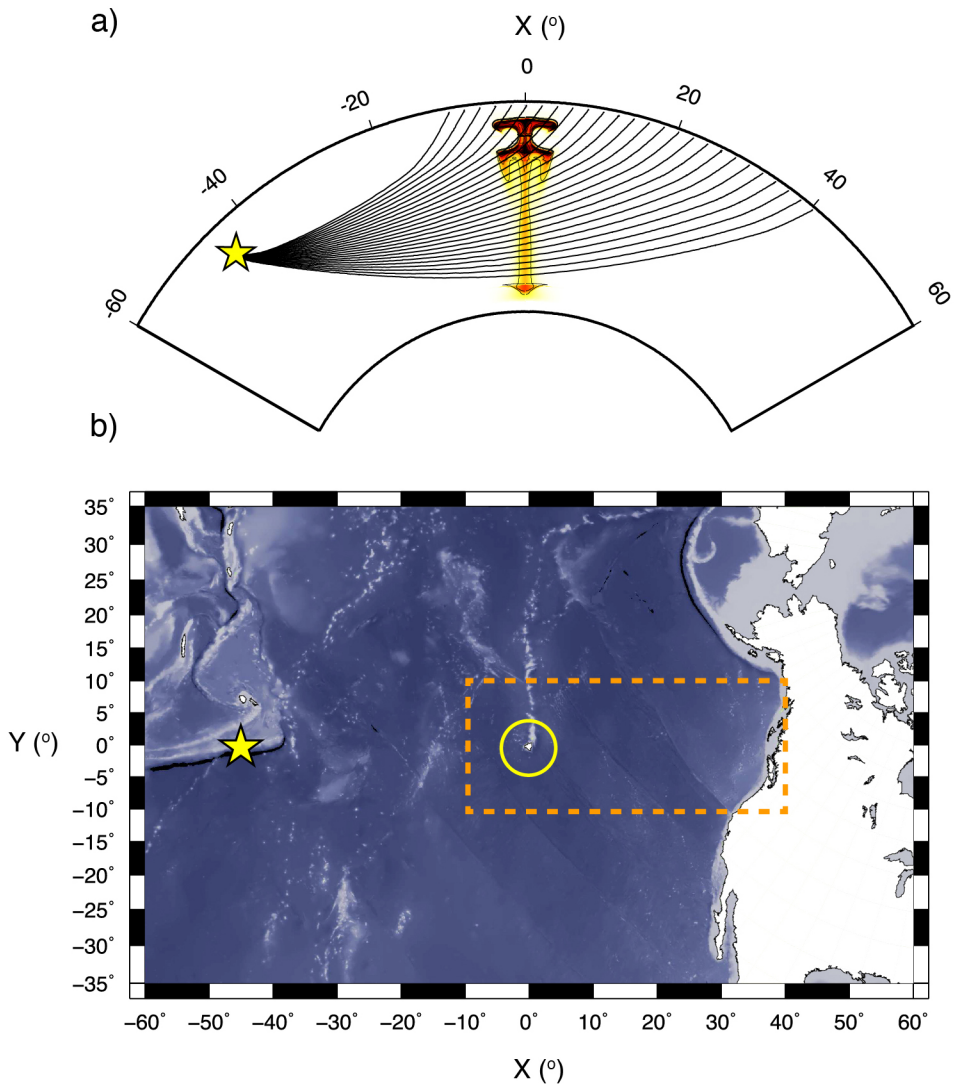

Figure 2.3: (a) Vertical cross section of the geometry of the seismic model. Plume R1b is at X=0, the earthquake at X=-45° and a depth of 400 km. The black line are ray paths to illustrate the P and S propagation through the plume. (b) Map view representing the geometry of the model domain. The domain spans 120 degrees in X and 70 degrees in Y. The earthquake (yellow star), plume (yellow circle), and a grid of seismic stations (dashed line) represents a hypothetical seismic deployment designed to image the mantle beneath Hawaii using recordings of earthquakes in the Fiji-Tonga region at stations in the NE Pacific.

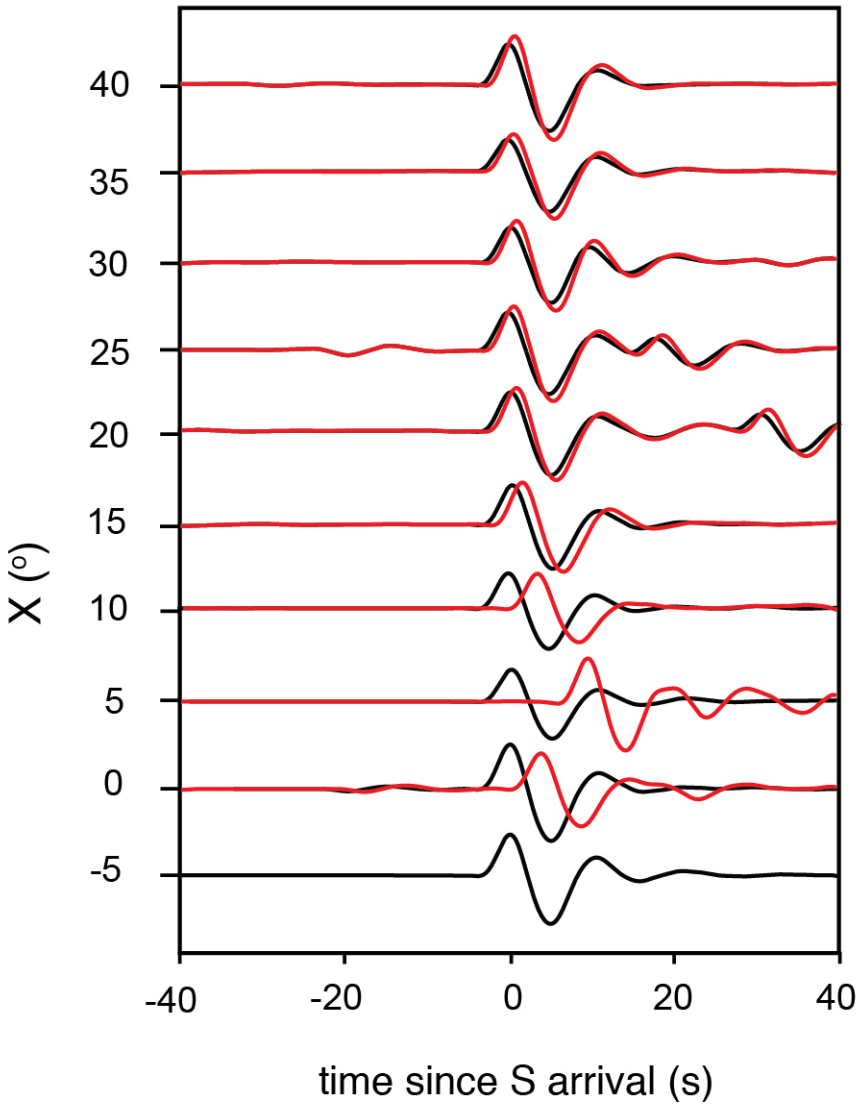

Figure 2.4: S waveforms for the background model (black) and plume model R2 (red) as a function of distance X from the plume axis. The waveforms have a minimum period T = 10 s. They have been aligned on the theoretical arrival time of the S wave for the background model.

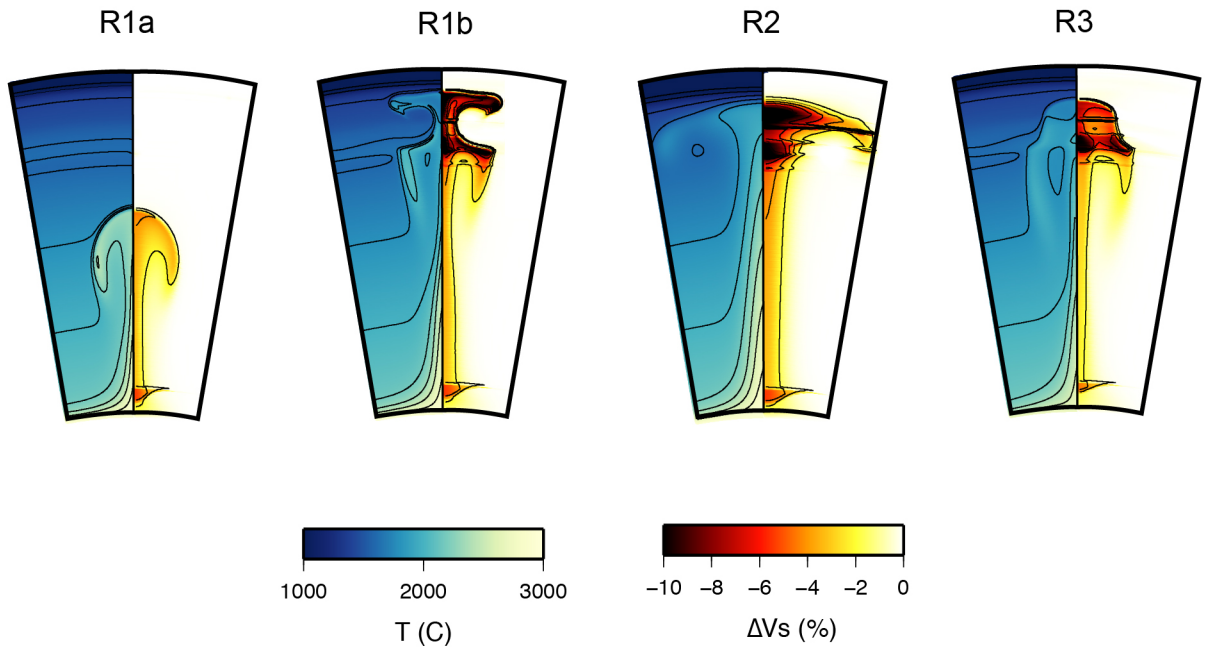

Figure 2.5: The temperature field (left half) and S-wave velocity perturbations ΔV_S (right half) of plume models R1a, R1b, R1c, R2, and R3. ΔV_S is relative to the reference shear velocity profile in shown in Figure 1. Temperature and ΔV_S contours are shown every 200 K and every 2%, respectively. The cross sections are 20° wide and extend from the surface to the core mantle boundary.

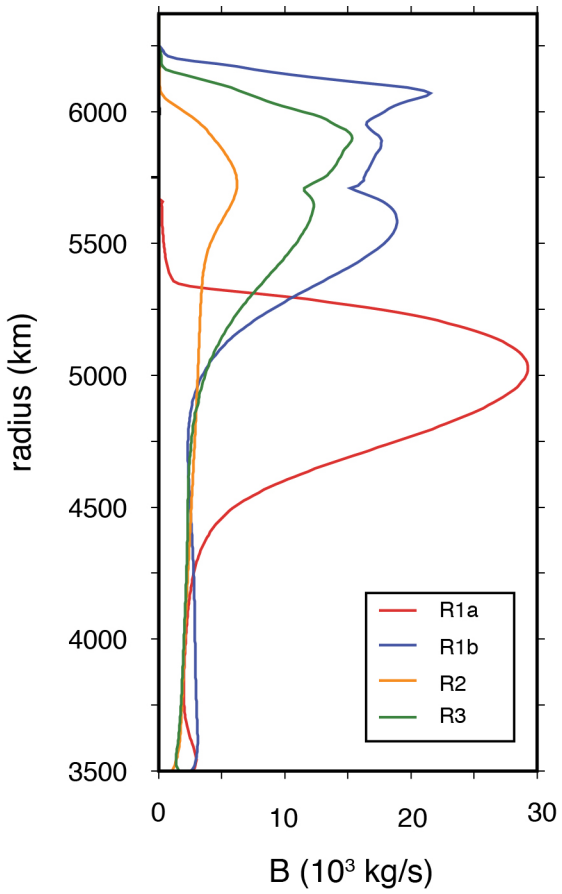

Figure 2.6: Plume buoyancy flux as a function of depth for plumes R1a (red), R1b (blue), R2 (orange), and R3 (green).

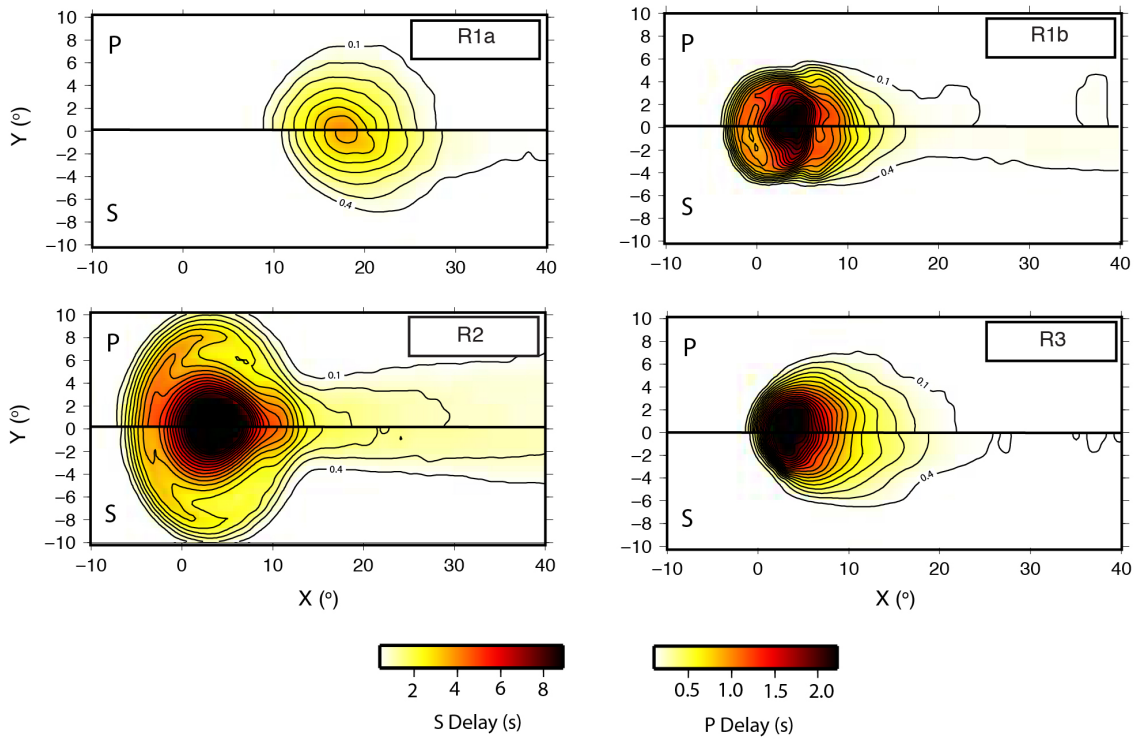

Figure 2.7: Cross-correlation delay times for plume models R1a, R1b, R2, and R3 as a function of X and Y. The top half and bottom half of each map show P and S delays, respectively. The S wave delay time scale is 4 times wider than the P delay time scale. P wave contours are drawn every 0.125 s, starting at 0.1 s. S wave contours are drawn every 0.5 s, starting at 0.4 s.

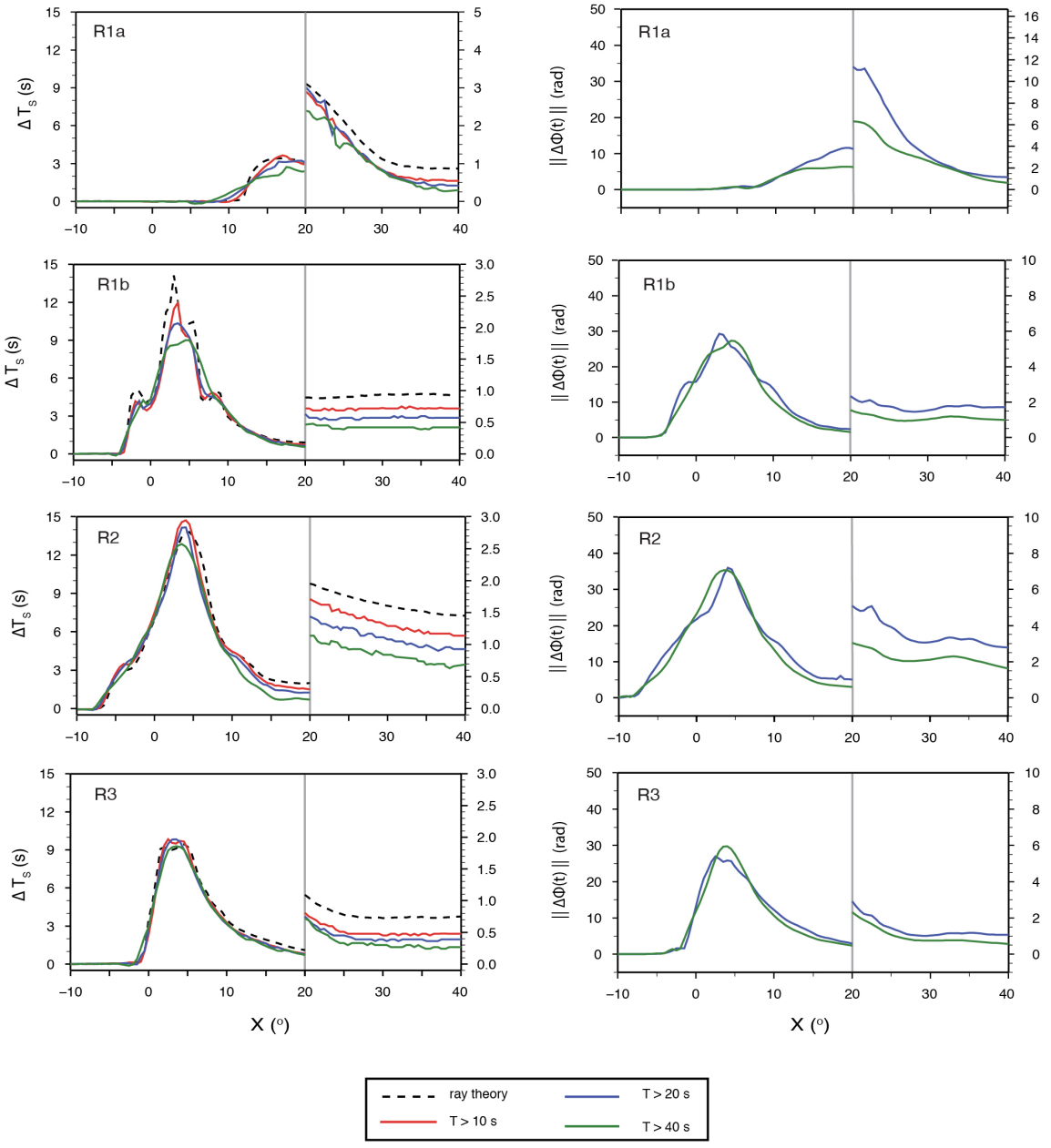

Figure 2.8: (left column), ΔT_S as a function of X along the earthquake-plume axis (i.e., $Y = 0$) for each of the four plume models. The dashed line shows calculated ray theoretical delays. The solid lines show ΔT_S determined by cross-correlation of waveforms with periods larger than (red) 10 s, (blue) 20 s, and (green) 40 s. At distances greater than X = 20, the vertical scale is exaggerated to show detail. (right column) Norm of instantaneous phase misfit measured along the earthquake-plume axis for periods larger than 20 s (blue) and periods larger than 40 s (green).

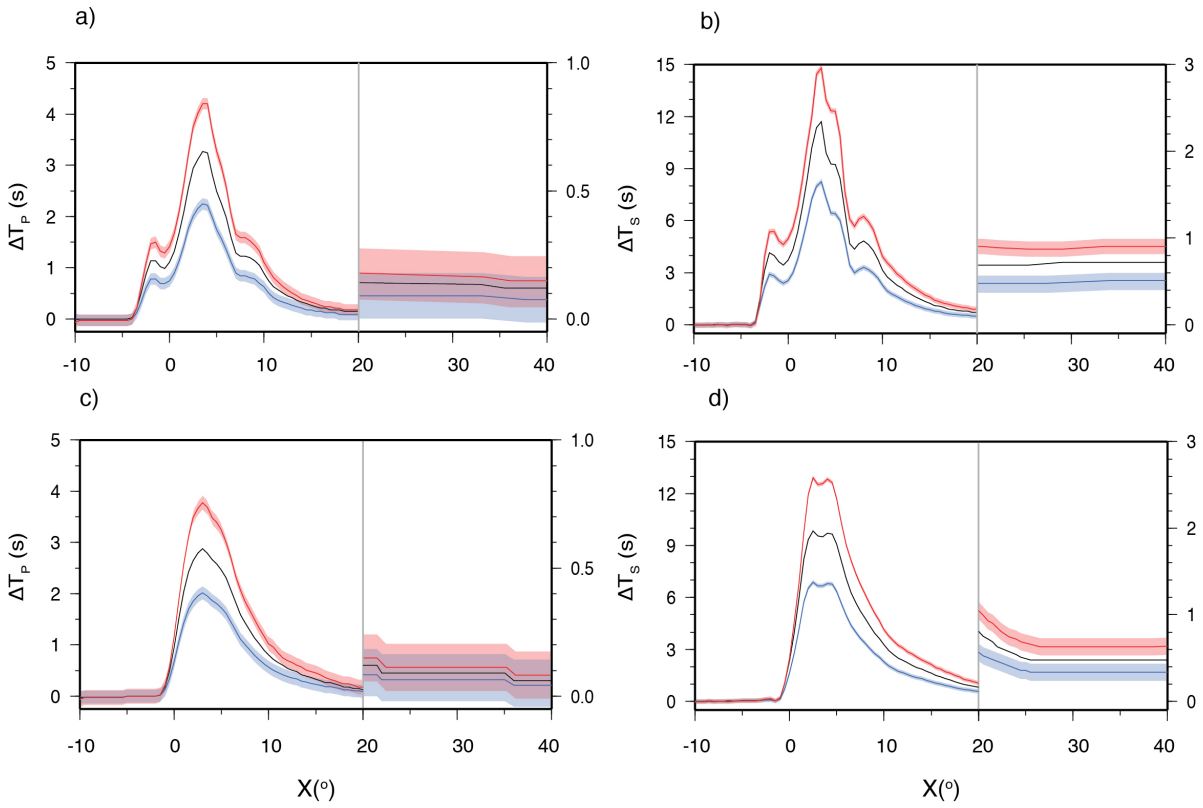

Figure 2.9: P (left) and S (right) delay times as a function of distance X behind the plume for models R1b (a and b) and R3 (c and d), measured at periods larger than 10 s. The shaded regions indicates the measurement uncertainty of $\pm$ 0.1 s. The black line shows delay times for models R1b and R3 (see Figure 5). The blue and red lines show measured delay times after multiplying the P and S velocity reductions by a factor 0.7, and 1.3 respectively. These represent the upper and lower bounds of the uncertainties associated with the temperature conversion.

	Ra	Time (Myr)	Δ T_{CMB} (K)	b	B (Mg/s)	Phase Changes
R1a	2×10^6	45	750	$\ln(10^2)$	2.00	Yes
R1b	2×10^6	55	750	$\ln(10^2)$	2.91	Yes
R1c	2×10^6	175	750	$\ln(10^2)$	1.53	Yes
R2	1×10^6	201	750	$\ln(10)$	1.94	No
R3	8×10^5	106	550	$\ln(10^3)$	1.87	Yes

Table 2.1: Physical parameters used in plume simulations.

CHAPTER 3

Evaluating the resolution of deep mantle plumes in teleseismic traveltime tomography *

Abstract

The strongest evidence to support the classical plume hypothesis comes from seismic imaging of the mantle beneath hotspots. However, imaging results are often ambiguous and it is questionable whether narrow plume tails can be detected by present-day seismological techniques. Here, we carry out synthetic tomography experiments based on spectral element simulations of seismic waves with period T $>$ 10 s propagating through geodynamically derived plume structures. We vary the source receiver geometry in order to explore the conditions under which lower mantle plume tails may be detected seismically. We determine that wide aperture (4,000 – 6,000 km) networks with dense station coverage ($<$ 100 – 200 km station spacing) are necessary to image narrow ($<$ 500 km wide) thermal plume tails. We find that if uncertainties on traveltime measurements exceed delay times imparted by plume tails (typically $<$ 1 s) the plume tails are concealed in seismic images. Vertically propagating SKS waves enhance plume tail recovery but lack vertical resolution in regions that are not independently constrained by direct S paths. We demonstrate how vertical smearing of an upper mantle low-velocity anomaly can appear as a plume originating in the deep mantle. Our results are useful for interpreting previous plume imaging experiments and guide the design of future experiments.

*Chapter 3 is published in *Journal of Geophysical Research: Solid Earth*: Maguire, R., Ritsema, J., Bonnin, M., van Keken, P. E., & Goes, S. (2018). Evaluating the Resolution of Deep Mantle Plumes in Teleseismic Traveltime Tomography. Journal of Geophysical Research: Solid Earth, 123(1), 384-400.

3.1 Introduction

Seismic imaging of the structure of mantle plumes and constraining the role of plumes in the dynamics of Earth's remain important research objectives. Estimates of plume heat flux inferred from hotspot swells indicate that plumes carry 5–10% of the Earth's 44 TW of heat (e.g., *Sleep*, 1990). Plumes may be responsible for the emplacement of large igneous provinces, continental breakup, and mid-plate volcanism (see *Ballmer et al.* (2015) for a review). Over the past two decades seismologists have sought evidence for plumes from estimates of the thermal perturbations of phase boundaries in the transition zone (e.g., *Shen et al.*, 1998; *Li et al.*, 2000; *Schmandt et al.*, 2012) and from tomographic imaging (e.g., *Wolfe et al.*, 1997; *Allen et al.*, 1999; *Montelli et al.*, 2004; *Wolfe et al.*, 2009; *French and Romanowicz*, 2015).

Seismic tomography in particular is a powerful technique to illuminate plumes in the deep mantle and their interactions with large-scale flow and physical boundaries in the mantle transition zone. However, interpreting seismic models remains difficult for several reasons. First, seismic station coverage at hotspots, particularly in oceanic regions, is limited, which inhibits sampling of deep mantle structure with direct P and S waves. Waves that propagate nearly vertically through the mantle, such as SKS, sample the deep structure beneath hotspots but have limited vertical resolution. In regions with low and non-uniform data coverage regularization of the inversion may distort seismic velocity anomalies. The artificial elongation of velocity anomalies along near-vertical teleseismic ray paths complicates estimates of the depth extent of plumes. Second, the delays of seismic waves after propagating through narrow plume conduits in the lower mantle may be immeasurably small (e.g., *Hwang et al.*, 2011; *Rickers et al.*, 2012; *Maguire et al.*, 2016). Finite-frequency theory (e.g., *Nolet and Dahlen*, 2000; *Hung et al.*, 2001) accounts for the effects of wave diffraction (i.e., wavefront healing) on traveltime delays. However, it is unclear if in practical terms finite-frequency tomography offers higher image resolution compared with ray theoretical tomography when measurement errors and the contributions of shallow structure to traveltime delays are relatively large (e.g., *Trampert and Spetzler*, 2006).

We evaluate how thermal plumes are imaged in teleseismic traveltime tomography using resolution tests that are commonly applied to assess the potential artifacts in tomographic images (e.g., *Grand*, 1987; *Spakman et al.*, 1989; *Styles et al.*, 2011). Our models of thermal plumes are based on geodynamic predictions of the temperature structure in the mantle beneath plumes and mineral-physics based estimates of seismic velocities. We calculate the travel time signature of a set of dynamic plume structures using 3D waveform simulations following our previous work (*Maguire et al.*, 2016). We invert these

'synthetic' data using both ray theory and finite frequency theory following methods using regional-scale teleseismic traveltime tomography. Our approach is similar to that of *Rickers et al.* (2012) and *Xue et al.* (2015) with the important difference that our plume structures are based on dynamically consistent compressible flow models of mantle plumes that satisfy geodynamic constraints together with a consistent mapping of temperatures to seismic velocity using mineral physics constraints. While plumes in the real Earth may deviate substantially from our idealized models, it is useful to consider geophysically plausible plumes since the range of widths, excess temperatures, and velocity perturbations are consistent with our current understanding of mantle dynamics and mineral physics.

While it is widely accepted that many hotspots exhibit upper mantle seismic anomalies, the debate on the resolvability of lower mantle plume tails continues. Therefore our tests are focused on the imaging of the plume tail in the lower mantle. We do not explore in detail the structure of the plume head in the upper mantle which may be complicated by shearing driven by plate motion and dynamic layering (e.g., *Ballmer et al.*, 2013). It is our goal to explore how accurately narrow plume tails can be imaged with regional seismic networks, given limited data coverage, inversion regularization, and data uncertainty. In synthetic tomography experiments, we vary the source-receiver geometry to determine the effects of array aperture and station density on image resolution. We choose regional-scale deployments since the direct phases S and P are ideal phases to image the deep mantle especially when they are recorded by wide-aperture, dense regional networks. We estimate the additional resolving power of SKS waves and assess the value of finite-frequency theory over ray theory. We use Hawaii as our example target and evaluate how well a plume there can be imaged using past and planned offshore seismic deployments in the Pacific Ocean.

3.2 Methods

3.2.1 Numerical simulations of plumes

3.2.1.1 Geodynamic modeling

The tested plume structures are based on geodynamic simulations of flow in the Earth using the method previously described by *Maguire et al.* (2016) and *Bossmann and van Keken* (2013). We simulate plumes in a compressible mantle by solving the equations governing conservation of mass, momentum, and energy using the finite-element method in an axisymmetric spherical shell. Plumes are initiated by applying a harmonic perturbation to the thermal boundary layer above the CMB.

We focus on three plumes with different diameters and strengths (Figure 3.1). The range

of dynamic parameters is summarized in Table 3.1. The buoyancy flux of the plume tails varies between 1.5 and 3.0 Mg/s, which is consistent with the range of hotspot buoyancy fluxes reported in *Sleep* (1990). The plume structure depends on several factors, including the temperature contrast across the core-mantle boundary ΔT_{CMB}, the depth dependence and temperature sensitivity of viscosity, the thermal expansivity and conductivity, and the Clapeyron slope Γ_{660} of the ringwoodite-bridgmanite transition near a depth of 660 km (abbreviated as the '660' from hereon). We use a temperature- and depth-dependent viscosity $\eta(T, z) = \eta_0(z) \exp(-b(T - T_{ref}))$ which represents a linearization of the Arrhenius viscosity law. We choose b to be in the range of $\ln(10^1)$ to $\ln(10^3)$. The latter value is consistent with olivine under diffusion creep with an activation energy of E = 300 kJ mol^{-1}. The depth-dependent viscosity profile $\eta_0(z)$ is defined by three layers. In the lower mantle $\eta_0(z) = 10^{22}$ Pa s. In the upper mantle we reduce the viscosity by a factor of 30 in a number of models. The uppermost 120 km of the mantle represents a high-viscosity lithosphere with $\eta_0(z) = 10^{24}$ Pa s.

Models R1a, R1b, and R1c represent three stages of development of the same dynamic simulation. After 45 Myr, plume R1a is a starting plume with a head rising in the lower mantle. After 55 Myr, plume R1b has reached the upper mantle and has begun to spread beneath the lithosphere. The plume structure is complex near the 660 because this boundary partially impedes the flow. After 175 Myr, plume R1c has a quasi-steady state structure. Phase boundary effects have dissipated and the plume head has spread completely beneath the lithosphere. Its tail in the lower mantle has a cylindrical structure with a width of about 500 km. R1c is thinner in the asthenosphere by a factor of about two due to the viscosity reduction above 660. Plume R2 has an anomalously wide (about 800 km) tail due to the modest temperature dependence of viscosity compared to the other models. Plume model R3, on the other hand, has an anomalously thin (less than 400 km wide) and weak tail because the temperature contrast across the CMB is relatively small at 550 K and the viscosity is strongly temperature dependent (b = $\ln(10^3)$). The heads of plumes R1c and R2 have spread horizontally a significant distance beneath the lithosphere. We artificially truncate them to be no wider than 5 degrees from the plume axis so they do not overwhelm the traveltime delay signal from the tail in the deep mantle.

We do not model any thermochemical plumes and therefore ignore the complexities that may arise when chemical entrainment of a dense layer is modeled. *Lin and van Keken* (2006) and *Dannberg and Sobolev* (2015) showed that entrainment of dense eclogitic material may reduce plume buoyancy and broaden plumes in the lower mantle. In addition, non-peridotitic components could change the amplitude of the seismic anomaly. While plumes R1, R2, and R3 are purely thermal in origin the travel time delays in the plume tails

are approximately linear with respect to velocity perturbation (e.g., *Mercerat and Nolet*, 2013; *Maguire et al.*, 2016). Therefore our results can provide insight into the resolvability of stronger or weaker thermochemical plume tails with similar widths.

3.2.1.2 Seismic velocity structure of plumes

The calculation of the seismic velocity structure of plumes R1, R2, and R3 in Figure 3.1 follows the same steps as in *Maguire et al.* (2016). We assume a constant pyrolitic composition (*Workman and Hart*, 2005), defined in the NCFMAS system (i.e., in terms of the six oxides Na_2O, CaO, FeO, MgO, Al_2O_3, and SiO_2). Using the code Perple_X (*Connolly*, 2005) and the thermodynamic database of *Stixrude and Lithgow-Bertelloni* (2011), we compute the equilibrium mineral assemblage and the corresponding elastic parameters and density as a function of pressure and temperature. The seismic velocity of the bulk mineral assemblage is the Voigt-Reuss-Hill average of the velocity of each phase. Subsequently, we add the effects of temperature, pressure, and frequency–dependent anelasticity using model Q7g (as in *Maguire et al.* (2016)). The maximum velocity reduction within plume tails is about 4% for shear waves and 2% for compressional waves. *Cobden et al.* (2008) provide further details of the thermodynamic method including sources of uncertainty.

3.2.2 Seismic modeling

3.2.2.1 Computation of travel time delays

The Preliminary Reference Earth Model (PREM) (*Dziewonski and Anderson*, 1981) is our reference seismic structure of the mantle without plumes. We construct seismic structures for plumes R1, R2, and R3 by superposing their velocity perturbations (from Figure 3.1) on PREM. We note that the choice of reference structure is not an important factor in our analysis given that commonly used 1D Earth models deviate only slightly in the lower mantle. We determine the traveltime delays of the phases P, S, and SKS using spectral-element method (SEM) waveform simulations. The seismic wavefield is described within each element as an expansion in fourth-order Lagrange polynomials. The SEM waveforms are accurate to wave periods longer than 10 s, corresponding to wavelengths in the lower mantle of 130 km (for P waves) and 80 km (for S waves). In contrast to our previous work (*Maguire et al.*, 2016) which was based on SES3D (*Gokhberg and Fichtner*, 2016), we use the spectral-element code SPECFEM3D GLOBE (*Komatitsch and Tromp*, 2002) to simulate the waveforms of core phases.

We analyze synthetic waveforms at teleseismic distances. As an example, Figure 3.2a shows the ray paths of S and SKS propagating through plume R1c for two events at dis-

tances $D = 50^\circ$ (for S) and $D = 100^\circ$ (for SKS) from the plume axis. When the plume axis is at a distance D of 50° from the event, the S waves at epicentral distances between 60° and 90° cross the plume tail in the lower mantle. The SKS waves traverse the plume tail more vertically up to an epicentral distance of 110° when the plume–event distance D is 100°.

We calculate traveltime differences for P, S, and SKS between PREM and the 3-D plume structures by comparing waveform segments centered on P, S, and SKS. The windows are approximately 50 s wide. The seismograms are bandpass filtered between 0.1 Hz and 0.04 Hz. We consider cross correlation delay times when applying finite frequency tomography and onset delay times when applying ray theoretical tomography since the wave onset is a high-frequency signal of a waveform. We discard measurements for waveforms affected by the interference between S and SKS near an epicentral distance of 80°.

3.2.2.2 Tomographic inversion

We invert travel time delays to estimate P-wave and S-wave structure using either ray theory (RT) or finite-frequency theory (FF) following the procedures that have been applied to regional network data (e.g., *Bonnin et al.*, 2014). The theories provide fundamentally different relationships between velocity heterogeneity in the mantle and recorded traveltime delays. According to RT, the travel time delay is sensitive to wavespeed variation along the ray path S:

$$\delta T = -\int_S \frac{\delta v}{v^2}\, ds, \tag{3.1}$$

where v is the absolute seismic velocity and δv is the fractional perturbation relative to v. In FF, the travel time delay is influenced by seismic structure within a volume V surrounding the ray path:

$$\delta T = \int_V K(\mathbf{x})\, \delta v\, dV, \tag{3.2}$$

where the sensitivity kernel $K(\mathbf{x})$ is related to the Fresnel zone.

Figures 3.2b, 3.2c, and 3.2d illustrate the cross-sectional form of $K(\mathbf{x})$ for S, P, and SKS measurements, respectively. S and P kernels are shown for events recorded at an epicentral distance of 80° and the SKS kernel is shown for an event recorded at epicentral distance of 100°. The kernels reflect the sensitivity of cross correlation delay time observations to waves filtered between 10 s $<$ T $<$ 25 s period. At the wave turning depth, the kernel is about 1,000 km wide but the width depends on epicentral distance and wave period. We compute the kernels $K(\mathbf{x})$ for PREM using the paraxial ray approximation introduced by *Dahlen et al.* (2000). We ignore the effects of velocity structure on the ray path S and on

the sensitivity kernels $K(\mathbf{x})$ which we expect to be weak for plume tails (e.g., *Mercerat and Nolet*, 2013).

The model $\mathbf{m}$ is based on the cubed-Earth parameterization (e.g., *Charléty et al.*, 2013; *Bonnin et al.*, 2014) and consists of about 3.5×10^6 blocks with horizontal side lengths between 59–83 km and vertical side lengths between 44–90 km which increase with depth. The global parameterization accommodates both mantle and core phases at teleseismic distances. The size of each voxel is small compared to the width of the finite frequency sensitivity kernels. The distinct 3-D shapes of the kernels are preserved when projected onto the parameterization (*Chevrot et al.*, 2012).

Given the large number of model parameters, we regularize the inversion by applying norm damping (i.e, the total size of the model) and smoothness damping (i.e., the second spatial derivative of the model). We minimize the object function $O(\mathbf{m})$

$$O(\mathbf{m}) = (\mathbf{Gm} - \mathbf{d})^2 + \epsilon_n \, \mathbf{m}^2 + \epsilon_s \, (\mathbf{Sm})^2. \tag{3.3}$$

The first term of $O(\mathbf{m})$ represents the data misfit. The second and third terms represent the model size and the model roughness, respectively. The system matrix $\mathbf{G}$ incorporates the forward theory, $\mathbf{d}$ is the vector of travel time delays, ϵ_n and ϵ_s are the norm and smoothness damping parameters, and $\mathbf{S}$ is a smoothness matrix which minimizes the Laplacian of the model.

The data misfit, χ^2, is defined as

$$\chi^2 = \sum_{i}^{N} \frac{(\sum_j G_{ij} m_j - d_i)^2}{{\sigma_i}^2}, \tag{3.4}$$

where N is the number of data and i and j are the indices of traveltime delays and model parameters, respectively. When the model fits the data to within measurement uncertainties, $\chi^2 = N$. We add varying amounts of Gaussian noise to the synthetic delay time data to approximate random measurement error.

We experiment with different values of the measurement uncertainty σ to estimate preferred models $\mathbf{m}$. We choose the minimum value for σ of 0.1 s, which is equivalent to the time step in the waveform simulations. The maximum value of σ is 1.0 s or 10% of the dominant wave period. It represents a realistic error when the match between observed and synthetic waveforms is poor and when the effects on waveforms of the crust, anisotropy, and 3-D heterogeneity in the deep mantle are uncertain.

We determine the optimal model by varying the values of ϵ_s and ϵ_n, while setting their ratio constant ($r = \epsilon_s/\epsilon_n$). Our tests indicate that $r = 5$ provides a suitable balance between

smoothness and norm damping and we use this value for all inversions unless otherwise noted. The effect of the choice of regularization parameters is explored in Section 3.4.7.

Figure 3.3 shows an example of tradeoff curves used to determine the best fit model for both RT and FF. In both RT and FF the optimal model is near the bend of the tradeoff curve, which indicates that error estimates are well constrained. However, for a given variance reduction χ^2/N, FF always leads to a model $\mathbf{m}$ with a larger L2 norm, indicating that FF recovers images of plume structures with higher amplitudes.

3.3 Network configurations

Seismic network configuration and wave sampling are the key factors determining tomographic image resolution. To understand plume resolution given the practical limitations of network design, especially in ocean basins, we conduct tomographic inversions of the synthetic traveltime data for four different network configurations. We determine the resolution of plumes given (i) ideal data coverage and (ii) incomplete data coverage that is representative of past or newly designed experiments near Hawaii and in the Pacific Ocean.

3.3.1 Configuration A: large network aperture, small station spacing, and homogeneous event distribution

An ideal seismic network has a wide aperture with dense station spacing and records earthquakes over a full range of epicentral distances and azimuths. Here, we assume such a network to be a square grid of stations with a width L and station spacing Δx. The events are at distances D between 30° and 120° and at azimuths every 30° (Figure 3.4a).

We vary L and Δx to explore how network aperture and station density affect resolution. For the largest and densest grid, when $L =$ 6,000 km and $\Delta x = 100$ km the data coverage is optimal, because the inversion results do not improve appreciably if the network aperture L is larger or if station spacing Δx is smaller. The largest network considered provides 254,193 paths for P and S.

3.3.2 Configuration B: the PLUME geometry

The PLUME experiment (*Laske et al.*, 2009; *Wolfe et al.*, 2009) was a comprehensive seismic experiment aimed at imaging the mantle beneath the Hawaiian hotspot. The experiment consisted of 67 land and ocean-bottom seismometers on and surrounding Hawaii which were in operation for more than two years. Figure 3.4b shows the station distribution

of the PLUME experiment, following the description of *Wolfe et al.* (2009). The network aperture is over 1,000 km , with stations typically spaced about 100 km apart. In simulating a set of traveltimes, we use earthquake locations from all events greater than M_W 6 that occurred during the two-year deployment of the PLUME network at epicentral distances between $30°$ and $120°$. The events are not exactly the same as those used by *Wolfe et al.* (2009), which were selected on the basis of waveform quality, but the azimuthal and distance distributions are similar. The total number of raypaths for P- and S-waves is 5,276.

3.3.3 Configuration C: wide-aperture linear arrays

The small array aperture of the PLUME experiment limits the imaging of lower mantle beneath Hawaii. Here, we explore how tomographic resolution can be improved if a hypothetical seismic array deployment has a wider aperture and would be operating for a longer time. The deployment consists of three linear arrays which intersect at Hawaii (Figure 3.4c). The station spacing is $\Delta x = 200$ km, and the length of each array is 50 degrees. The total number of seismometers is 87. In our test the angles between each limb of the array is $60°$ and is optimally aligned with regions of relative high seismicity. We consider a five-year deployment and simulate traveltime measurements for all teleseismic earthquakes greater than M_W 6 that have occurred between 2012 and 2017, which provides 50,738 raypaths for P- and S-waves.

3.3.4 Configuration D: the Pacific Array

The fourth network configuration is based on a conceptual Pacific-wide network called "The Pacific Array" as envisioned by *Kawakatsu et al.* (2016). The anticipated configuration of PA is shown in Figure 3.4d. The Pacific Array (PA) constitutes "an array of arrays". Each of the 14 sub-arrays is comprised a spiral of 10 stations with an aperture of about 500 km which enables the measurement of surface-wave dispersion to study the structure of the crust and lithosphere across the Pacific. The network as a whole provides improved body-wave coverage of the deep mantle. We assume in our modeling that the PA would have been active for the same 2012–2017 period as the previous configuration. The array provides 62,715 direct body-wave paths over this time span.

3.4 Results

We first explore the impact of plume tail width on resolution by showing inversion results for each plume structure using the optimal source-receiver configuration. We next illustrate

how data coverage and other aspects of the inversion process affect image resolution.

3.4.1 Plume images for ideal data coverage

Figure 3.5 shows the resolved images of plumes R1 (at stages a, b, and c), R2, and R3 using FF and RT inversions of S-wave delay times. We use network configuration A shown in Figure 3.4a with L = 6,000 km and Δx = 100 km and assume that the uncertainty in the S-wave traveltime delays has a Gaussian distribution with a standard deviation $\sigma = 0.1$ s. This represents an optimal scenario for a tomographic inversion of teleseismic traveltimes at a regional network of stations: the network aperture is wide, the station spacing is small, the earthquake distribution is uniform, and the traveltime measurements are precise.

Despite the optimal setup, the images derived using both RT and FF reveal the significant distortions and amplitude loss. The intricate head and stem features of the plume in the upper mantle (e.g., plumes R1b and R1c) or lower mantle (e.g., R1a), the dynamic effects of the 660 on plume ascent, and the thinning of the conduit in the low-viscosity upper mantle above the 660 are unresolved. The velocity anomaly of the plume in the lower mantle is strongly reduced due to wavefront healing and the applied model damping. For the same variance reduction, FF resolves the plume tail in the lower mantle with a higher amplitude than RT. For example, $\delta V_S = -1\%$ in the resolved plume tail of R1b imaged with FF, while is only about -0.2% with RT δV_S.

The width of the plume tail is a primary factor in determining the fraction of the input anomaly recovered. Plume R3 has the thinnest tail (less than 400 km wide) and is resolved with the greatest amplitude reduction. With FF the tail is imaged with an amplitude $\delta V_S = -0.5\%$, which is only about 25% of the strength of the input structure. With RT, the shear velocity reduction δV_S in the tail is smaller than 0.1%, which we consider to be undetectable. The tails of plumes R1b and R1c are slightly wider (about 500 km wide) and are recovered with greater amplitude. In the lowermost mantle, with FF, the tails of R1b and R1c are imaged with an amplitude of about $\delta V_S = -1\%$, which is about 30% of the amplitude of the input structure. In the mid-mantle, R1c is imaged with greater amplitude than R1b since the tail of R1b thins slightly near 1500 km depth. With RT, the tails of R1b and R1c are close to invisible in the lowermost mantle (δV_S of about -0.2%). The wide plume tail of R2 (diameter of 800 km) is imaged with the highest amplitude. More than 50% of the initial anomaly is recovered to a depth of 1800 km (imaged amplitude $\delta V_S < -2\%$). Near the base of the mantle the tail diminishes in strength to about $\delta V_S = -1\%$. The broad lower mantle plume head of R1a is imaged with little amplitude reduction with both FF and RT (about 75% of strength of the input structure), but the short stem is less

accurately recovered.

3.4.2 Effects of network spacing and aperture

Image resolution depends on wave path coverage. Networks with dense station spacing offer data redundancy and enable resolution of fine-scale structure. Depth resolution is best for the network with the widest aperture as teleseismic wave crisscross the mantle at large range of angles.

To illustrate how image resolution depends on network aperture and station density, we show in Figure 3.6 the resolved fractional amplitude F with respect to the shear velocity anomaly in the input model: $F = \delta V_S^{\mathrm{OUT}}/\delta V_S^{\mathrm{IN}}$. For plume R1b and using FF, we determine F at three depths along the plume axis in the lower mantle. We use network configuration A for values of L of 2,000 km, 4,000 km, and 6,000 km and Δx of 100 km, 200 km, and 500 km. The standard deviation of delay time measurement error is $\Delta\sigma = 0.1$ s.

Resolution decreases with increasing depth z because data coverage diminishes. For the smallest width (L = 2,000 km), teleseismic S-waves do not cross the plume axis at depths larger than 2,000 km so $F = 0$ regardless of the station spacing Δx. When L = 4,000 km, the plume tail is resolved to over 2,000 km depth. There is a weak signal of plume tail at 2,400 km depth only when the network width is L = 6,000 km. However, the narrow plume tail is resolved with a significant amplitude reduction. At 1600 km depth, F in the plume tail is lower than 30% for the widest width L of 6,000 km and the smallest station spacing Δx of 100 km considered. F decreases with increasing station spacing because the data misfit makes a smaller contribution to the object function O (equation 3).

3.4.3 P-velocity versus S-velocity inversion

Figure 3.7 shows a comparison between S-wave and P-wave inversions for plume R1c using FF theory. We use configuration A and L = 6,000 km, and $\Delta x = 100$ km and assume that the standard deviation of random traveltime error $\sigma = 0.1$ s. Throughout the lower mantle, S wave inversions recover a larger fraction of the input anomaly than P wave inversions. The velocity anomaly in the lower mantle is about -1.0% for S (30% of the amplitude in the input structure) and -0.3% for P (15% of the amplitude in the input structure).

There are two reasons for the higher amplitudes of S velocity anomalies. First, δV_S is stronger than δV_P in the input structures by about a factor of two due to the greater sensitivity of V_S to temperature. Second, the P-wave has a larger wavelength, a wider Fresnel zone, and is more susceptible to the effects of wavefront healing. Given its wider

Fresnel zone, a P-wave is sensitive to structure in the mantle over a broader volume than S-waves and P velocity heterogeneity is imaged with a lower amplitudes. We note that we are comparing inversions of P and S-wave delays calculated in the same frequency band. In practice, P waves may be analyzed at higher frequencies than S waves. If P delays are determined at a period of $T = 5$ s, we expect to recover the same fraction of the plume tail because the sensitivity kernels of P and S would be of comparable size.

3.4.4 The effect of measurement uncertainty

To test the effect of uncorrelated error in travel time measurements, we invert S-wave delay times with variable amounts of assumed noise. We use configuration A with L = 6,000 km and $\Delta x = 200$ km and choose three values for the standard deviation of traveltime error: $\sigma = 0.1$ s, $\sigma = 0.5$ s, and $\sigma = 1.0$ s. We test the effects for plume R1b using FF.

With increasing values of σ, model damping and regularization have higher influence (see equation (3)). This is evident from the comparison of the resolved structure of plume R1b for the three values of σ in Figure 3.8. When the traveltime error is smallest (i.e., $\sigma = 0.1$ s), the deep plume tail is resolved with an amplitude of $\delta V_S \approx$ -1.0%. For $\sigma = 0.5$ s, the recovered shear velocity anomaly in the plume tail is δV_S is weaker than -0.2% and the resolved δV_S is smaller than -0.1% for $\sigma = 1.0$ s. These weak anomalies are likely undetectable.

3.4.5 Comparison between networks

Figure 3.9 compares the resolved images of plume R1c for the four network configurations discussed in section 4. We assume $\sigma = 0.1$ s and invert the delay times using FF. We invert either the delay time of S (Figure 3.9; first column) and S with SKS (Figure 3.9; second column).

High data coverage is key for the imaging of the plume tail in the lower mantle. The images obtained using the optimal experiment geometry are shown in the first row of Figure 3.9 (see also Figure 3.4). They exhibit signatures of the tail of plume R1c deep into the lower mantle. The shear velocity anomaly δV_S in the plume tail is lower for configuration B (representative of the PLUME network around Hawaii) because the aperture is much smaller and the event distribution is inhomogeneous. When distributing a similar number of stations as in B into wide-aperture linear arrays (configuration C), the imaging of the deep mantle structure is significantly better. The Pacific Array distribution of stations across the Pacific Ocean (configuration D) produces a weak signature of the tail in the lower mantle. However, without dense station coverage the images are missing a clear mantle-

wide expression of plume R1c into the upper mantle. We note that resolution in the mid and shallow mantle can be improved by incorporating surface reflections (e.g., SS) and surface wave constraints.

Figure 3.9 demonstrates also that SKS traveltimes provide resolution of the structure in the lower mantle. For example, for configuration A the shear velocity anomaly δV_S in the plume tail diminishes from about -2.0% at 1,000 km depth to less than -1.0% near the base of the mantle when only S traveltime delays are inverted. A joint inversion of S and SKS traveltime delays produces a nearly constant δV_S of -2.0% in the plume tail throughout the lower mantle.

3.4.6 The resolving power of SKS

Wolfe et al. (2009) concluded that SKS is capable of driving resolution of the deep mantle where direct S-waves are absent. Our results confirm this, as is evident in the second row of Figure 3.9, which shows R1c imaged with the PLUME network (i.e., configuration B). When inversions are performed using only S (first panel), the plume is not imaged below a depth of 1,000 km. When SKS is included (middle panel), the plume tail is apparent to a depth of 1,800 km.

However, since SKS propagates nearly vertically through the mantle, it is difficult to resolve structure in the upper mantle and lower mantle independently. To illustrate this, plume head in the upper mantle, we compute and invert S and SKS travel time delays for the same plume R1c in which we have set $\delta V_S = 0$ in the lower mantle (Figure 3.10a). The NW–SE and SW–NE oriented cross sections in Figure 3.10b and 3.10c indicate that upper mantle structure is projected into the lower mantle along dominant S and SKS paths. For instance, the steeply dipping anomaly in Figure 3.10c, labeled X, projects towards a cluster of events in South America at large epicentral distances that produces most of the SKS traveltime delays. In Figure 3.10d the more shallowly dipping anomaly Y has a direction towards the SW, parallel to S-wave paths between Hawaii and Tonga. Similar artifacts towards the NE are missing because only one event in North America contributes to the collection of traveltime delays.

3.4.7 Fast anomalies due to regularization

When data coverage is sparse, regularization artifacts tend to dominate tomographic images. In particular, when strong preference is given to smooth models, artificial high-to-low seismic velocity oscillations may be introduced. Figure 3.11 shows inversion results for R1b imaged with configuration B, in which a high velocity ring shaped anomaly is in-

troduced surrounding the plume head in the upper mantle. The amplitude of the feature is as large as $\delta V_S = +1.0\%$, and could be misinterpreted as dynamic in origin. The artifact is several hundred km wide in some cases, which is much wider than the blocks used in the model parameterization. A notable gap in the ring anomaly is present NE of Hawaii due to a lack of raypath coverage from North American events. The strength and extent of the artifact depends on the choice of regularization. Figure 3.11a shows an inversion with $\epsilon_s/\epsilon_n = 50$ (strong preference for smooth models), and 3.11b shows an inversion with $\epsilon_s/\epsilon_n = 0.02$ (strong preference for small models). In both cases, the fast ring anomaly is present, however it is more prominent when preference is given to smoothness.

The tradeoff for minimizing the high velocity artifact (i.e., giving stronger preference to norm damping), is that a smaller fraction of the true strength of the plume is recovered.

3.5 Discussion

The Hawaii PLUME network has been one of the most comprehensive experiments for studying the structure the mantle beneath a hotspot. It comprised an array of both on-shore and off-shore seismic instrumentation designed to maximize imaging resolution given the constraints on budget and operational logistics. We have also focused on the PLUME experiment in our analysis to illustrate how the imaging of a plume tail in the deep mantle beneath a regional seismic network is complicated by the limited array aperture and inhomogeneous data coverage.

Our analysis confirms that the PLUME experiment is capable of imaging deep mantle structure if traveltime measurements of SKS are incorporated in the analysis. However, the limited vertical resolution complicates the interpretation of teleseismic traveltime tomography images. Seismic structure in lower mantle cannot be resolved independently from structure in the upper mantle from regional network data. Our simple test (shown in Figure 3.10) illustrates how seismic structure in the upper mantle can be projected into the lower mantle along dominant S and SKS paths particularly towards regions with high seismicity. Steeply elongated anomalies in the lower mantle follow SKS paths to distant earthquakes in South America while more shallowly dipping anomalies extend to nearer earthquakes in the western Pacific. These anomalies are reminiscent of the anomalies resolved by *Wolfe et al.* (2009).

However, we do not dismiss the results from *Wolfe et al.* (2009). In our experiment using the head structure of plume R1c, the velocity reduction in upper mantle is as high as $\delta V_S = -10\%$, corresponding to a temperature anomaly of ΔT = 400 K, which is likely to be unrealistically high. We predict that the velocity anomalies that are projected from an

upper mantle plume expression have rather low amplitude ($\delta V_S = -0.3\%$) which is lower than that recovered in the original PLUME experiment (δV_S of about -0.5% extending into the mid-mantle). While the pattern of smearing is similar between the original experiment and our synthetic analysis, the higher amplitude found in the PLUME experiment may well indicate that a true lower mantle plume expression was recovered.

Over the course of its deployment the EarthScope USArray covered the entire contiguous United States (about 4,000 km wide) with stations typically spaced less than 100 km apart. Recent tomographic images using data from USArray (e.g., *Schmandt et al.*, 2012; *Porritt et al.*, 2014; *Burdick et al.*, 2017) have been used to test the hypothesis that the Yellowstone hotspot has a deep mantle plume origin. *Schmandt and Lin* (2014a) image a mostly vertical slow velocity anomaly beneath Yellowstone to a depth of about 900 km. *Porritt et al.* (2014) image a slow wavespeed anomaly to at least the base of the transition zone and potentially deeper, although below the transition zone the anomaly is weakened and tilted. Our results shown in Figure 3.6 suggest a network comparable to USArray is capable of imaging a plume tail to at least 2000 km depth.

The uncertain detection of a plume tail extending into the deep mantle beneath Yellowstone could be due to several reasons. First, a plume tail may be absent if Yellowstone volcanism is fed by a shallow source, or if the deep plume source is waning. Second, the plume may be thinner or weaker than those we consider and thus impart smaller travel time delays. Uncertainties of travel time observations due to the influence of heterogeneous crust may also make imaging the deep plume tail challenging. Additionally, plume dynamics may be complicated by interaction with the sinking Farallon slab (e.g., *Leonard and Liu*, 2016).

The imaging of small scale structure in the deep mantle can potentially be improved either by using multiple-frequency tomography (e.g., *Sigloch et al.*, 2008), which exploits the frequency dependence of body wave dispersion, or full-waveform inversion (FWI) which uses large portions of the seismic signal at broadband frequencies (e.g., *Rickers et al.*, 2013; *French and Romanowicz*, 2015; *Bozdağ et al.*, 2016). A major challenge of FWI is in distinguishing low-amplitude diffracted arrivals in the coda of main arrivals from crustal scattering. FWI may be particularly useful in regions such as the Pacific Plate surrounding Hawaii where the crust is relatively simple. While FWI may be an improvement over traveltime tomography, we argue that the lack of data coverage is still the limiting factor in the imaging of plume tails in the deep mantle. Our analysis here shows that large-scale OBS deployments, while costly, can improve seismic models of the deep mantle and advance the plume debate forward significantly.

3.6 Conclusions

Traveltime tomography is the most powerful tool to image the structure of the deep mantle but the resolution of small-scale structures such as plume tails is inherently limited. To quantify resolution of thermal plume ascent from the core-mantle boundary, we have investigated how deep-mantle plumes are imaged by teleseismic traveltime tomography using regional networks of seismometers and analytical procedures similar to those commonly applied to real data.

We have explored best-case scenarios for network design and data coverage and deployments based on past and proposed experiments. Our computations of plume formation at the core-mantle boundary and plume ascent through the mantle incorporate realistic constraints on thermodynamic and rheological conditions of the mantle and plume buoyancy flux. We use mineral physics constraints to relate the elevated temperature to wave speed reductions in the plume. We predict the traveltime delays from 3-D spectral element method waveform simulations at periods longer than 10 s and invert them using both ray-theory and finite-frequency theory.

Plume tails are imaged with considerably reduced strengths even under under ideal imaging conditions. For wide-aperture, dense networks of stations which have recorded earthquakes at a uniform range of azimuths and epicentral distances, a plume tail in the lower mantle is imaged with an amplitude loss of at least 40%. The strength of the imaged plume tail depends on many factors. We have explored the effects of network aperture, station spacing, data types, delay-time measurement uncertainty, regularization, and applied modeling theory.

While it is difficult to directly compare 'best fit' models for different experiments, the following observations are robust:

(i) For the same frequency band S velocity tomography provides higher image resolution than P velocity tomography since the S-wave delays are stronger and S-wave sensitivity zones are smaller.

(ii) As it accounts for the finite sensitivity zones of waves, finite-frequency inversions provide a clearer and higher-amplitude image of the plume tail than ray-theoretical inversions.

(iii) Measurements of traveltime delays of SKS contribute to the imaging of plume tails. This supports the argument by *Wolfe et al.* (2009) that SKS extends tomographic resolving power to deeper depths.

(iv) The uncertainty in the measured traveltime delay poses a significant limitation on resolution. When the measurement uncertainty is larger than about 1.0 s, it is equal to or it exceeds the expected delay time imparted by plume tail in the deep mantle on the S-wave (see Figure 8 in *Maguire et al.* (2016)). In this case, plume tails cannot be resolved. Hence, accurate estimates earthquake hypocenter locations and event origin times and understanding the effects of the crust and shallow mantle on traveltimes are critical to resolving plumes.

(v) Wide aperture (4,000 – 6,000 km) networks with dense station coverage ($<$ 100 – 200 km station spacing) are necessary to image narrow ($<$ 500 km wide) thermal plume tails. Large scale deployments of OBS networks could significantly advance plume imaging.

Imaging artifacts appear when data coverage is heterogeneous and the effects of model regularization are relatively large. Due to the predominantly near-vertical wave propagation of teleseismic body waves below a regional network, seismic velocity anomalies are artificially elongated in the vertical direction. The artificial elongation bears a strong resemblance to the resolved anomalies in the lower mantle in the shear velocity model of *Wolfe et al.* (2009). Ring-shaped high-velocities anomalies surrounding the low-velocity plume anomaly are primarily an effect of regularization. Such artifacts can be minimized by carefully balancing smoothness and norm damping parameters.

Further modeling work should focus on constraining the effects of compositional variability in plumes on their dynamics and seismic velocity expression, as well as assessing travel time delays caused by thermochemical plumes. Additionally, the seismic expression of plumes in whole mantle convection models should be examined.

3.7 Figures - Chapter 3

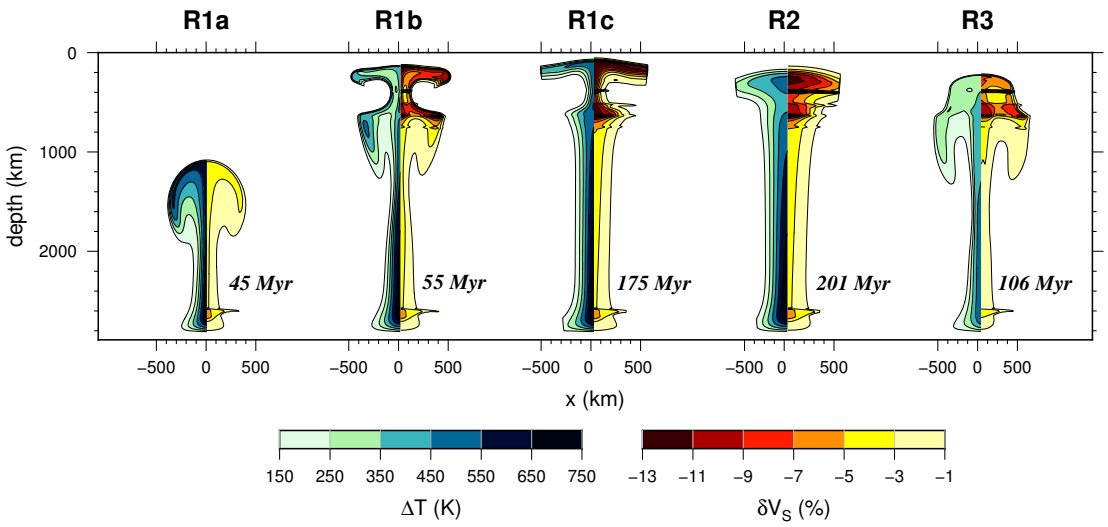

Figure 3.1: Dynamic simulations of plumes used in sensitivity tests. The plumes are symmetric about the vertical axis at $x = 0$. For each plume, the excess temperature is shown on the left and the reduction in shear velocity δV_S relative to PREM is shown on the right. The plume structures R1a, R1b, and R1c are snapshots of the same dynamic simulation at 45 Myr, 55 Myr, and 175 Myr, respectively.

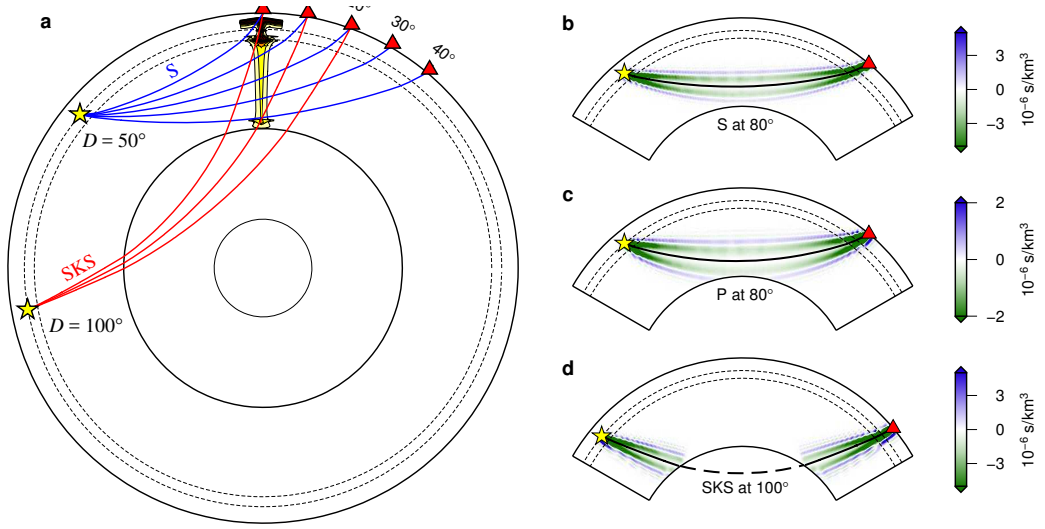

Figure 3.2: (a) Ray geometry for S (in blue) and SKS (in red) waves traversing plume R1c. The distance D between the earthquake and plume is $50°$ for S and $100°$ for SKS. X is the angular distance beyond the plume along the great circle path. (b – d) Sensitivity kernels $K(\mathbf{x})$ for cross correlation travel time delays measured over the frequency band 0.04 – 0.10 Hz. Kernels are shown for an S-wave at an epicentral distance of $80°$ (in b), a P-wave at $80°$ (in c), and an SKS-wave at an epicentral distance of $100°$ (in d). The yellow star indicates the earthquake and the red triangle indicates the receiver. Earthquakes are 400 km deep. The black lines in the center of the kernels are the geometric ray paths.

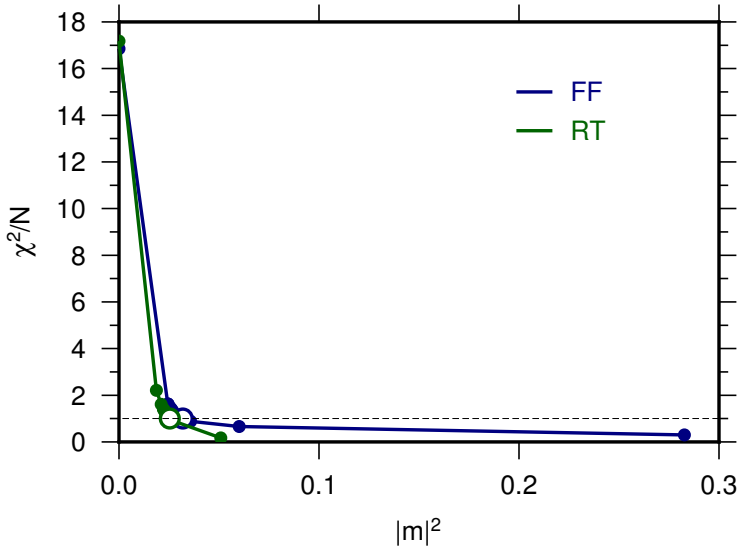

Figure 3.3: The tradeoff curve of misfit versus model norm obtained for plume R1a using network configuration A (see section 3.3.1). Results for FF are shown in blue and results of RT are shown in green. The open circles indicate the 'best' model, for which the model fits the data to within uncertainty (i.e., $\chi^2 = N$). The best model $\mathbf{m}$ is smaller for RT than FF for a given misfit χ^2.

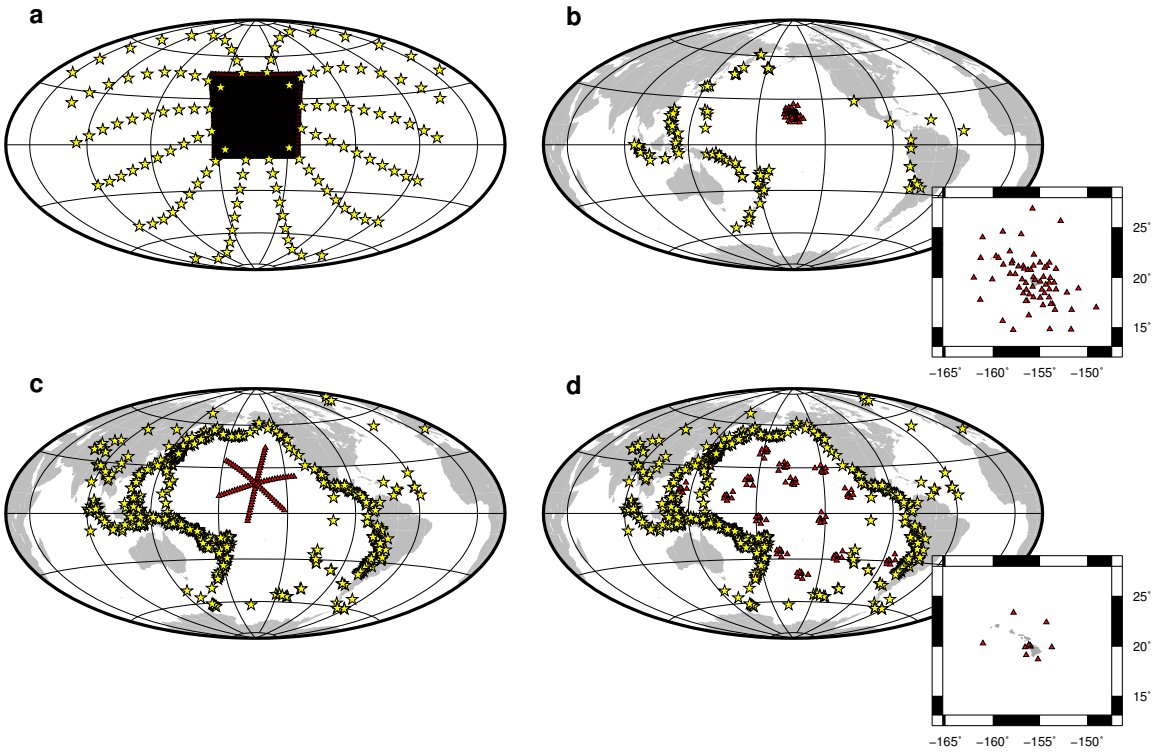

Figure 3.4: Source–receiver geometries used in synthetic tomography experiments. Yellow stars indicate earthquakes and red triangles indicate receivers. (a) represents a scenario in which earthquakes are recorded on a rectangular network at distances D between $30°$ and $120°$ and with uniform azimuthal coverage. The width L of the network is 6,000 km, and the spacing between stations Δx is 100 km. The network geometry shown in (b) is identical to the PLUME geometry. The earthquakes are larger than magnitude 6 between 2012 and 2017. Panels (c) and (d) illustrate hypothetical deployments in the Pacific Ocean. The earthquake locations are taken from the historical seismicity record of events greater than M_W 6 over the previous five years. The network in (c) comprises three intersecting linear arrays with Δx = 200 km. The arrays-of-arrays network shown in (d) is similar to the proposed Pacific Array

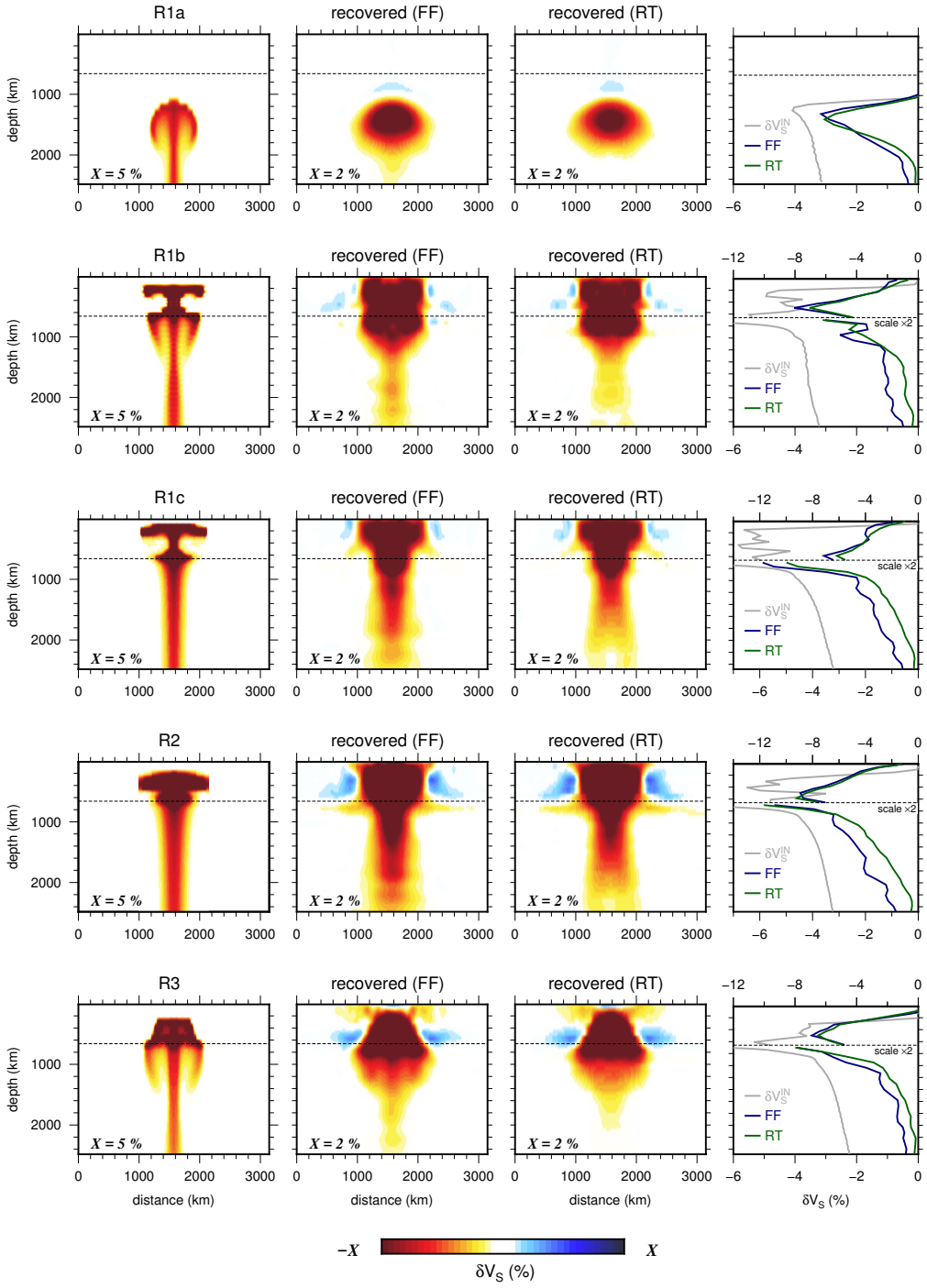

Figure 3.5: Shear velocity structures of the plumes R1, R2, and R3 obtained by inverting S-wave delay times for network geometry A (Figure 3.4a) with L = 6,000 km, Δx = 100 km. The standard deviation of the traveltime uncertainty is $\sigma = 0.1$ s. The first column shows the structures of the input plume models. The second and third columns show the resolved velocity structures using FF and RT, respectively. The dotted line is the 660 discontinuity. The fourth column shows the resolved velocity structure along the plume axis for FF (in blue) and RT (in green), as well as the strength of the input structure δV_S^{IN} (in grey). The anomalies below the 660 are enlarged by a factor of two relative to the upper mantle for clarity.

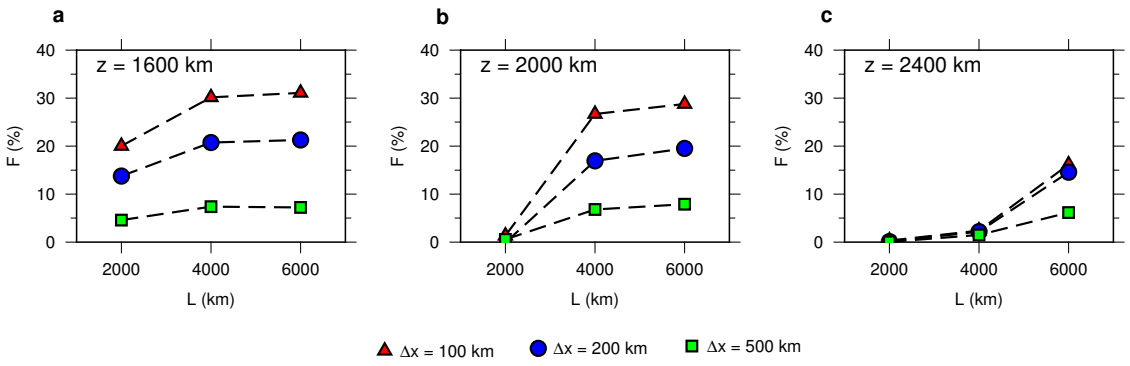

Figure 3.6: The fraction F recovered of the velocity anomaly within the tail of R1b as a function of network width L. F is determined for a station spacing Δx of 100 km (triangles), 200 km (circles), and 500 km (squares) and for three depths along the plume axis: (a) 1,600 km, (b) 2,000 km, and (c) 2,400 km. Delay times are inverted using FF.

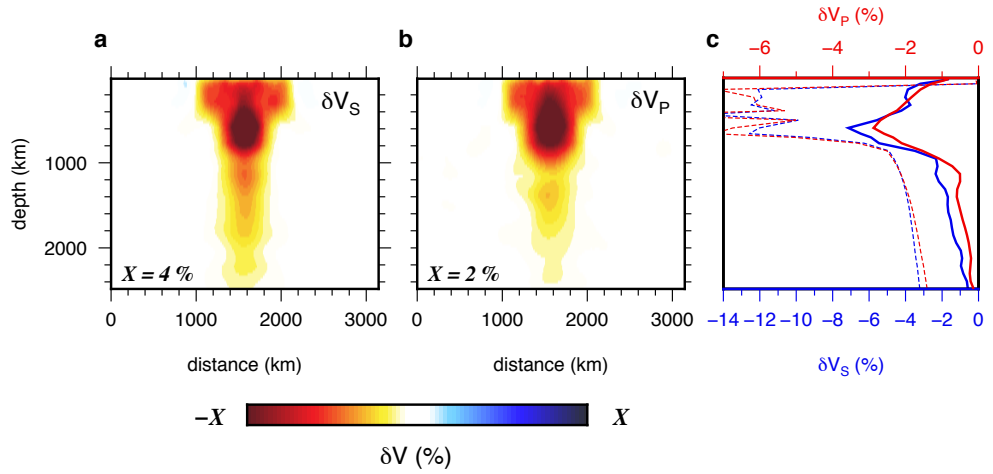

Figure 3.7: Comparison of (a) the resolved S-wave velocity δV_S and (b) the resolved P-wave velocity δV_P structures for plume R1c using the idealized source–receiver geometry and FF theory. The scale X of the colorbar is indicated in the lower left corner. c) shows δV_S (blue) and δV_P (red) along the plume axis. Dashed lines indicate the axial anomaly of the input model.

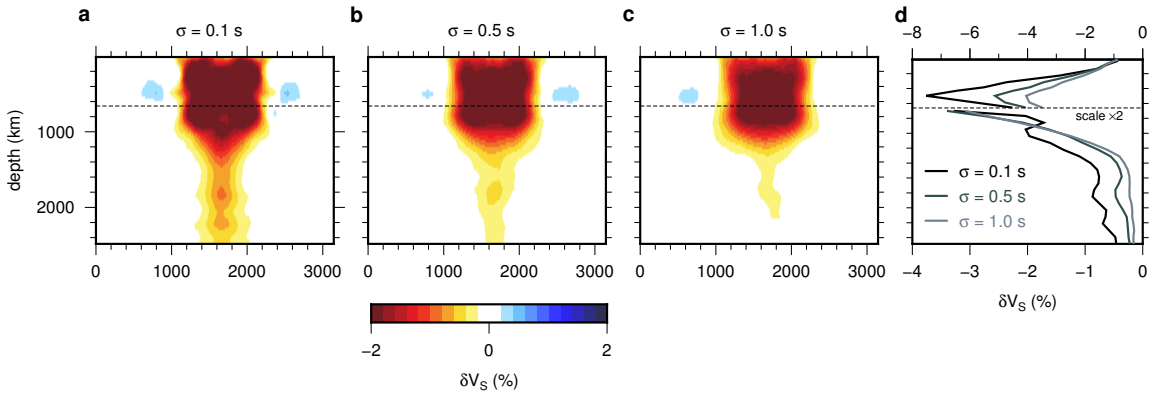

Figure 3.8: Effect of Gaussian noise in the traveltime measurements on tomographic imaging of plumes using FF and S traveltime delays. Panels (a), (b), and (c) show FF S-wave inversion results of R1b, with different values for the standard deviation of Gaussian noise σ. Panel (d) shows the structure of each of the three models along the plume axis. The scale of the x-axis is enlarged by a factor of two in the lower mantle.

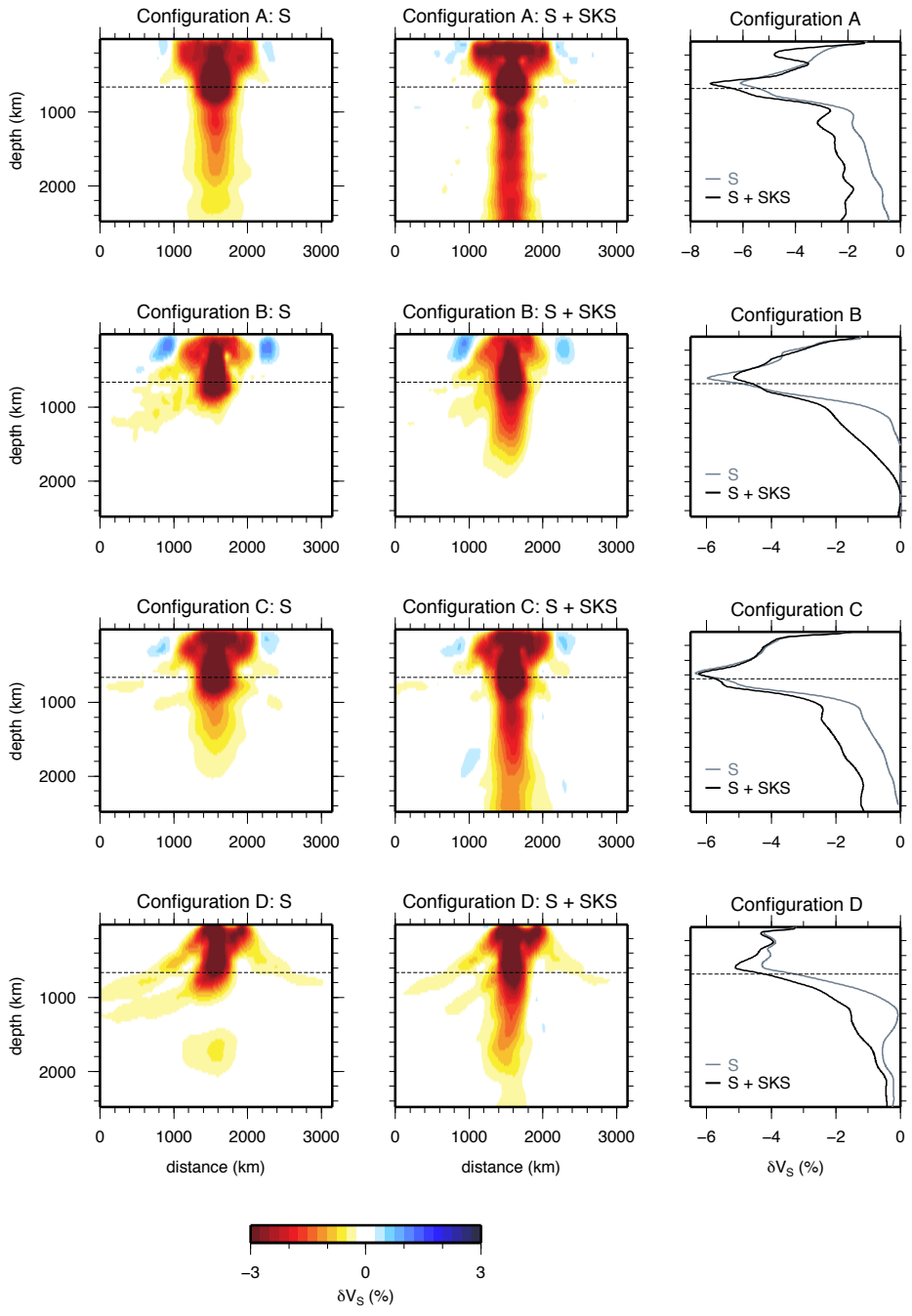

Figure 3.9: Inversions of R1c for all source-receiver configurations using FF. The rows correspond to i) the idealized rectangular grid ii) the PLUME geometry iii) the intersecting linear arrays and iv) the Pacific array. Models in the left column use only S traveltimes and models in the middle column use S and SKS traveltimes. The right column compares inversion results for S and S+SKS along the plume axis.

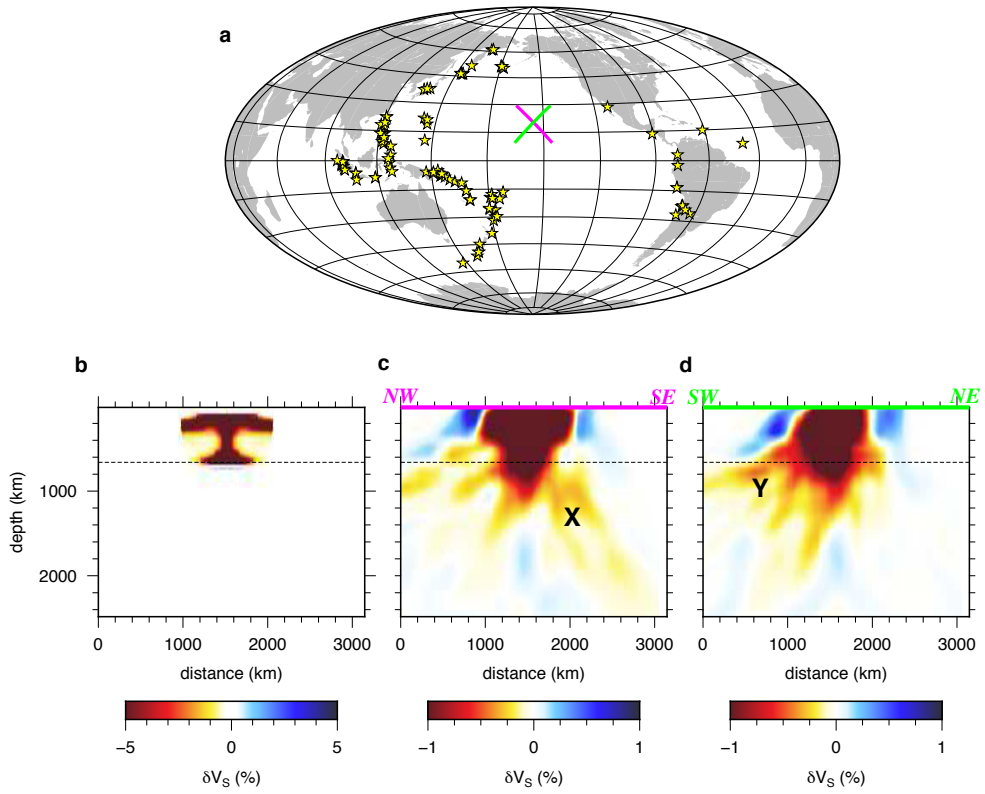

Figure 3.10: Smearing test for the PLUME experiment (i.e., configuration B). S and SKS traveltimes are jointly inverted using FF. a) Earthquake distribution used in the inversion, as well as the locations of cross sections through recovered model. b) Input plume structure, which is the upper mantle expression of R1c (i.e., R1c where the plume tail has been artificially removed). c) NW–SE cross section through the recovered model. The feature labeled 'X' illustrates smearing oriented steeply to the SE due to the prevailing incoming ray direction of South American events. d) SW–NE cross section through recovered model. The feature labeled 'Y' reflects smearing to the SW owing to the prevalence of South Pacific events.

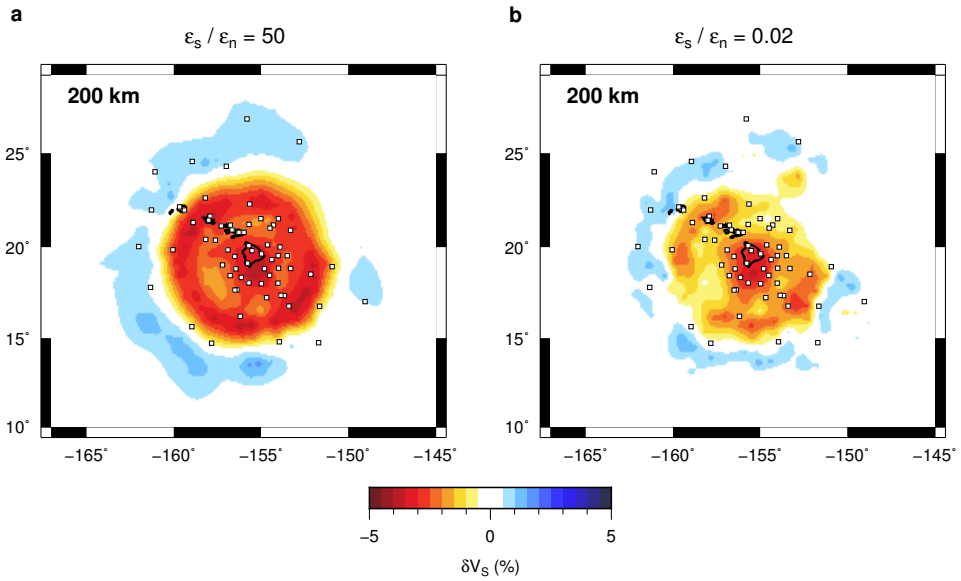

Figure 3.11: Effect of regularization parameters. Inversions shown are for R1b using S and SKS travel times, and the PLUME geometry. Horizontal slices of the model are taken at 200 km depth. In (a) smooth models are preferred ($\epsilon_s/\epsilon_n = 50$), and in (b) small models are preferred ($\epsilon_s/\epsilon_n = 0.02$).

Plume	Ra	ΔT_{CMB} (K)	b	Γ_{660} (MPa K^{-1})
R1	2×10^6	750	$\ln(10^2)$	-2.5
R2	1×10^6	750	$\ln(10)$	0
R3	8×10^5	550	$\ln(10^3)$	-2.5

Table 3.1: Dynamic parameters used in plume simulations. Ra is the thermal Rayleigh number, ΔT_{CMB} is the temperature contrast across the core mantle boundary, b is the temperature dependence of viscosity, and Γ_{660} is the Clapeyron slope of the ringwoodite–bridgmanite phase transition.

CHAPTER 4

Signals of 660-km topography and harzburgite enrichment in seismic images of whole-mantle upwellings *

Abstract

Various changes in seismic structures across the mantle transition zone (MTZ) indicate it may hamper thermal and chemical circulation. Here we show how thermal elevation of the post-spinel phase transition at 660 km depth plus harzburgite segregation below this depth can project as narrow high-velocity anomalies in tomographic images of continuous thermochemical mantle upwellings. Model S40RTS features a narrow high-velocity anomaly of +0.8% near 660 km depth within the broad low-velocity structure beneath the Samoa hotspot. Our analyses indicate that elevation of the 660 phase boundary in a hot pyrolitic plume alone is insufficient to explain this anomaly. An additional effect of harzburgite enrichment is required and consistent with geodynamic simulations that predict compositional segregation in the MTZ, especially within thermochemical upwellings. The Samoa anomaly can be modelled with a 125–175°C excess temperature and a harzburgite enrichment below 660 of least 60% compared to a pyrolitic mantle.

4.1 Introduction

It is well established that the upper mantle transition zone has a profound influence on the structure of mantle flow. Seismic tomography has been successful in imaging the variable descent of subducting slabs into the deep mantle (e.g., *Grand*, 1994; *Sigloch and*

*Chapter 4 is published in Geophysical Research Letters: Maguire, R., Ritsema, J., & Goes, S. (2017). Signatures of 660-km topography and compositional heterogeneity in seismic images of upwellings. Geophysical Research Letters, 119. http://doi.org/10.1002/2017GL073120

Mihalynuk, 2013; *Fukao and Obayashi*, 2013) but tomographic constraints on the origin of mantle upwellings have remained ambiguous (e.g., *Montelli et al.*, 2004; *Wolfe et al.*, 2009; *Styles et al.*, 2011; *French and Romanowicz*, 2015).

In this paper, we investigate the effects of compositional layering in the upper mantle transition zone on images of mantle upwellings. We consider a thermochemical upwelling from the lower mantle that has transported compositionally distinct material into the transition zone (e.g., *Xie and Tackley*, 2004; *Brandenburg and van Keken*, 2007; *Nakagawa et al.*, 2010). The layering originates from thermal perturbations of the 660-km phase boundary (i.e., the 660) and from the segregation of basaltic and harzburgitic components with intrinsically different densities (*Irifune and Ringwood*, 1993). Using a forward modeling approach, we illustrate how anomalous layering near the 660 can project as a high-velocity seismic anomaly embedded within a whole-mantle low-velocity structure and be reminiscent of discontinuous flow across the transition zone.

Figure 4.1a is the working example of our analysis. It shows the shear-velocity structure in the mantle beneath the southwestern Pacific according to S40RTS (*Ritsema et al.*, 2011). The dipping high-velocity anomaly between 10^o and 35^o is the subducting Pacific Plate. A broad low-velocity anomaly extends from the core-mantle boundary to the surface beneath the Samoa hotspot. We interpret this mantle-wide structure as a large-scale mantle upwelling related to hotspot volcanism on Samoa and call it the *Samoa plume* for simplicity. There is a gap in the Samoa plume near the base of the upper-mantle transition zone, manifested as a positive wave speed anomaly with a maximum amplitude of $\delta \mathrm{V_S} = 0.8\%$. We will call this the *Samoa gap* from here on. The Samoa gap may imply that upward mantle flow is blocked near the 660. Here, we hypothesize that the Samoa gap is due to the thermal elevation of the 660 and compositional heterogeneity around the base of the transition zone within a continuous thermochemical upwelling. Our modeling is informed by seismic estimates of 660 topography, geodynamic simulations of mantle mixing, and estimates of image resolution in tomographic model S40RTS.

4.2 Models of the Samoa gap

4.2.1 Temperature induced phase boundary topography

The mineral phase transformation of ringwoodite (ri) to the post–spinel phases bridgmanite (br) plus magnesiowüstite (mw) is responsible for the deepest global seismic discontinuity in the upper mantle at 660 km depth. Recent estimates indicate that this transition has a negative Clapeyron slope $-2.9 \leq \gamma_{660} \leq -2.1$ MPa K^{-1} (*Ye et al.*, 2014). Hence, a

temperature increase in the upper mantle of $\Delta T = 250°\text{C}$ would elevate the 660 by 13–18 km. Analyses of P and S wave reflections (e.g., *Flanagan et al.*, 1998; *Gu and Dziewonski*, 2002; *Deuss*, 2009) and conversions (e.g., *Schmandt et al.*, 2012; *Mulibo and Nyblade*, 2013; *Jenkins et al.*, 2016) indicate that topography on the 660 in the mantle is as high as 30 km.

In seismic images (Figure 4.1b), a locally elevated 660 would be visible as a thin high-velocity anomaly with respect to a mantle in which the 660 is unperturbed. Its vertical width is equivalent to the elevation of the 660 and the velocity contrast is determined by the shear velocity increase across the 660. The expected concurrent depression of the 410 due to the exothermic phase transition around that depth would produce a low-velocity anomaly. We ignore such an anomaly because it would likely not be observable within a large-scale low-velocity anomaly (i.e., the Samoa plume).

4.2.2 Basalt depletion below the 660

Melting of mantle peridotite generates a stratified oceanic lithosphere with layers of basalt and harzburgite. After plates subduct these two components are recycled back into the mantle to become a folded and stretched mechanical mixture (see *Xu et al.* (2008) for a discussion). Since harzburgite is denser than mid-ocean ridge basalt for a narrow depth range ($\sim$ 100 km) beneath the 660, the two components may segregate near the 660 (*Irifune and Ringwood*, 1993). As a result the lower mantle will have a harzburgite enriched composition between about 660 and 800 km depth and basalt enrichment directly above 660. Numerical simulations of thermochemical mantle convection (e.g., *Xie and Tackley*, 2004; *Brandenburg and van Keken*, 2007; *Nakagawa et al.*, 2010) demonstrate that a compositional gradient forms in the mantle and that basalt–harzburgite partitioning can be particularly strong within upwelling regions of the mantle and when γ_{660} or the density contrast between basalt and harzburgite are high (e.g., *van Summeren et al.*, 2009). The shear velocity of a basalt-enriched composition above 660 will be lower than the background mantle and would contribute to the overall low velocities of a hot upwelling. By contrast, the shear speed in a harzburgite-enriched layer beneath the 660 is higher than in a mantle with a pyrolite composition, as illustrated in Figure 4.1c.

4.3 Analysis

4.3.1 Mineral physics constraints

Experimental mineral physics results constrain our seismic models of the elevation of the 660 and harzburgite enrichment in the uppermost lower mantle. We compute theoretical profiles of shear velocity as described in *Cobden et al.* (2008), i.e., using Perple_X (*Connolly*, 2005), with the thermodynamic parameter database from *Stixrude and Lithgow-Bertelloni* (2011) and estimates of temperature and pressure-dependent anelasticity from *Goes et al.* (2004). As in *Xu et al.* (2008), the mantle is composed of the Na-Ca-Fe-Mg-Al-Fi (i.e, NCFMAS) oxides and regarded as a mechanical mixture of basalt and harzburgite in proportions f and 1–f, respectively. We calculate the reference profile for an adiabat with a potential temperature of 1300°C, suitable for the convective MORB-source mantle, and for a basalt fraction $f = 0.2$, roughly equivalent to the composition of pyrolite. We compute the elevation of the 660 due to a temperature increase using a Clapeyron slope of $\gamma_{660} = -2.9$ MPa K^{-1} and velocity anomalies due to changes in the composition of the uppermost lower mantle by changing f.

Figure 4.2a compares profiles of shear velocity for basalt fractions f between 0 and 0.4 and an adiabat for the reference potential temperature of 1300°C. In a purely harzburgitic mantle (i.e., $f = 0$), the 660 phase transition is entirely controlled by the $ri \rightarrow bm + mw$ transition with a shear velocity jump of 9.0% at the 660. The shear velocity is up to 2% higher than in a pyrolitic mantle between 660 km and 760 km depth. In a mechanical mixture of basalt and harzburgite (i.e., $f > 0$), the phase transformation at the 660 is distributed over a finite pressure range because the $gt \rightarrow mw$ in basalt occurs near 760 km depth. The shear velocity jump at the 660 decreases with increasing basalt fraction f from 7.2% for $f = 0.2$ to 5.4% for $f = 0.4$. Figure 4.2b compares profiles of shear velocity for adiabats with potential temperatures between 1300°C (our reference geotherm) and 1600°C (expected within a hot mantle upwelling). The basalt fraction f = 0.2. The elevation of the 660 increases with temperature but the velocity increase across the 660 is not very sensitive to temperature.

4.3.2 Model parameterization

We parameterize the elevation of the 660 and a layer below the 660 with a harzburgite-enriched composition as narrow rectangular blocks. The rectangular blocks have horizontal side lengths of 1000 km which corresponds to the minimum horizontal scale that can be resolved by S40RTS. The vertical thickness H and the uniform velocity perturbation δV_{IN}

are free parameters.

For a model that represents a 660 perturbation, H corresponds to the elevation of the 660. The shear velocity jump $\delta \mathrm{V_B}$ at the phase boundary (see Figure 4.2c) and the shear velocity reduction $\delta \mathrm{V_T}$ due to the increased temperature determine $\delta \mathrm{V_{IN}}$ (see Figure 4.2d). $\delta \mathrm{V_{IN}} = \delta \mathrm{V_B} + \delta \mathrm{V_T}$. For a model that represents a harzburgite-enriched layer beneath the 660, H is the layer thickness and the shear velocity anomaly $\delta \mathrm{V_{IN}}$ depends on the composition (δV_C) and temperature $\delta \mathrm{V_T}$. Thus, $\delta \mathrm{V_{IN}} = \delta \mathrm{V_C} + \delta \mathrm{V_T}$, where $\delta \mathrm{V_C}$ and $\delta \mathrm{V_T}$ have opposite signs. If the layer is pure harzburgite ($f = 0$) and there is no temperature anomaly, then $\delta \mathrm{V_{IN}}$ is about 2%. If ΔT exceeds about 200°C, the shear velocity in the harzburgite-enriched layer is lower than in the reference model and the layer may not be visible.

4.3.3 Tomographic filtering

To estimate how phase boundary topography and harzburgite enrichment in the uppermost lower mantle would be imaged tomographically, we use the model resolution matrix $\mathcal{R}$ of S40RTS. We first project the test structure (i.e., the rectangular block) into the model parameterization of S40RTS, which consists of spherical harmonics up to degree 40, and 21 vertical spline basis functions. After projection into S40RTS parameterization the linear operator $\mathcal{R}$ is applied to produce a tomographically filtered version of the input model. Application of $\mathcal{R}$ distorts and dampens the input model due to incomplete and heterogeneous data coverage, and model regularization, but it does not include the effects of inaccurate forward modeling (*Ritsema et al.*, 2007).

Figure 4.3 shows how a 30-km elevation of the 660 (in Figure 4.3a) and a 100-km thick layer of compositional heterogeneity below the 660 (in Figure 4.3b) would be imaged in S40RTS. After projection into S40RTS parameterization (Figure 4.3c and 4.3d) the high-velocity rectangular blocks are thicker and the velocity anomalies are weaker because the spacing of the vertical splines in S40RTS is large compared to H. The amplitude reduction is strongest for the thinnest layer. After filtering (Figure 4.3e and 4.3f), the velocity perturbations have been reduced further by a factor of about two.

4.4 Results

The contours in Figure 4.4 show how the peak recovered velocity anomaly, which we refer to as $\delta \mathrm{V_{OUT}}$, varies as function of H and $\delta \mathrm{V_{IN}}$. $\delta \mathrm{V_{OUT}}$ depends linearly on $\delta \mathrm{V_{IN}}$ and non-linearly on H. It is highest for the thickest layers when re-parameterization affects the

amplitude reduction the least.

In Figure 4.4a, the highest value for δV_{OUT} of 1.7% is obtained when the 660 is elevated by 30 km and the shear velocity jump across the 660 is 10%. The Samoa gap of 0.8% (see Figure 4.1) can be explained if the 660 is elevated by at least 15 km. For a shear velocity jump as small as 5%, the 660 elevation must be 25 km or more. The smallest shear velocity perturbation δV_{IN} in combination with the smallest H for which $\delta V_{OUT} = 0.8\%$ are 7% and 18 km, respectively. The combinations of H and δV_{IN} consistent with a temperature induced elevation of the 660, as discussed in Section 4.3.1, are indicated by dashed lines in Figure 4.4a. We consider a mantle mixture with a pyrolitic composition ($f = 0.2$) and a harzburgitic mantle ($f = 0$) and assume that γ_{660} = -2.9 MPa K^{-1}. The highest values of δV_{OUT} are obtained when ΔT is about 200–250°C, depending on composition. Within this temperature range, the 660 elevation is about 15–20 km. δV_{OUT} approaches 0.8% if the mantle is composed of pure harzburgite but it is smaller than 0.5% for a pyrolitic mantle.

Figure 4.4b shows that the Samoa gap of 0.8% can be better explained by a harzburgite-enriched layer with a thickness of at least 50 km. The highest value for δV_{OUT} of 1.7% is obtained when shear velocity jump is 2.1% higher than in the ambient mantle within 100-km thick layer below the 660. The smallest values for δV_{IN} and H for which $\delta V_{OUT} = 0.8\%$ are 1.5% and 70 km, respectively. The shear velocity increase δV_{IN} in this layer decreases with increasing basalt fraction f. If the layer has a thickness of 100 km, the harzburgite fraction must be higher than 0.925 to match the Samoa gap of 0.8%.

4.5 Discussion and Conclusions

In this paper, we have demonstrated that thermal elevations of the post-spinel phase transition at 660 km depth and basalt segregation at the top of the lower mantle can project as narrow high-velocity anomalies in tomographic images of continuous thermochemical mantle upwellings. Even though our analysis used post–spinel Clapeyron slopes on the high end of those determined from mineral physics (*Ye et al.*, 2014; *Hirose*, 2002; *Weidner and Wang*, 1998), the elevation of the 660 alone is not sufficient to explain the relatively high shear velocity in the Samoa gap. This is because of the competing effects of the phase transition and temperature on shear velocity in a pyrolytic mantle. A harzburgite-enriched layer within the uppermost lower mantle is an essential feature of the model. It is consistent with geodynamic simulations of mantle mixing which predict strong compositional layering around the 660 (e.g., *Xie and Tackley*, 2004; *Nakagawa et al.*, 2010; *van Summeren et al.*, 2009). It may also help explain the change in the pattern of seismic velocity heterogeneity across the 660 (e.g., *Gu et al.*, 2001; *Ritsema et al.*, 2004).

In Figure 4.5 we show which combinations of mantle temperature anomaly ΔT and composition below 660 can explain the high velocity anomaly of 0.8% in the gap within the thermochemical Samoa plume (See Figure 4.1). The uppermost lower mantle is enriched in harzburgite due to compositional segregation across the 660. Assuming a Clapeyron slope for the 660 phase boundary of γ_{660} = -2.9 MPa K^{-1}, we find that if the average harzburgite fraction is > 0.925 (i.e., a basalt fraction of $f < 0.075$) between 660 and 760 km depth, a temperature anomaly of ΔT = 125–175°C in the transition zone can explain the Samoa anomaly. Although phase boundary topography plus high-velocity material below or around 660 km depth are required to match the Samoa gap, estimates of composition and thermal anomaly are subject to substantial uncertainties associated with the mineral physics constraints on transition-zone shear velocities (*Stixrude and Lithgow-Bertelloni*, 2011; *Cammarano et al.*, 2003).

Our analysis has focused on the mantle beneath the Samoa hotspot where image resolution in the transition zone is relatively high and where the effects are most obvious. The Samoa plume is also apparent in global tomographic models GyPSuM-S (*Simmons et al.*, 2010) and SEMUCM-WM1 *French and Romanowicz* (2015) (see Figure 4.6), which are based on different data sets and modeling strategies. However, a quantitative comparison of image resolution for all models is necessary to determine whether these tomographic images are consistent with S40RTS and our analysis.

While this study has concentrated on anomalies caused by phase boundary effects in regions of mantle upwelling, we expect that within a cold slab the $ri \rightarrow bm+mw$ transition will occur at a greater depth, and thus introduce a thin low wavespeed anomaly. The Pacific slab anomaly (Figure 4.1a) is diminished by about 0.5% near 660, which is consistent with this interpretation. Figure 4.4a indicates that if the average slab composition is close to pyrolite, a velocity anomaly of 0.5% can be explained by a thermally induced phase boundary deflection of 15 km, corresponding to a temperature decrease within the slab of $\Delta\mathrm{T} = 200^\circ$ C.

If harzburgite-enrichment is important in the mantle, we should expect to see high-velocity anomalies in other regions of mantle upwelling. Anomalies similar to the gap in the Samoa plume are indeed apparent beneath the Azores, Canary, Galapagos, and Hawaii hotspots (Figure 4.7) although they are much weaker and not as obviously layered, most likely due to the relatively poor tomographic image resolution in the transition zone beneath regions far from the western Pacific subduction zones (e.g., *Ritsema et al.*, 2004; *Houser et al.*, 2008) (Figure 4.8).

While we suggest that high-velocity layering within broad low seismic velocity anomalies is consistent with dynamically predicted basalt–harzburgite segregation, this prediction

depends on the post-spinel Clapeyron slope (*Weinstein*, 1992), mantle viscosity (*Brandenburg and van Keken*, 2007) and the relative densities of basalt, harzburgite and pyrolite as a function of pressure and temperature, each with significant uncertainties. These parameters determine whether or not global compositional stratification near 660 develops over the convective timescale of Earth (*Nakagawa et al.*, 2010). Further work should test our observation and interpretation of the compositional segregation within mantle plumes.

4.6 Figures - Chapter 4

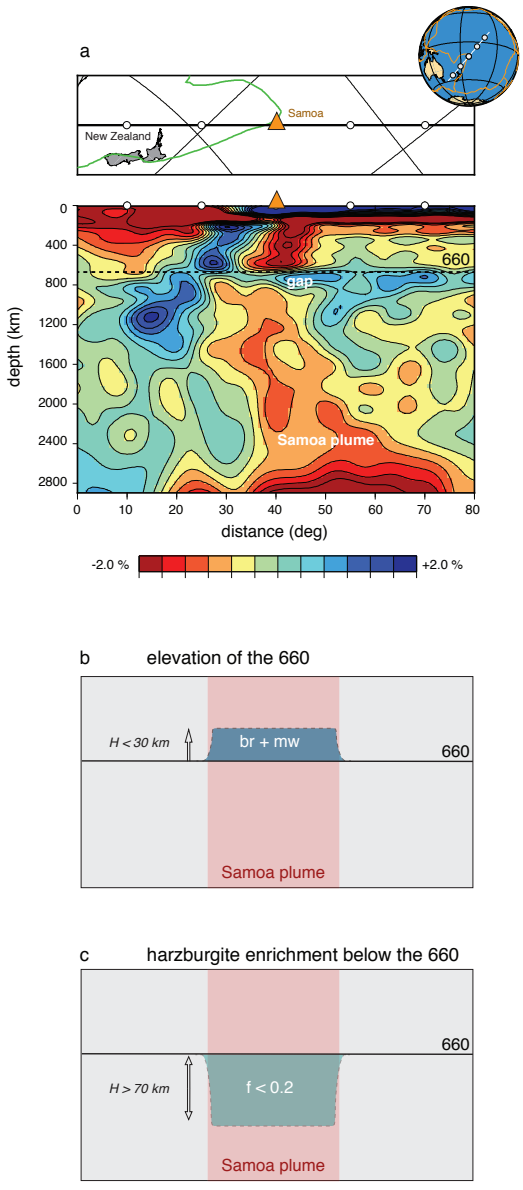

Figure 4.1: (a) Vertical, SW–NE oriented cross-section through the shear velocity model S40RTS centered on the Samoa hotspot. The Samoa plume is a broad low shear velocity anomaly from the core-mantle boundary to the surface and assumed to be a hot thermal upwelling. A high-velocity anomaly breaks the Samoa plume near the 660-km discontinuity (dashed line). This feature is called the Samoa gap in this paper. (b) Sketch of the expected 660-km phase boundary elevation due to the increased temperature in the upper mantle beneath Samoa. (c) Sketch of a layer in the uppermost lower mantle with a harzburgite-enriched composition. The 660 elevation (in b) and the harzburgite-enriched layer (in c) may be observed as high-velocity anomalies.

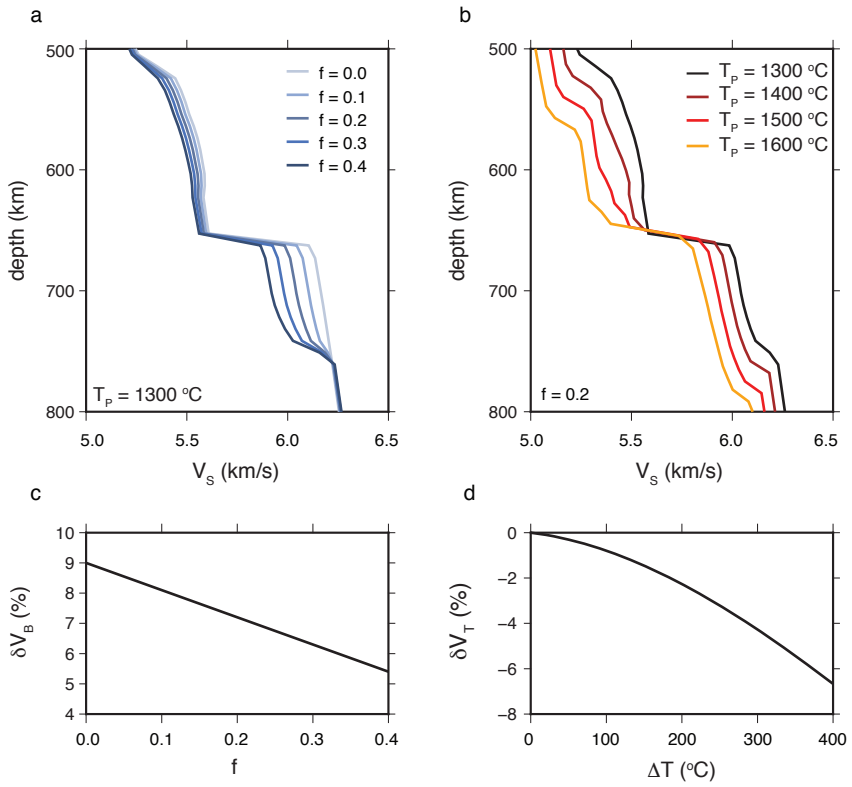

Figure 4.2: Shear velocity profiles calculated for mechanical mixtures of basalt and harzburgite in proportions f and $1–f$, respectively. (a) The basalt fraction f is varied from 0 to 0.4. The geotherm is an adiabat with a potential temperature of 1300°C. (b) The potential temperature is varied between 1300°C and 1600°C. The basalt fraction $f = 0.2$. (c) The shear velocity increase $\delta \mathrm{V_B}$ across the 660 as a function of basalt fraction f. (d) The shear velocity decrease $\delta \mathrm{V_T}$ in the uppermost lower mantle as a function of temperature increase $\Delta \mathrm{T}$.

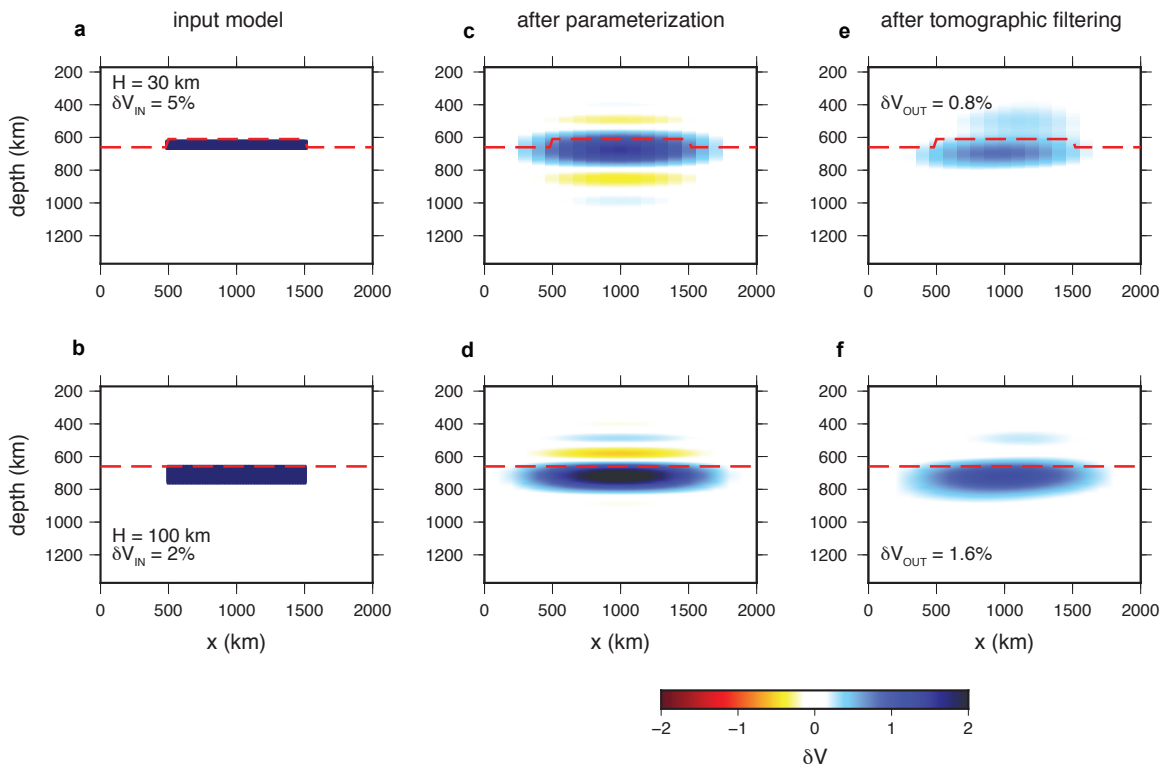

Figure 4.3: Resolution test showing how a rectangular block-shaped velocity anomaly above the 660 (in a) and below the 660 (in b) would be imaged in S40RTS. The anomaly has horizontal side lengths of 1000 km. In (a) the thickness $H = 30$ km and $\delta \mathrm{V_{IN}} = 5\%$. In (b) the thickness $H = 100$ km and $\delta \mathrm{V_{IN}} = 2\%$. The anomalies are drawn with vertical exaggeration for clarity. Panels (c) and (d) show these anomalies after projection into S40RTS parameterization. Panels (e) and (f) show the anomalies after re-parameterization and filtering by $\mathcal{R}$. The highest recovered anomaly in tomographically filtered model is $\delta \mathrm{V_{OUT}}$.

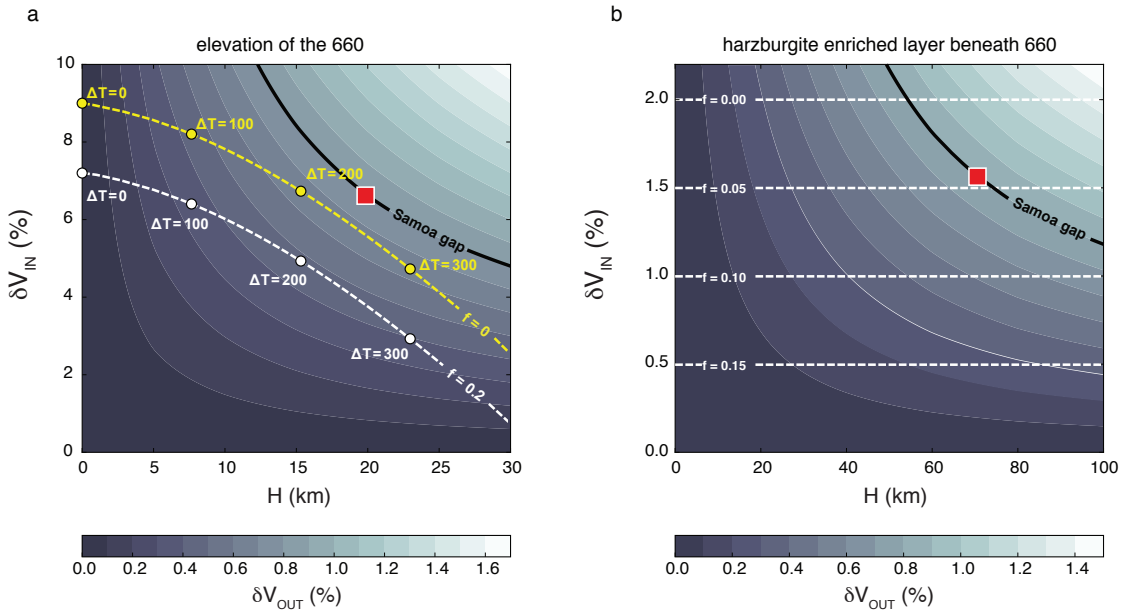

Figure 4.4: Contours of the peak recovered velocity anomaly $\delta \mathrm{V_{OUT}}$ obtained by tomographic filtering of input models using $\mathcal{R}$. An input model is defined by the assumed layer thickness H (along the x-axis) and velocity anomaly $\delta \mathrm{V_{IN}}$ (along the y-axis) and represents (in a) an elevation of the 660 or (in b) a layer in the uppermost lower mantle with a harzburgite-enriched composition. The 0.8% contour corresponds to the Samoa gap near the 660 within the Samoa plume (see Figure 1). The red square is a corner point where $\delta \mathrm{V_{OUT}} = 0.8\%$ for the smallest values of $\delta \mathrm{V_{IN}}$ and H. In (a), the dashed lines show the combinations of $\delta \mathrm{V_{IN}}$ and H consistent with an elevation of the 660 due to the presence of a temperature $\Delta \mathrm{T}$, indicated with solid circles. The yellow and white lines correspond to assumed basalt fractions of $f = 0$ and $f = 0.2$, respectively. In (b), the dashed lines show the values of $\delta \mathrm{V_{IN}}$ consistent with harzburgite enrichment below the 660 for $f = 0$, $f = 0.05$, $f = 0.10$, and $f = 0.15$.

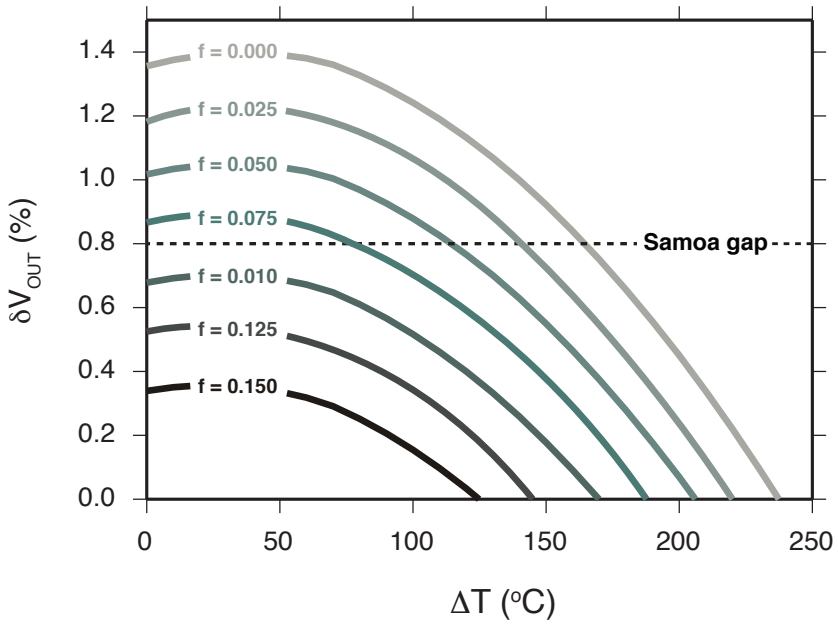

Figure 4.5: The expected values of $\delta \mathrm{V_{OUT}}$ in the Samoa gap for a model of the Samoa plume as a continuous thermochemical upwelling across the transition zone that has elevated the 660 and includes a 100-km thick zone below the 660 with a harzburgite-enriched (basalt-depleted) composition. $\delta \mathrm{V_{OUT}}$ is determined as a function of the temperature anomaly $\Delta \mathrm{T}$ and for variable basalt fraction. in the uppermost lower mantle.

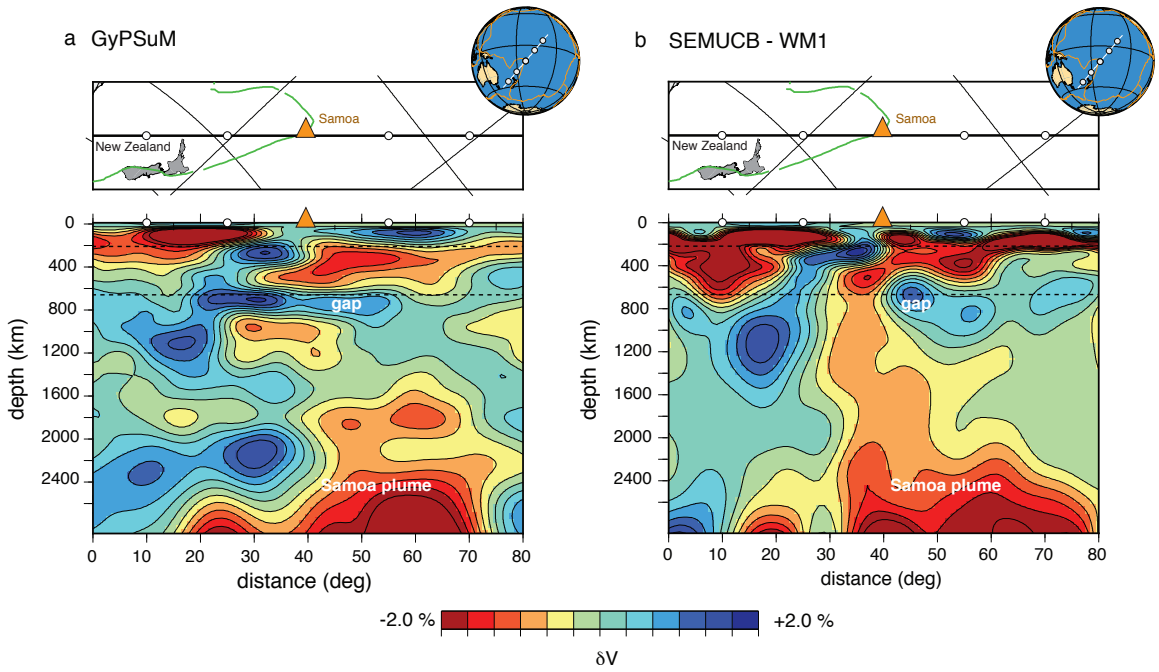

Figure 4.6: Vertical, SW–NE oriented cross-section through the shear velocity models (a) GyPSuM-S and (b) SEMUCB-WM1 centered on the Samoa hotspot. The 660-km discontinuity is marked by a dashed line. See Figure 1 for comparison with S40RTS.

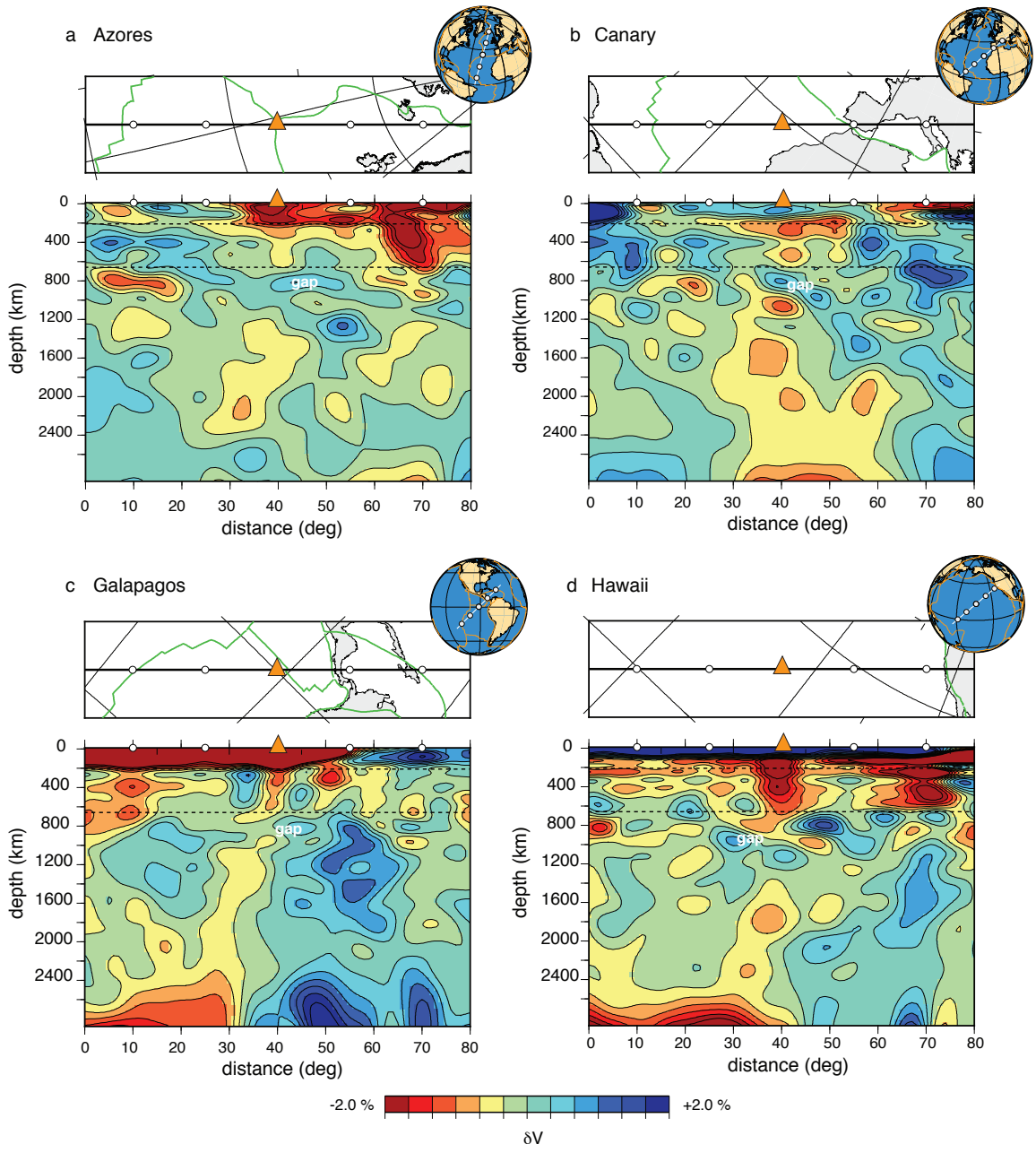

Figure 4.7: Cross sections through shear velocity model S40RTS beneath the Azores (a), Canary (b), Galapagos (c), and Hawaii (d) hotspots. Low wavespeed anomalies beneath each of these hotspots may represent upwellings from the deep mantle. Each cross section shows a gap in the low wavespeed anomaly near 660, potentially due to elevation of the 660, or basalt depletion at the top of the lower mantle.

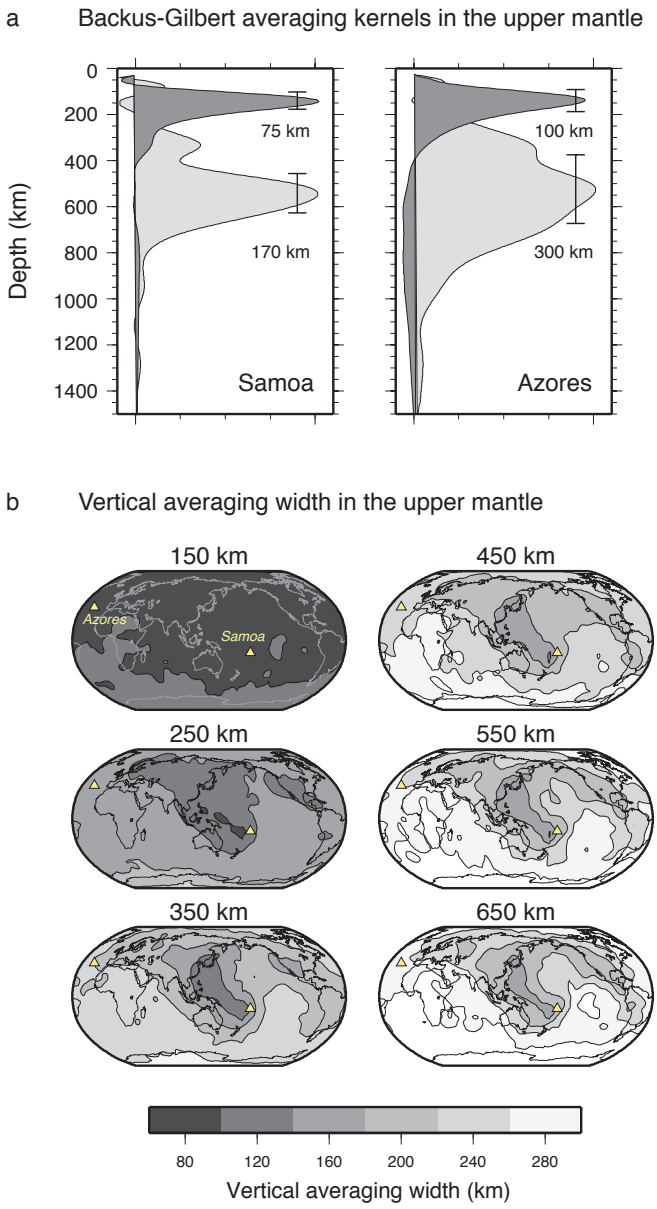

Figure 4.8: (a) S40RTS resolution kernels indicating how a velocity anomalies at 150 km and 550 km depth represent weighted averages of the structure in the mantle. The vertical width of the kernels is a measure of vertical resolution. Here, the width is defined by the interval for which the area under the curve is 50% of the total area. For Samoa, vertical resolution is 75 km and 170 km at depth of 150km and 550 km, respectively. For Azores, these values are 100 km and 300 km. (b) Geographic variations of vertical resolution of S40RTS, as quantified in (a), at six depths in the mantle.

CHAPTER 5

Investigating the petrological variation in LLVPs using seismic tomography and mantle mixing simulations

Abstract

The tomographically imaged large low velocity provinces (LLVPs) beneath Africa and the Pacific may play an important role in mantle convection, yet they remain poorly understood. In this study, we test the hypothesis that LLVPs represent piles of recycled oceanic crust that have been entrained in thermal upwellings at the core-mantle-boundary by comparing LLVPs in tomography model S40RTS (*Ritsema et al.*, 2011) to the global mantle mixing simulations of *Brandenburg et al.* (2008). To account for the limited resolution of tomographic imaging, we tomographically 'filter' the geodynamic models to the same spatial resolution as S40RTS. Dynamic simulations develop thermochemical piles that bear strong resemblance to LLVPs if the excess density of oceanic crust is about 6% or higher. More generally, we find eclogite enrichment alone can not explain tomographic observations of LLVPs. If LLVPs represent piles of recycled oceanic crust, they must be accompanied by a temperature elevated by at least 400 K.

5.1 Introduction

The seismic structure of Earth's lowermost mantle is dominated by two continent-sized regions of anomalously low wave speed beneath Africa and the Pacific (Figure 5.1). These regions are commonly referred to as large low velocity provinces or LLVPs (see *Garnero et al.* (2016) for a review). The two LLVPs occupy almost one third of the total area of the core-mantle boundary (CMB) and are characterized by shear wave (δV_S) compressional

wave (δV_P) velocity reductions of about 2% and 1%, respectively. In some regions, the ratio $R = \delta \mathrm{V_S}/\delta \mathrm{V_P}$ can be larger than $R = 4$ in LLVPs (e.g., *Koelemeijer et al.*, 2016).

LLVPs have been recognized in seismic images of the lower mantle for more than 30 years (e.g., *Dziewonski*, 1984), yet their origin remains mysterious. The growing consensus is that LLVPs represent piles of anomalously warm and compositionally distinct material. However, a purely thermal origin, in which LLVPs represent broad super-plume upwellings, or clusters of narrow plumes, cannot be ruled out because it is challenging to distinguish the thermal and compositional contributions to the seismic signature of LLVPs. Arguments for a compositional component are based primarily on three lines of evidence. First, the high value of R within LLVPs, as well as a negative correlation between bulk and shear velocity are inconsistent with a purely pyrolitic composition. Second, LLVPs appear to have sharp edges (e.g., *Ritsema et al.*, 1998; *Ni et al.*, 2002; *Zhao et al.*, 2015), which would not be expected if their boundaries are controlled by heat diffusion. Third, normal-mode (e.g., *Ishii and Tromp*, 1999; *Trampert*, 2004; *Moulik and Ekström*, 2016) and solid-Earth tide (*Lau et al.*, 2017) data indicate that LLVPs are intrinsically more dense than the surrounding mantle, suggestive of a distinct composition, although Stoneley mode data suggest otherwise (*Koelemeijer et al.*, 2017).

There are several possible explanations that could account for a distinct composition within LLVPs. One possibility is that LLVPs are warm piles of recycled oceanic crust that has accumulated above the core. If the recycled crust has an intrinsically higher density than the surrounding mantle, thermochemical piles may be stable over billions of years (e.g., *Mulyukova et al.*, 2015). Alternatively, LLVPs might represent a dense layer of primitive material (for example the crystallized remnants of basal magma ocean (*Labrosse et al.*, 2007)), that has been reworked into piles by the cumulative history of subduction (*McNamara and Zhong*, 2005).

Here we explore the first possibility. Our models of LLVPs are based on mantle mixing simulations by *Brandenburg et al.* (2008), which develop anomalously hot piles of eclogite above the CMB. To facilitate direct comparison between dynamic models and tomographic images, we convert temperature and compositional fields to seismic velocity using mineral physics constraints and filter the resultant model to the same spatial resolution as tomographic model S40RTS (*Ritsema et al.*, 2011).

Previous studies have tested various models of LLVPs using a tomographic filtering approach. *Schuberth et al.* (2009) argued that isochemical convection models with strong core heating develop features that bear strong resemblance to LLVPs after tomographic filtering. *Bull et al.* (2009) suggest that LLVPs are broadly consistent with models in which a dense layer at the core mantle boundary is swept into a pile by recent (since 119 Ma)

subduction. However, they also find that thermochemical piles are indistinguishable from clusters of thermal plumes after tomographic filtering. *Davies et al.* (2015) use a similar approach and find that the seismic characteristics of LLVPs are most consistent with purely thermal structures, and that compositional variability plays a passive role in lower mantle dynamics. Our work builds on these previous studies by exploring whether or not LLVPs are consistent with predicted features that develop in thermochemical mixing simulations, and if compositional heterogeneity within LLVPs can be tomographically resolved.

5.2 Geodynamic and seismic modeling

5.2.1 Thermochemical convection simulations

We use the mantle mixing simulations of *Brandenburg et al.* (2008) to estimate the temperature, spatial scales, and composition of thermochemical piles. These numerical simulations solve the incompressible form of the equations governing mantle flow with infinite Prandtl number in a cylindrical geometry with force balanced plates. The force balance formulation (*Gable et al.*, 1991) mimics plate tectonic behavior by ensuring persistent zones of divergence and convergence at the surface. The convective vigor, as measured by plate velocities and surface heat flow, is similar to the modern day Earth. The evolution of mantle composition is tracked using a particle tracing method in which eclogite tracers are assigned an excess density $\delta\rho_E$ relative to the surrounding mantle. The compositional field f is formulated such that harzburgite corresponds to $f = 0.0$, fertile peridotite corresponds to $f = 0.125$, and eclogite corresonds to $f = 1.0$. When fertile mantle approaches a melting zone beneath spreading ridge, melting is simulated by extracting tracers to the surface where they accumulate to form a layer of oceanic crust. The oceanic crust and underlying depleted hazrbugitic residue is recycled back into the mantle at subduction zones. When basaltic material (i.e., eclogite) is more dense than the ambient mantle, it settles to the core where it can form thermochemical piles.

Figure 5.2 shows snapshots of the temperature (left column) and composition (middle column) of mantle mixing simulations after 4.5 Gyr of convection, for various values of excess eclogite density $\delta\rho_E$. Warm thermochemical piles do not develop when $\delta\rho_E \leq 4\%$ (see Figure 5.2A). Instead, the structure at the CMB is characterized by cold slabs and narrow plume upwellings. Thin plumes occasionally develop in close proximity to one another, which could potentially be imaged as LLVPs. When $\delta\rho_E \geq 6\%$, subducted oceanic crust begins to accumulate above the core mantle boundary, where it is swept into pile structures by mantle flow (see Figure 5.2B–D). The temperature within the piles (or

plumes) is elevated by as much as 1000 K. Their widths L, heights H, and compositions f depend on $\delta\rho_E$. When $\delta\rho_E = 6\%$, the piles are short ($H \sim 300$ km), and broad ($L > 3000$ km). For the $\delta\rho_E = 8\%$ case, the piles are taller ($H \sim 600$ km), slightly shorter wavelength. When $\delta\rho_E = 10\%$, the tallest structures develop, with $H \geq 1500$ km. In all cases where piles develop there is a basalt enrichment of $f = 0.2$ or greater. The characteristics of thermochemical piles in each simulation are summarized in Table 5.1.

5.2.2 Seismic velocity modeling

Our models of seismic velocity are based on forward calculations of the elastic properties of mechanical mixtures of MORB and harzburgite (e.g., *Xu et al.*, 2008). We use the code Perple_X (*Connolly*, 2005), which is based on thermodynamic first principles to calculate stable mineral assemblages as well as their seismic wavespeeds. The bulk compositions of MORB and harzburgite are defined by proportions of the oxides Na_2O, CaO, FeO, MgO, Al_2O_3, and SiO_2. We use the MORB composition of *Workman and Hart* (2005) and the harzburgite composition of *Baker and Beckett* (1999) (see Table 5.2). The anharmonic seismic wavespeeds are corrected for frequency dependent effects of attenuation using attenuation model Q7g (e.g., *Maguire et al.*, 2016).

We convert the temperature and compositional fields from dynamic simulations into seismic velocity using the following steps. First, we convert potential temperature to absolute temperature using a set of adiabats (i.e., isentropes) computed for a pyrolite composition. This step is required because geodynamic simulations are performed using the Boussinesq (i.e., incompressibility) approximation. Next, we scale the absolute temperature field by 0.76 such that temperatures in the upper mantle are between 1500–1700 K, which is consistent with estimates of mantle potential temperature from mid-ocean-ridge basalts (e.g, *Herzberg et al.*, 2007). Temperatures at the surface and CMB are 300 K and 4000 K respectively. We then compute shear velocity V_S as a function of pressure P, temperature T and f for all points in the model, The shear velocity anomaly δV_S is taken relative to the radial average and is shown for each simulation in the right column of Figure 5.2. In the upper half of the mantle, cold downwellings dominate the seismic structure. At the CMB high-velocity ($\delta V_S > 5\%$) anomalies represent accumulations of slab material. Within the plumes or piles, δV_S exceeds -5% slow. Before filtering, these shear velocity anomalies are more than twice as strong as in S40RTS.

5.2.3 Tomographic filtering

The solution of the linearized tomographic inverse problem can be written as

$$\mathbf{m} = \mathbf{G}^{\dagger}\mathbf{d}, \tag{5.1}$$

where $\mathbf{m}$ is the tomographic model of wavespeed variation, $\mathbf{d}$ is the vector of seismic observations, and $\mathbf{G}^{\dagger}$ is the generalized inverse of the system matrix $\mathbf{G}$ that describes the forward theory. When $\mathbf{G}^{\dagger}$ is known explicitly, for example by singular value decomposition, we can compute the resolution operator $\mathcal{R} = \mathbf{G}^{\dagger}\mathbf{G}$. $\mathcal{R}$ allows us to test how a geodynamically predicted model of wavespeed variation $\mathbf{m}_{\text{in}}$ would be imaged tomographically, using the relationship

$$\mathbf{m}_{\text{out}} = \mathcal{R}\,\mathbf{m}_{\text{in}}, \tag{5.2}$$

where $\mathbf{m}_{\text{out}}$ is the tomographically 'filtered' version of the input model, which accounts for the effects of incomplete data coverage and inversion damping. We use $\mathcal{R}$ associated with S40RTS.

We project a 180° wide section of geodynamic simulations with the LLVPs into a 3D spherical model. The spherical model is symmetric about an axis through the center of the LLVP (Figure 5.2). The LLVP is not distorted significantly but structures far from the rotation axis are ring-like and cannot be interpreted.

Prior to filtering, we project the geodynamically predicted wave speed model into the parameterization of S40RTS. Lateral variations of δV_S are described using spherical harmonics up to degree and order 40, and depth variations by 21 vertical splines. Reparameterizing acts as a low pass filter and reduces the strength of the seismic anomaly (e.g., *Schuberth et al.*, 2009; *Maguire et al.*, 2017). Further details of the filtering process are found in *Ritsema et al.* (2007).

The resolution of S40RTS is inherently spatially heterogeneous so the effects of the filter $\mathcal{R}$ varies in the mantle. We evaluate how thermochemical plumes and piles are imaged beneath Africa and the Pacific by performing a solid-body rotation of the 3D δV_S model prior to filtering, such that the input model has plumes or piles centered in the regions where the LLVPs are imaged.

5.3 Results

5.3.1 Comparison between tomography and dynamic simulations

Figure 5.3 shows a comparison between the LLVPs observed in S40RTS and the tomographically filtered plumes or thermochemical piles placed beneath Africa (left column) and the Pacific (right column). In S40RTS, the LLVPs beneath Africa and the Pacific extend into the mid-mantle and are characterized by shear velocity reductions of about 2%. δV_S in the tomographically filtered models are similar in strength but the pattern of heterogeneity depends strongly on $\delta\rho_E$. When $\delta\rho_E = 4\%$ (i.e., when thermochemical piles do not form), the imaged plume structures have a strength that is half of the strength of the unfiltered anomaly. The filter weakens δV_S of the LLVP beneath Africa slightly more than a LLVP beneath the Pacific. The δV_S in the filtered plume structures are much smaller scale than δV_S in the LLVPs of S40RTS. When $\delta\rho_E \geq 6\%$ and thermochemical piles develop the filtered structures are more similar to LLVPs in S40RTS. When $\delta\rho_E = 6\%$, the piles have a similar width and amplitude as LLVPs in S40RTS, although they extend to only several hundred km above the CMB. When $\delta\rho_E = 8\%$ the imaged piles are broader and taller than piles for the $\delta\rho_E = 6\%$ case. The structure imaged beneath Africa in particular bears a strong resemblance to the African LLVP. It has a width of about 3000 km, a height of 1000 km, and shear velocity reductions of about 2.0%. When $\delta\rho_E = 10\%$, the piles are imaged with $\delta V_S \leq -2.0\%$ and extend well into the mid-mantle. The pile is weaker and more diffuse when imaged beneath Africa than when imaged beneath the Pacific. The structure surrounding the imaged piles is dominated by strong fast slab anomalies, which is inconsistent with tomographic observations. Overall, the dynamic simulations with $\delta\rho_E = 8\%$ develop structures that most closely match the observed LLVP structures beneath Africa and the Pacific, although the strength of the recovered anomaly is slightly larger than what is observed.

5.3.2 Resolving temperature and composition in thermochemical piles

We next investigate the range of temperatures and compositions in thermochemical piles that produce LLVPs with a δV_S consistent with tomographic observations. We systematically test how the filtered thermochemical piles depends on its volume and location on the CMB. Rather than using the dynamic simulations, we assume the thermochemical piles are elliptical domes with a length L, a height H, and seismic velocity anomaly δV_{IN} (see Figure 5.4). The largest LLVP we consider has $L = 2000$ km and $H = 1500$ km, which is similar in size to the largest pile structures that develop in the geodynamic simulations.

For simplicity we refer to the input model as δV_{IN} and the tomographically filtered model as δV_{OUT}. We estimate the percentage recovered of the input anomaly, which we call F. F is defined as the average of $\delta V_{\mathrm{IN}}/\delta V_{\mathrm{OUT}}$ within the pile (i.e., the region defined by H and L).

Figure 5.5 shows how F depends on H and L beneath Africa (Figure 5.5A) and the Pacific (Figure 5.5B). Over the range of sizes we consider, the structures are recovered with between 15% and 55% of their original amplitude, although the recovery depends on location. Structures recovered beneath the Pacific are between 1.1–2 times stronger than structures recovered beneath Africa. In general, the recovery is low when H and L are small, and improves systematically as L increases. The dependence of F on H is more complex. For structures beneath Africa, there is a local minimum in F for piles with $H = 800$ km, due to the poor resolution in S40RTS near a depth of 2100 km. When a large proportion of the structure sits in the region of poor resolution a smaller percentage is recovered. When H is greater than 800 km, F grows with increasing H since the resolution in S40RTS improves at shallower depths. A similar local minimum in resolution is present for structures beneath the Pacific when $H = 1000$ km.

In all cases, the strength of the anomaly δV_{IN} is reduced by at least 40% after tomographic filtering. This suggests that if LLVPs are similar in scale to the structures we test, their shear velocity reduction must be at least 4–5 % in order to match the reductions in V_S that are tomographically imaged. Figure 5.6 shows how shear velocity perturbation within a pile (i.e., δV_{IN}) depends on composition f and excess temperature ΔT at depths between 1900 – 2800 km. The seismic anomaly δV_{IN} is calculated relative to a mantle which has a fertile peridotite composition ($f = 0.125$), and a potential temperature of 1600 K. Throughout the lower mantle, the temperature anomaly ΔT is the dominant factor that determines the strength of the velocity anomaly. The green lines in each panel show the 5% slow velocity contour, which we estimate is the largest anomaly within a pile that would be consistent with tomographically observed LLVPs.

At 2800 km depth (Figure 5.6A), if excess temperature is low (below about $\Delta T = 400$ K) basalt enrichment within the pile reduces the seismic velocity. This is due to the post-perovskite phase transition in the reference profile, which is not as strong in eclogite. At higher temperatures ($\Delta T \geq 400$ K) the post-perovskite phase transition disappears. The presence of post-perovskite in the lowermost mantle means that if a pile is pure basalt (i.e., $f = 1.0$), the velocity will be reduced by almost 1% without zero temperature anomaly. However, after tomographic filtering, this anomaly would be imaged with $\delta V_S > -0.5\%$, which is much smaller than what we observe. Therefore, a model in which LLVPs are piles of recycled oceanic crust is not permissible, unless accompanied by an elevated temperature

of about 400 K or more. Furthermore, since shear velocity reductions are much more sensitive to temperature than to f throughout the lower mantle, the basalt fraction within LLVPs can not be determined from δV_S.

5.4 Discussion

The simulations of (*Brandenburg et al.*, 2008) which produce features most similar to LLVPs require the excess eclogite density to be $\delta\rho_E \geq 6\%$, which is larger than the $\sim 2\%$ excess density suggested by experimental and theoretical mineral physics results (e.g., *Tsuchiya*, 2011). It is difficult for piles to develop when $\delta\rho_E$ is small since recycled oceanic crust is entrained upwards in mantle plumes at a faster rate than it accumulates above the core (*Li and McNamara*, 2013). However, depending on viscosity contrasts in the lower mantle (*Christensen and Hofmann*, 1994), or the effective Rayleigh number (*Nakagawa and Tackley*, 2014) dense piles of oceanic material can develop for more realistic eclogite density contrasts. One limitation in our analysis is that the dynamic simulations are not self consistent with the mineral physics based modeling of seismic properties. Further dynamic simulations should use mineral physics based equations of state (e.g., *Nakagawa et al.*, 2010) which will allow self consistent calculation of mantle dynamics and seismic expression of dynamic features.

Our assumption of a mechanical mixture of basalt and harzburgite limits the range of compositions, and hence conceptual models of LLVP formation that we can explore. An alternative explanation for seismic observations of LLVPs is bulk iron enrichment, which could account for observations of increased density as well as anti-correlation between shear and bulk velocity anomalies (e.g., *Mao et al.*, 2011; *Deschamps et al.*, 2012, 2015). Future seismic modeling work which explores a wider range of bulk mantle composition, including equilibrium assemblages of MORB and harzburgite, as well as bulk iron enrichment is warranted.

The ratio R of $\delta V_S/\delta V_P$ within LLVPs is larger than what is expected for a pyolitic mantle, which has been used as evidence that LLVPs have a distinct composition. However, when comparing V_S and V_P anomalies, the difference in sensitivity of S and P phases must be considered. A tomographic filtering approach using the resolution matrix of joint S and P tomography models (e.g., *Koelemeijer et al.*, 2016) would allow us how to test the resolution of R within thermochemical piles.

5.5 Conclusions

We performed tomographic filtering tests of mantle mixing simulations and found that warm piles of recycled oceanic crust are largely consistent with LLVPs beneath Africa and the Pacific. Dynamic simulations assuming an excess eclogite density $\delta\rho_E \geq 6\%$ develop large (more than 2000 km wide and up to 1500 km tall) eclogite enriched piles with temperature anomalies as large as $\Delta T = 1000$ K. After tomographic filtering, these structures have similar scale and shear velocity reductions as tomographically observed LLVPs. We find that thermochemical piles are better resolved beneath the Pacific than Africa, but in either case the imaged structures are reduced in strength by a factor of about 2 or more. Hence, imaged of shear velocity reductions within LLVPs of more than 2% (Figure 5.1) likely represent anomalies of at least -4 to -5% near the CMB. Further, we find that eclogite enrichment alone can not explain tomographic observations of LLVPs. If LLVPs represent piles of recycled oceanic crust, they must be accompanied by a temperate elevated by at least 400 K (see Figure 5.6). Since shear velocity is much more sensitive to temperature than f throughout the lower mantle, the shear velocity reduction within LLVPs tells us little about their basalt content. Other compositional models for LLVPs, such bulk iron enrichment, can not be ruled out and should be the focus of future work.

5.6 Figures - Chapter 5

$\delta\rho_E$ (%)	4	6	8	10
Thermochemical piles?	no	yes	yes	yes
H (km)	–	300	600	1500
L (km)	–	3000	2000	1500

Table 5.1: Thermochemical pile characteristics.

Component	harzburgite	basalt
Na_2O	0.0	2.18
CaO	0.81	13.88
FeO	6.07	7.06
MgO	56.51	14.96
Al_2SiO_3	0.53	10.19
SiO_2	36.07	51.75

Table 5.2: Bulk composition of harzburgite (from Baker and Beckett (1999)) and mid-ocean ridge basalt (from Workman and Hart (2005)) given in terms of percent of six oxides.

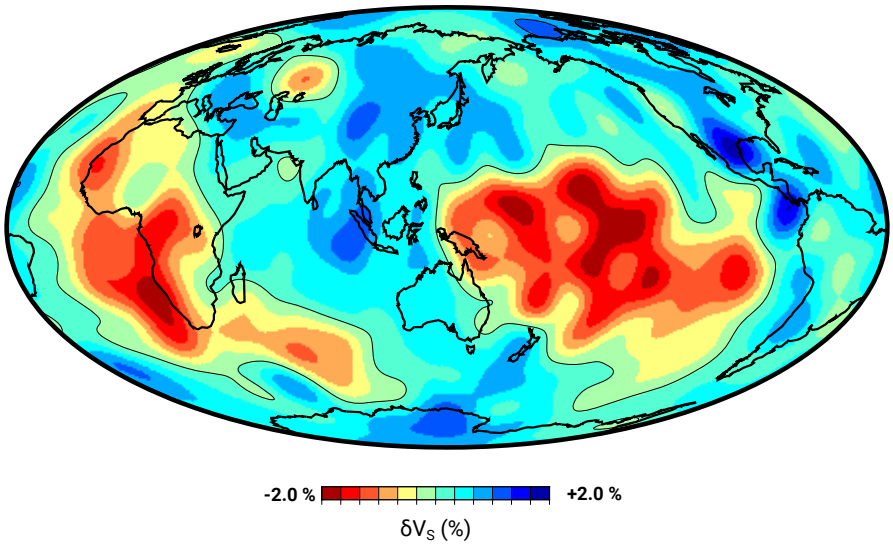

Figure 5.1: Map of the shear velocity anomaly at 2800 km depth in S40RTS, showing LLVPs beneath Africa and the Pacific Ocean. The edges of the LLVPs are marked by the $\delta \mathrm{V}_S = -1.0\%$ slow velocity contour.

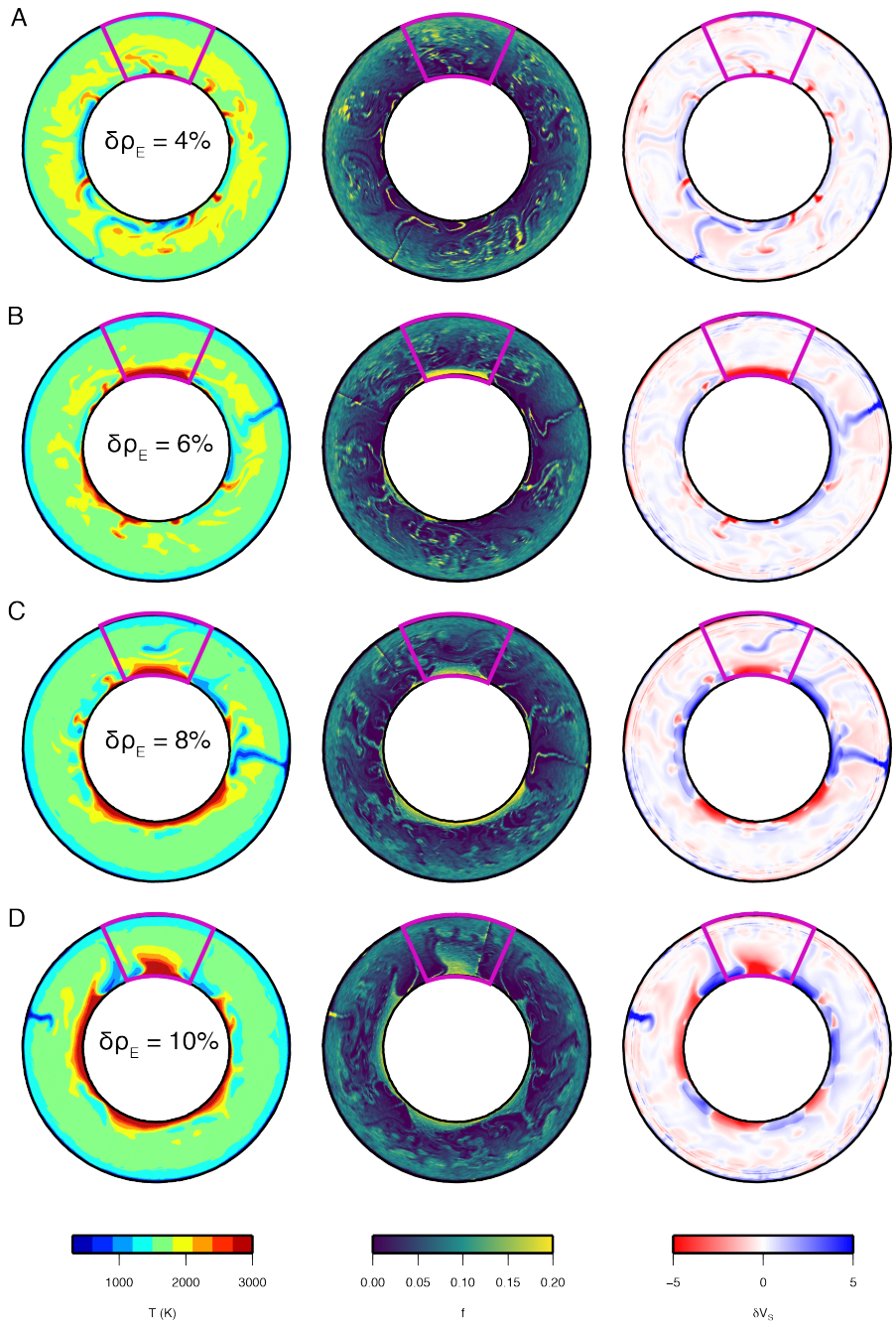

Figure 5.2: Snapshots of mantle convection simulations at 4.5 Gyr. Rows A–D correspond to simulations with $\delta\rho_E$ of 4%, 6%, 8%, and 10%, respectively. In each row, the left panel shows temperature, the middle panel shows f, and the right panel shows δV_S. Characteristic examples of plumes or thermochemical piles that develop in each simulation are outlined in pink.

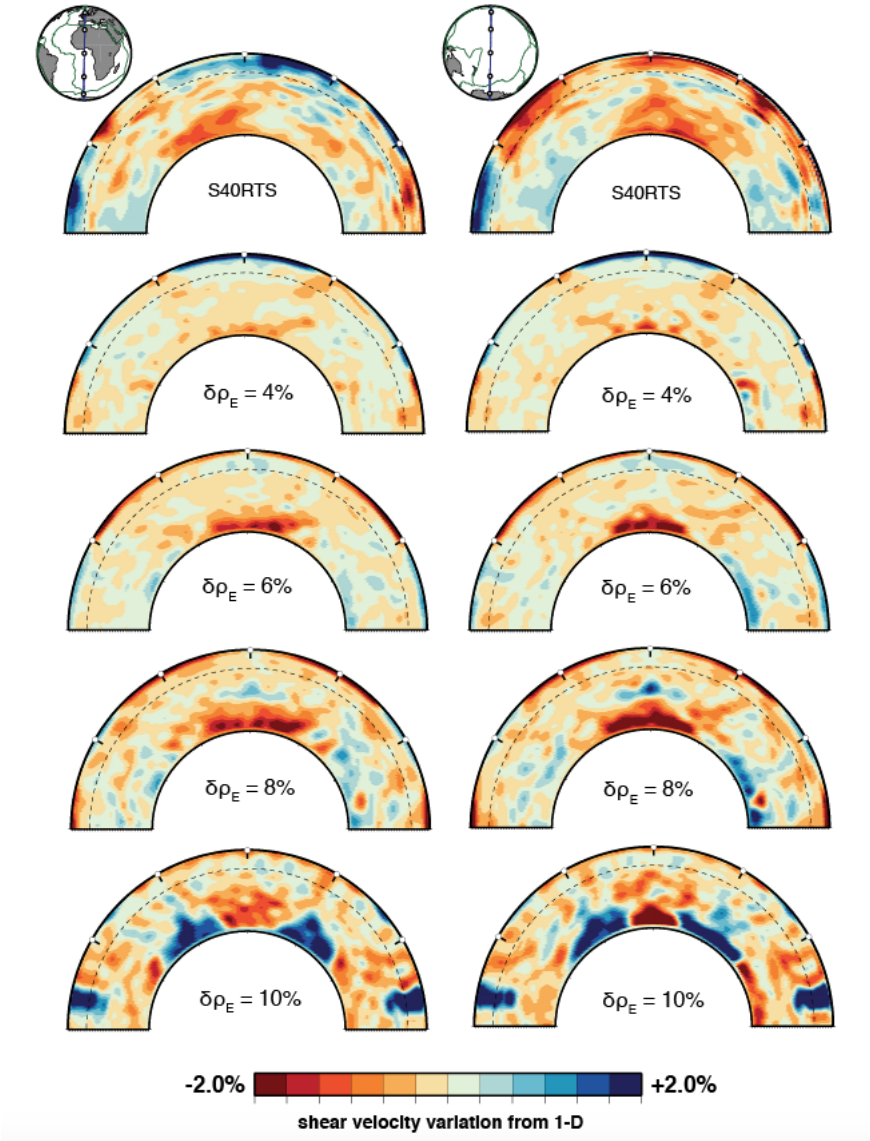

Figure 5.3: Comparison between LLVPs in S40RTS and tomographically filtered models. The left and right columns show results for the African and Pacific LLVPs, respectively.

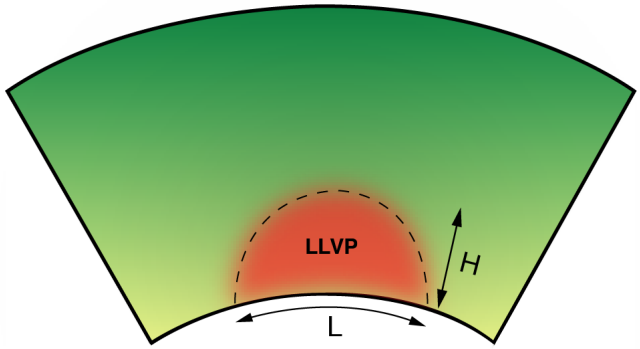

Figure 5.4: Diagram of LLVP input structures, which are elliptical domes defined by their width L at the CMB and their height H. Within the LLVP the shear velocity anomaly is defined as δV_{IN}, and outside the LLVP the shear velocity anomaly is 0.

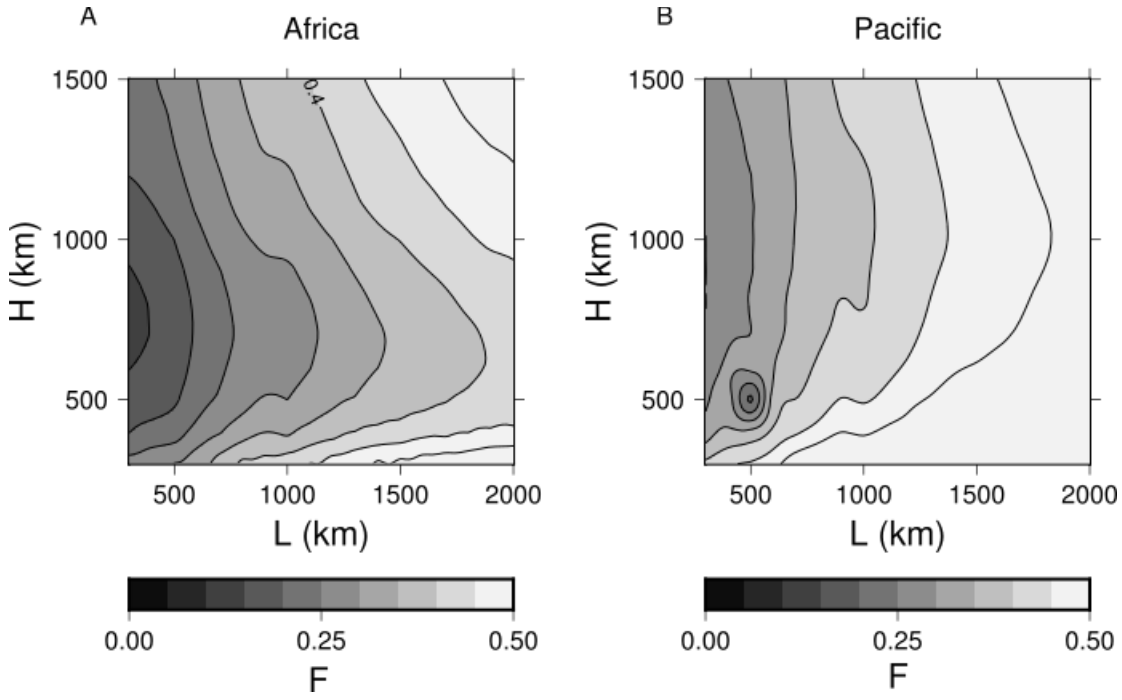

Figure 5.5: Recovery F of piles as a function of width L and height above the core-mantle boundary H, beneath Africa (A) and the Pacific (B).

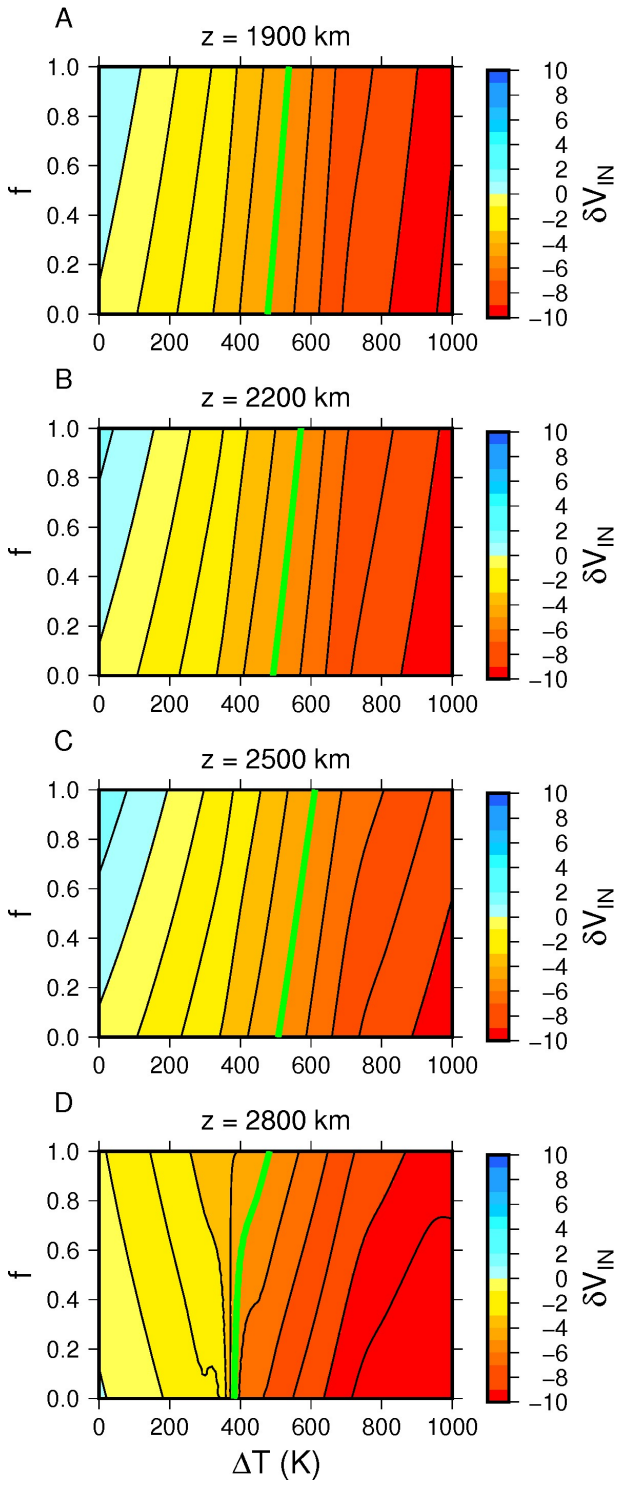

Figure 5.6: The strength of the seismic anomaly within an LLVP (δV_{IN}) in percent, as a function of ΔT and f, at depths of 1900 km (A), 2200 km (B), 2500 km (C), and 2800 km (D). The anomalies are computed relative to a mantle with a potential temperature of 1600 K, and a pyrolitic composition. In A–C (i.e., depths between 1900 km and 2500 km), seismic velocity is decreased by either elevating temperature or reducing f. At 2800 km depth increasing f reduces seismic velocity when $\Delta\mathrm{T} \leq 400$ K, while the opposite is true when $\Delta\mathrm{T} > 400$K. The green line indicates the 5% slow velocity contour.

CHAPTER 6

Evidence of subduction related thermal and compositional heterogeneity below the United States from transition-zone receiver functions

Abstract

The subduction of the Farallon Plate has altered the temperature and composition of the mantle transition zone (MTZ) beneath the United States. We investigate the structure of the MTZ by mapping P-to-S wave conversions at mineralogical phase changes using US-Array waveform data and theoretical seismic profiles based on experimental constraints on the depths and strengths of phase transitions as a function of temperature and composition. The width of the mantle transition zone varies by about 35 km over the study region, corresponding to temperature variation of more than 300 K. The MTZ is coldest and thickest beneath the eastern US where tomography model US-SL-2014 resolves high wavespeed anomalies. We detect intermittent P-to-S conversions at depths of 520 km and 730 km. The conversions at 730 km depth are coherent beneath the southeastern United States. This is consistent with basalt enrichment of about 50% in the uppermost lower mantle possibly due to the emplacement of a fragment of an oceanic plateau (i.e., the Hess conjugate) in the MTZ.

6.1 Introduction

The subduction of oceanic lithosphere brings thermal and compositional heterogeneity into the mantle transition zone (MTZ). The different chemical components of a slab, including sediments, crust, and the depleted mantle lithosphere separate due to transitions to denser mineral phases at different pressures. Over geologic time, mechanical mixing may produce

a compositional gradient across the MTZ since basaltic components accumulate preferentially above the 660-km phase transition and melt-depleted, harzburgitic components concentrate below it (e.g., *Irifune and Ringwood*, 1993; *Xie and Tackley*, 2004; *Nakagawa et al.*, 2010). Large fragments of recently subducted slabs may still be intact and distributed within the MTZ.

North America is an ideal region for studying the structure of the MTZ and its modification by plate subduction in the Cenozoic and Mesozoic. Tomographic images of the mantle beneath North America (e.g., *Grand*, 1994; *van der Lee and Nolet*, 1997; *Sigloch et al.*, 2008; *Sigloch*, 2012; *Porritt et al.*, 2014; *Schmandt and Lin*, 2014a; *Burdick et al.*, 2017) reveal high-velocity anomalies within or just below the MTZ beneath the central and eastern United States which may be relics of the Farallon oceanic plate. A phase of low-angle (i.e., flat-slab) subduction may explain the distribution of these slab remnants far from the ancient trench axis and the eastward propagation of deformation and arc-like magmatism during the Laramide orogeny (e.g., *Coney and Reynolds*, 1977; *Humphreys et al.*, 2003). *Livaccari et al.* (1981) suggested that the subduction of an oceanic plateau may provide the necessary buoyancy since the thickened oceanic crust and depleted harzburgite residue are less dense than the surrounding mantle. *Liu et al.* (2010) suggested that buoyancy forces from the conjugate halves of the Shatsky Rise and Hess Rise play a critical role in flat-slab subduction of the Farallon plate. They predicted that the subducted oceanic plateaus are presently located at the top of the lower mantle beneath the southeastern US (the Hess conjugate) and to the east of the Great Lakes region (the Shatsky conjugate). *Wang et al.* (2017) suggested that the eclogitized Hess conjugate caused Laramide age subsidence in the Gulf of Mexico region.

The deployment of the USArray over the past two decades has produced new seismic data for imaging the mantle with high spatial resolution. The USArray includes 120 Reference Network stations and about 400 Transportable Array stations with about 70-km station spacing. The TA stations were redeployed at sites in the western US and the eastern US between 2004 and 2013. Building on previous analyses (e.g., *Schmandt et al.*, 2012; *Tauzin et al.*, 2013; *Gao and Liu*, 2014), we develop receiver function images from USArray waveform data to map seismic discontinuities in the MTZ. Using mineral-physics relationships between temperature, composition, and wave speed, we associate the discontinuities with mineral phase transitions and estimate variations in temperature and composition from their relative depths and strengths. In particular, we investigate whether fragments of relatively cold slabs and relatively dense oceanic plateaus at the base of the MTZ, are evident in receiver functions to corroborate previous tomographic and geodynamic observations.

6.2 Receiver functions

6.2.1 Method

As is well documented (e.g., *Shearer*, 2000; *Deuss et al.*, 2013), phase transitions in the olivine system produce sharp gradients in seismic wavespeed observed near depths of 410-km, 520-km, and 660-km. Additional seismic discontinuities have been observed near the base of the transition zone between depths of about 660-km to 750-km (e.g., *Simmons and Gurrola*, 2000; *Deuss et al.*, 2006; *Wang and Niu*, 2011), which are commonly interpreted as phase transitions in the garnet system. Since garnet is a primary constituent in basaltic material at transition zone pressures, the detection of seismic signals produced just below 660-km depth may provide a useful estimate of the basalt content at the base of the MTZ.

In this study, we use the Pds receiver function method (e.g., *Vinnik*, 1977; *Burdick and Langston*, 1977; *Kind et al.*, 2012) image seismic velocity gradients in the MTZ. The Pds phase is a P-to-S wave conversion at depth d. Its amplitude and arrival time depends on the impedance contrast and depth of the seismic discontinuities or wave speed gradients associated with mineral phase transitions. We compute receiver functions by rotating the original seismograms into the RTZ coordinate system, filtering the waveforms with a band-pass filter between periods of 5–50 s, cutting waveform sections that begin 10 s before and end 120 s after the predicted P wave arrivals, and deconvolving the vertical from the radial component waveforms using the time-domain matrix inversion method (e.g, *Gurrola et al.*, 1995). The deconvolution is stabilized by using a damping parameter λ (we use $\lambda = 5$) to suppress noise without excessive low-pass filtering.

We analyze USArray recordings of all earthquakes which occurred between 2008–2014 and with moment magnitudes between 6 and 7 (Figure 6.1A). We include event-station pairs for epicentral distances between 30° and 90°. We cull receiver functions both visually and using the signal-to-noise criterion that the RMS amplitude of a 5-s window centered on the P onset must be at least 3 times larger than the RMS amplitude of a 20-s window (*Schmandt et al.*, 2012). After quality control, roughly half of the dataset has been rejected, retaining 46,026 high-quality receiver functions.

We migrate the receiver functions to depth using the common conversion point (CCP) technique (e.g., *Dueker and Sheehan*, 1997; *Eagar et al.*, 2010; *Schmandt et al.*, 2012; *Gao and Liu*, 2014). The imaging domain consists of voxels that are about 50×50 km^2 wide and 5 km thick. At a given depth, receiver function signals contribute to all points in the CCP volume which are within one Fresnel zone radius of the pierce point. We estimate and subtract the contributions of 3D velocity anomalies to the Pds and P traveltimes by ray tracing through the tomographic model US-SL-2014 (*Schmandt and Lin*, 2014a) using the

TauP method (*Crotwell et al.*, 1999).

The distribution of epicentral distances has a slight bias toward larger distances (Figure 6.1B) and the majority of the events were in South America and the western Pacific (Figure 6.1C). The imperfect illumination geometry hampers resolution of discontinuity topography and may introduce artifacts such as artificial duplexing of seismic interfaces (e.g., *Lekić and Fischer*, 2017). To test for artifacts due to illumination geometry, we apply all receiver function processing steps to synthetic seismograms for each of the events used in the study. We compute these synthetic waveforms up to frequencies of 0.2 Hz using the spectral element method waveform solver AxiSEM (*Nissen-Meyer et al.*, 2014), for source parameters documented in the Global CMT catalog (*Ekström et al.*, 2012), and the AK135 seismic reference model (*Montagner and Kennett*, 1996). The set of synthetic receiver functions has an identical ray parameter and back azimuth distribution as the observational data, and should be affected by deconvolution in a similar manner. Since AK135 includes only the 410 and 660 discontinuities we expect only P410s and P660s wave conversions to appear in our synthetic CCP images.

6.2.2 CCP cross sections

Figure 6.2 shows vertical cross sections through the CCP stacks along parallels at latitudes $44°$N (profile X), $38°$N (profile Y) and $32°$N (profile Z). The stacked receiver functions are superposed on the shear velocity structure of US-SL-2014 (*Schmandt and Lin*, 2014a). P-to-S conversions from the 410-km and 660-km discontinuities (i.e., $P410s$ and $P660s$) are the largest phases and coherent throughout the CCP image. Their amplitudes vary, but on average they are both about 5% of the direct P arrival. Along each cross section, the depths of the 410 and 660 varies by as much as +/- 20 km. Regions with the strongest deflections of the 410 and 660 correspond to strong wave speed anomalies in US-SL-2014. In general, regions with a positive wavespeed anomaly in the transition zone correspond to an anomalously shallow 410 and deep 660, while the opposite is true for regions with a negative wavespeed anomaly. Cross sections of the synthetic CCP images are shown in Figure 6.3. The amplitudes of P410s and P660s are relatively uniform across the imaging region, suggesting these discontinuities are well resolved in our study.

Signals of conversions from near the 520 (i.e., $P520s$) are detected intermittently in each of the three cross sections shown in Figure 6.2 (circled in green). In cross section X, a strong 520 between $-100°$ and $-110°$ has an amplitude as large as 30 % of $P410s$, and corresponds to a high velocity anomaly in US-SL2014. Weaker signals from 520 are present in cross section Y in low wave speed regions. In cross section Z, the 520 is apparent

in several locations but shows no clear association with wavespeed anomalies. There is an apparent doubling of the 520 near the western end of cross section Z, although synthetic tests show the transition zone is poorly resolved in this region (see Figure 6.3).

Cross section Z shows a strong signal from 730 is present between $-85°$ and $-95°$ (circled in pink). Here, the maximum amplitude of $P730s$ is about 30% of the amplitude of $P660s$. This signal coincides with a fast seismic wavespeed anomaly and a strong 520. Signals from 730 are also present in cross section Y in a region of anomalously high seismic wavespeed, but with no associated detection of the 520.

The stacked receiver functions show complicated signals between 250-km and 400-km depth, with single or double positive arrivals coherent across broad regions. However, signals in this depth range are also present in our synthetic CCP stacks (Figure 6.3), which are based on a seismic model with no velocity discontinuities in this depth range. It is likely that these signals are reverberations from shallower discontinuities. Sporadic and weak conversions are present between about 850-km and 1000-km depth. Seismic layering in the lower mantle have been observed previously (e.g., *Jenkins et al.*, 2017; *Waszek et al.*, 2018), but there are no known mineral phase transitions that could account for these observations.

6.2.3 Phasing diagrams

We verify that the observed Pds conversions from 520-km and 730-km depth have the expected slownesses by a phasing analysis of (e.g., *Fee and Dueker*, 2004) receiver functions from regions with the strongest signals. Figure 6.4 compares the stack of all 40,026 receiver functions (Figure 6.4A) to stacks of receiver functions that sample the northern Rockies (Figure 6.4B) and the southeastern US (Figure 6.4C). We estimate amplitude uncertainties by bootstrap resampling the receiver function stacks (*Efron and Tibshirani*, 1986).

The move-out corrected stack for the full data set (bottom left of Figure 6.4A) represents the average transition zone structure beneath the USArray. The $P410s$ and $P660s$ conversions at the 410 and 660 are the main signals and have the predicted P-to-S move-out. The $P520s$ and $P730s$ conversions are invisible, confirming that the 520 and 730 are not coherent boundaries beneath the USArray. The 520 is detected in the stacks of both subsets but the 730 is visible only in the stack from the southeastern United States (Figure 6.4C). Both the 520 and 730 signals are above noise level according to bootstrap re-sampling analysis. The phasing analysis diagrams (right panels of Figure 6.4B and C) confirm that the signals at 55 s after P (i.e., 9.8 s after $P410s$) and 73 s after P (i.e., 5.5 s after $P410s$) have slownesses and traveltimes consistent with $P520s$ and $P730s$.

The crust adds additional complication in interpreting receiver functions since reverber-

ations within the crust can masquerade as P-to-S conversions from deeper discontinuities. Crustal reverberations are expected to be strongest in regions with thick low velocity layers such as sedimentary basins. We test the influence of crustal reverberations by forward calculating receiver function stacks using AxiSEM for AK135 both with and without a crust. We use the crustal profile 'DN' from CRUST2.0 (*Laske et al.*, 2001), which characterizes the crustal structure over broad regions of the southeastern US near the Gulf of Mexico, where we detect a strong $P520s$ and $P730s$. The results, shown in Figure 6.5 indicate that the signals we observe following $P410s$ or $P660s$ are unlikely to be crustal reverberations. Our modeling shows reverberations are weak and arrive with the same delay time after $P410s$ and $P660s$. A CCP profile from the Gulf of Mexico region (Figure 6.5D) shows that $P520s$ arrives 9.8 s after $P410s$, while $P730s$ arrives 5.5 s after $P660s$.

6.3 Interpretation

6.3.1 Modeling T and C dependent velocity

We interpret our receiver function images of the transition zone using mineral physics modeling of the relationship between temperature, composition, and seismic wavespeed in the mantle. We compute the effects of temperature and composition on mineral phase equilibria and seismic velocities in the MTZ using the thermodynamic code Perple_X (*Connolly*, 2005) and the elastic parameter database of *Stixrude and Lithgow-Bertelloni* (2011). To account for the P and T dependent effects of anelasticity on seismic wavespeeds, we correct the anharmonic wavespeeds using the attenuation model Q7g (e.g., *Maguire et al.*, 2016). We consider the mantle to be a mechanical mixture of basalt (i.e., recycled oceanic crust) and harzburgite (i.e., the melt depleted fraction of oceanic lithosphere) (e.g., *Xu et al.*, 2008). We refer to the end member compositions basalt and harzburgite for simplicity but the actual mineral assemblages depend on thermodynamic conditions. The relative fractions of basalt and harzburgite are defined as f and $1-f$. We use the mid-ocean ridge basalt composition from *Workman and Hart* (2005) and harzburgite composition from *Baker and Beckett* (1999).

Figure 6.6A shows how the shear wave velocity V_S depends on the basalt fraction f in the mantle. Profiles of the P-wave velocity have a similar character. Each profile of V_S is computed along an adiabat with a potential temperature of 1573 K. There are seismic discontinuities or sharp gradients near 300 km, 410 km, 520 km, 660 km, and 730 km depth. For a pyrolitic (i.e., $f \approx 0.2$) or harzburgite-enriched mantle ($f < 0.2$), the 410, 520, and 660 in the olivine system are dominant. Both the 410 and 660 are narrower than

10 km and they are the largest discontinuities with shear velocity jumps of 7.8 % and 7.2 % respectively. The 300 and 520 are weaker and the 520 is spread over a broad depth interval.

As f increases, the 410, 520 and 660 phase changes in the olivine system weaken while the coesite to stishovite transformation near 300 km depth and the majorite garnet to bridgmanite transformation near 730 km depth become stronger. Low wave speeds throughout the transition zone also characterize a mantle enriched in basalt. The increase of V_S at the 730 is 1.8% for $f = 0.2$ and 11.2% for $f = 1$. The 730 is the only phase transition that occurs near the base of the transition zone in a purely basaltic mantle (when $f = 1$). Since the strength of the 660 and 730 depends strongly on f, we use the relative amplitudes of $P660s$ and $P730s$ to estimate the basalt fraction f. Figure 6.6B shows how the predicted receiver function $P730s/P660s$ amplitude ratio varies with basalt fraction f

Figure 6.6C shows how phase changes and V_S in the upper mantle depend on temperature. Here, we assume a homogeneous mantle composition with $f = 0.2$ (i.e., a roughly pyrolitic mantle). We vary the potential temperature of the adiabat between 1473 K and 1873 K, which is within -150 K to +250 K of the average potential temperature of mid-ocean-ridge basalt (MORB) suggested by *Herzberg et al.* (2007) Since the magnitude of the Clapeyron slope of the 660 transition is smaller than the 410 transition the phase boundary topography of the 660 is more subdued than the 410 for the same thermal anomaly. The transition zone thickness varies from 230 km to 280 km for our range of potential temperatures (Figure 6.6D).

The 730 is a strongly temperature-dependent exothermic transition. Its depth varies between about 730 km (for the 1473 K adiabat) to 800 km (for the 1873 K adiabat). However, $P730s$ is generally too weak in our data for it to be useful to map the temperature structure at the base of the MTZ.

6.3.2 Transition zone properties

Our estimates of the MTZ thickness and temperature inferred from our mineral physics models are shown in Figure 6.7A. The thickness of the transition zone is on average 249 km with peak-to-peak variations of about 35 km. This is in good agreement with the study by *Gao and Liu* (2014). The variation in thickness is similar to the velocity variations at 400 km depth imaged in US-SL-2014 (Figure 6.7D) and implies that the temperature in the MTZ beneath the United States varies by more than 300 K. Estimates of transition zone thickness and temperature change slightly depending on the seismic velocity model used to migrate receiver functions, but the general interpretations are robust. In Figure 6.8 we compare estimates of transition zone thickness based on a 1D seismic velocity model

to estimates using 3D tomography models US-SL-2014 (*Schmandt and Lin*, 2014a) and DNA13 (*Porritt et al.*, 2014).

The transition zone is thinnest and therefore warmest beneath the western United States, except for the Columbia Plateau region to the east of the Cascades. This likely reflects the cooling of the mantle by the Juan de Fuca slab which has penetrated into the MTZ although US-SL-2014 does not provide clear tomographic evidence for a high-velocity anomaly in the MTZ beneath this region. Yellowstone stands out as a small-scale region with an anomalously thin (230–240 km) transition zone, corresponding to a potential temperature of 1750–1850 K. It implies a deep origin of the Yellowstone hotspot, in agreement with *Schmandt et al.* (2012) but not with *Gao and Liu* (2014), who do not find evidence for a thin transition zone beneath Yellowstone. The transition zone is relatively thick (260–270 km) over broad regions beneath the central and southeastern United States with maxima that coincide with high-velocity anomalies in US-SL-2014. We infer the potential temperature in these regions to be between 1500–1600 K.

Figure 6.7B shows the regions where 520 discontinuity appears to be the strongest. The amplitude of $P520s$ is difficult to measure due to interference with the relatively strong side lobes of $P410s$ and $P660s$, which are artifacts of waveform deconvolution. Therefore we simply show in Figure 6.7B the regions where $P520s$ is at least 20% of $P410s$, which we consider to be robust detections. The 520 is strong in the MTZ beneath the Columbia Plateau and northern Basin and Range, where we also resolve the transition zone to be relatively thick and therefore cold. Further, we detect 520 coherently over a broad area beneath the northern Great Plains and Rocky Mountain region where wave speeds are relatively high according to US-SL-2104. However, we do not find evidence for a cool and thick transition zone in this region, which would be expected if slabs of subducted material are present. The 520 is also apparent in the southeastern United States near the Gulf of Mexico. Here, the thick transition zone and the high wave speeds provide complementary evidence for a cold downwelling.

Mineral physics models (Figure 6.6A) indicate that the impedance contrast at 520 increases with decreasing f. Therefore, Figure 6.7B may indicate regions of harzburgite enrichment. The absence of a pervasive detection of a 520 across the study area could indicate the MTZ is enriched in basalt on average. It is also possible that the intermittent detection of the 520 may signify a local sharpening of the seismic discontinuity, rather than an increased impedance contrast, which would increase the seismic visibility. Recently, *Mrosko et al.* (2015) found that the presence of water in transition zone under oxidizing environment reduces the stability field over which ringwoodite and wadsleyite coexist, and thus reducing the width of the 520 discontinuity. These conditions are expected in regions

of subduction, and thus may explain the association we observe between detections of the 520 and inferred downwellings, particularly in the southeastern United States. A hydrated transition zone beneath the Gulf of Mexico region has also been suggested by *Courtier and Revenaugh* (2013) who observe a strong 520 using multiple reverberations of ScS.

Figure 6.7C shows the variable basalt fraction f at the base of the MTZ inferred from amplitude ratios of $P730s$ and $P660s$. We assume that $f = 0$ in regions where $P730s$ is undetected, which may be inaccurate if $P730s$ is masked by side-lobes of adjacent arrivals, or if signals stack incoherently due to unmodeled 3D velocity structure. Additionally, regions with negative arrivals below 660, for example due to dehydration melting (e.g., *Schmandt et al.*, 2014b), would map as regions with $f = 0$. Nonetheless, Figure 6.7C reveals an intriguing pattern of the basalt content at the base of the transition zone.

The inferred basalt enrichment, with values $f > 0.3$, is highest in the southeastern US near the Gulf of Mexico. This coincides with a region of thick transition zone, and a detection of the 520. Additionally, US-SL-2014 maps a high velocity anomaly at the top of the lower mantle in this region (Figure 6.7E). A similarly enriched mantle is found along the Atlantic coast to the east of the Appalachians with no concurrent detection of the 520. Small regions of enriched mantle are also found to the east of the Great Lakes region and near Lake Superior. The western US is largely depleted with the exception of the Colorado Plateau region, with $f \approx 0.2$, and an east-west trending region north of Rockies with $f \approx 0.3$. The Northern Rockies region is also associated with a strong 520.

6.4 Discussion

In a pyrolitic mantle, the 520 and 730 should produce observable $P520s$ and $P730s$ wave conversions, yet these signals are recorded intermittently. The low amplitudes of $P520s$ and $P730s$ may indicate a strongly compositionally layered mantle with basalt enrichment and depletion above and below the 660 (e.g., *Nakagawa et al.*, 2010). The 520 and 730 are weak or even absent in such a mantle (see Figure 6.6A). Our stack of the full set of receiver functions from all stations of the USArray is consistent with the geodynamic predictions of a compositional gradient in the MTZ beneath North America.

The local detections of $P520s$ and $P730s$ may indicate regions of the MTZ where a compositional gradient has been perturbed by vertical flow, either by sinking slabs or the ascent of plumes. In general, there is no clear correlation between the strength of the 520 and 730 discontinuities and the inferred MTZ temperature, although some trends are apparent.

1. The detection of the 520 typically coincides with high-velocity anomalies in US-SL-

2014 within the MTZ, with a thick transition zone, or both.

2. The MTZ is coolest and the basalt enrichment is highest beneath the eastern US

3. Basalt enrichment in the Gulf of Mexico region correlates with a high-velocity anomaly, a detection of the 520, and a thick transition zone.

These results are consistent with a mantle that has been perturbed by recent subduction and with the widespread distribution of fragments of cold slabs in the MTZ beneath the eastern US. Previous studies have interpreted the high-velocity anomalies in the MTZ as remnants of the Farallon slab, which subducted eastward from the western margin of the US during the Mesozoic and Cenozoic (e.g., *Bunge and Grand*, 2000), although other subduction histories remain possible (e.g., *Sigloch and Mihalynuk*, 2013).

Geodynamic simulations by *Liu et al.* (2010) suggest that buoyancy forces from the conjugate halves of the Shatsky Rise and Hess Rise play a critical role in flat slab subduction of the Farallon plate. Furthermore, they predicted that the subducted oceanic plateaus are presently located at the top of the lower mantle beneath the southeastern United States (the Hess conjugate) and to the east of the Great Lakes (the Shatsky conjugate). *Wang et al.* (2017) suggested that the negative buoyancy from the eclogitized Hess conjugate explains Laramide age subsidence in the Gulf of Mexico region. The presence of a subducted oceanic plateau (i.e., the Hess conjugate) may explain the strong signature of basalt enrichment that we observe beneath the southeastern US.

6.5 Conclusions

CCP images (Figure 6.2 and 6.7) of receiver functions from seven years of USArray waveform data indicate the variable strength of phase transitions in the transition zone. This is compatible with a mantle with basalt enrichment in the MTZ above the 660 and harzburgite enrichment in the mantle below the 660. The images, with a lateral resolution of about 100 km, indicate that the 410 and 660 transitions are the only coherent boundaries. The width between the 410 and 660 varies by about 35 km, consistent with temperature variations of 300 K. The lateral variations of the transition zone thickness correlate with the wave speed variation resolved by tomography. The transition zone is relatively thick and cool beneath the eastern United States, due to the presence of fragments of the subducted Farallon slab.

The receiver functions include a strong P-wave to S-wave conversion from a depth of about 730 km beneath the Gulf of Mexico region which is consistent with the garnet to bridgmanite phase transition within a relatively cold (1500 – 1600 $^\circ$ K) slab fragment. The

location of the reflector at 730-km depth correlates with the location of the subducted Hess conjugate predicted by geodynamic simulations (*Liu et al.*, 2010). Our results demonstrate the potential of using the regional variability of the transition zone structure below 660-km depth to map compositional heterogeneity at the base of the transition zone.

6.6 Figures - Chapter 6

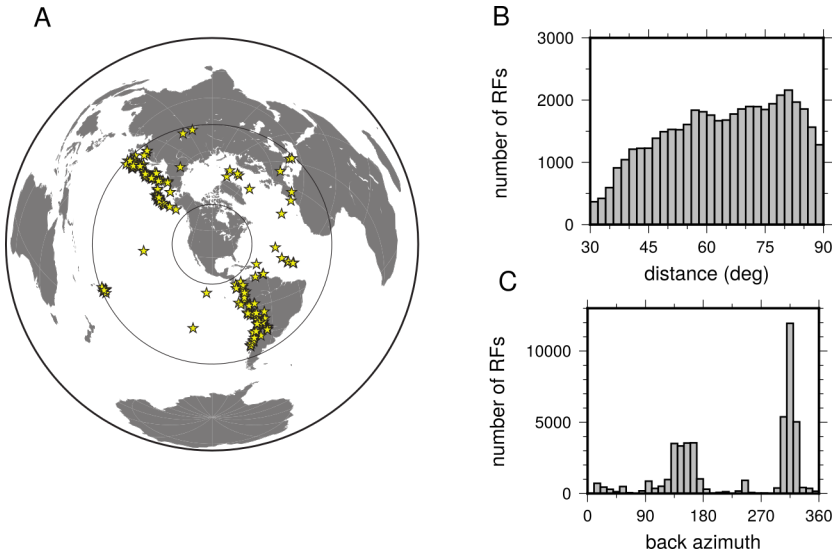

Figure 6.1: (A) Map of events used in this study. The distribution of epicentral distances is shown in (B) and the distribution of back azimuths is shown in (C).

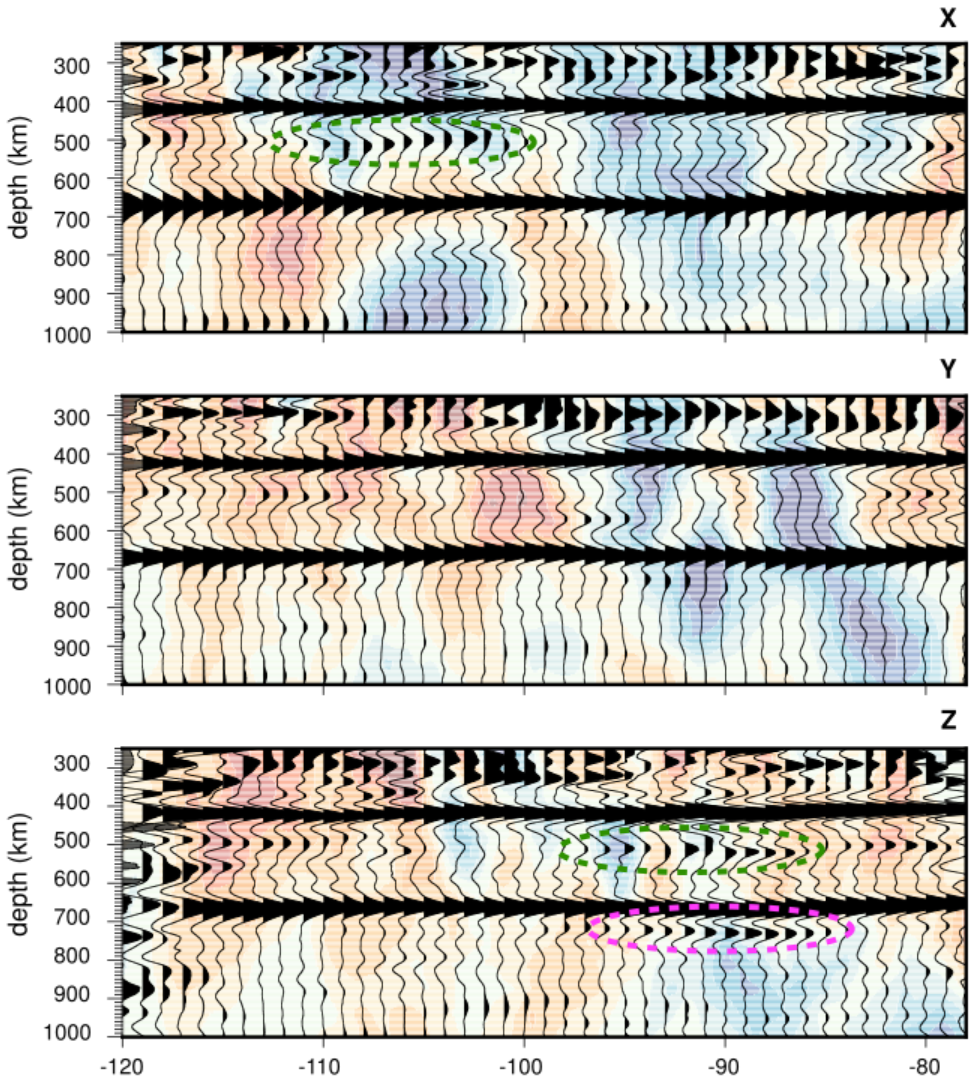

Figure 6.2: Longitudinal cross sections through the CCP imaging volume for (from top to bottom) latitude 44°N (profile X), 38°N (profile Y), and 32°N (profile Z). High-amplitude conversions from the 520 and 730 are indicated by green and pink circles, respectively. The background depicts the shear velocity structure of tomographic model US-SL-2014. The locations of the cross sections are shown in Figure 6.7D.

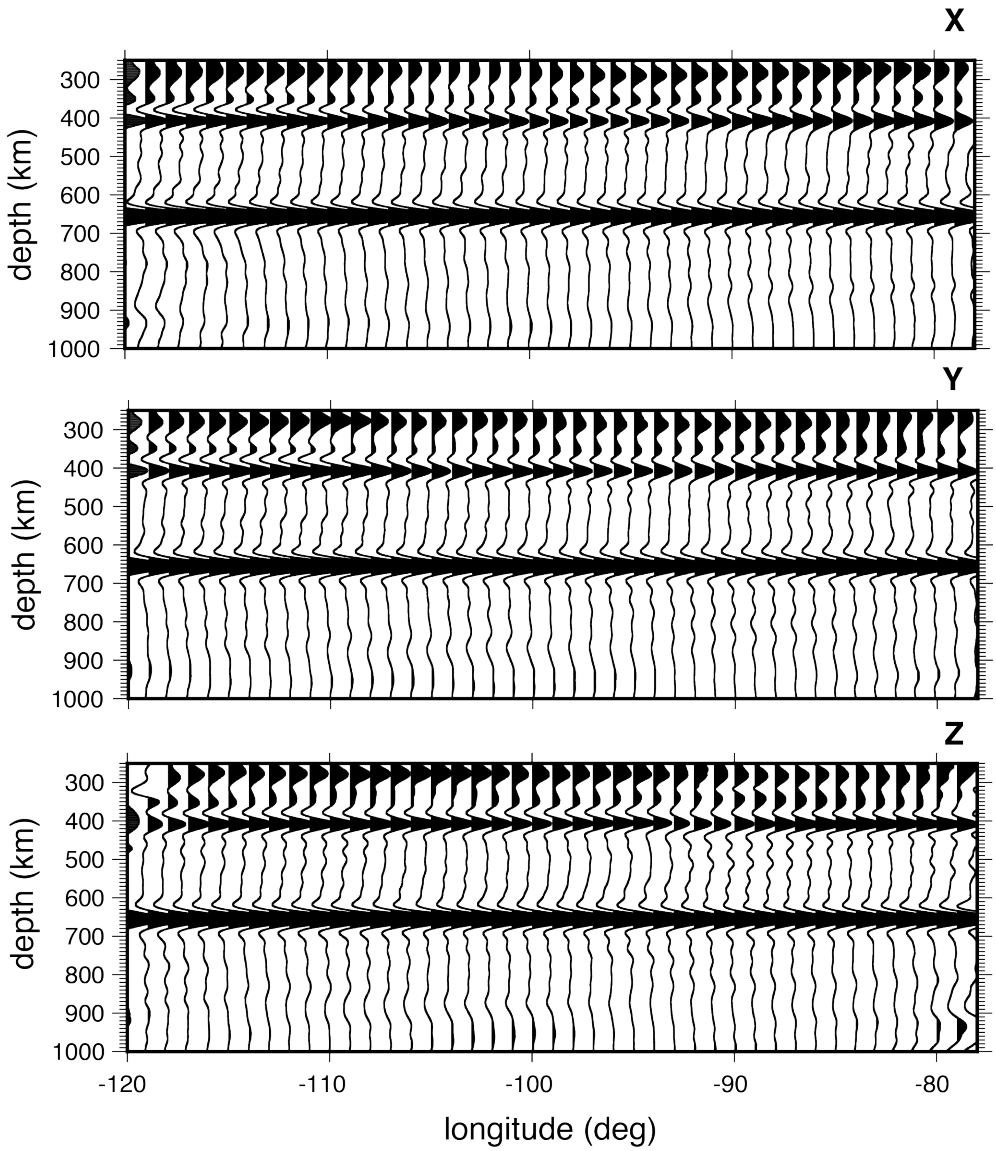

Figure 6.3: Cross sections through synthetic CCP image at latitudes of 44° (cross section X), 38° (cross section Y), and 32° (cross section Z).

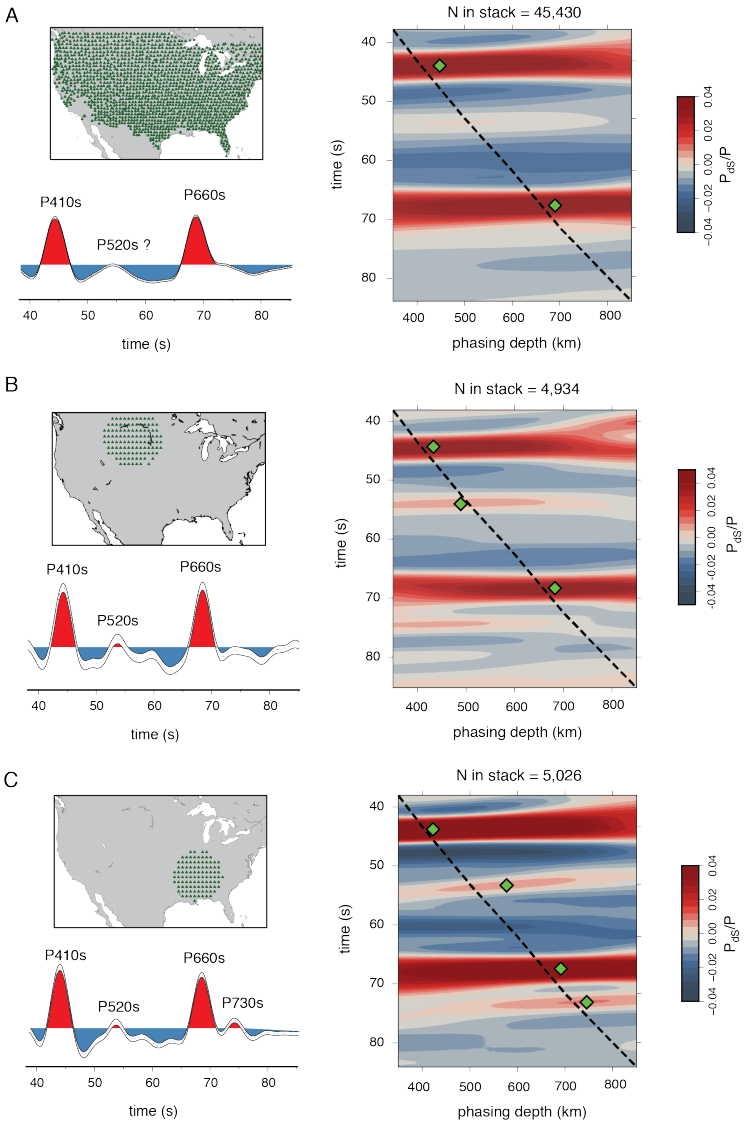

Figure 6.4: Comparison between receiver function stacks of the full data set (A), and regional stacks of 4,934 receiver functions from stations in the northern Rockies (B), and 5,026 receiver functions from stations in the southeastern US (C). Each region has three panels. The top left panel shows the included stations, the bottom left panel shows the move-out corrected stack, and the right panel shows a phasing analysis. The move-out corrected stacks show the average receiver function signal, as well as the upper and lower bound of the bootstrap confidence interval. Positively identified phases are labeled. Green diamonds shown in the phasing analysis indicate a local maximum.

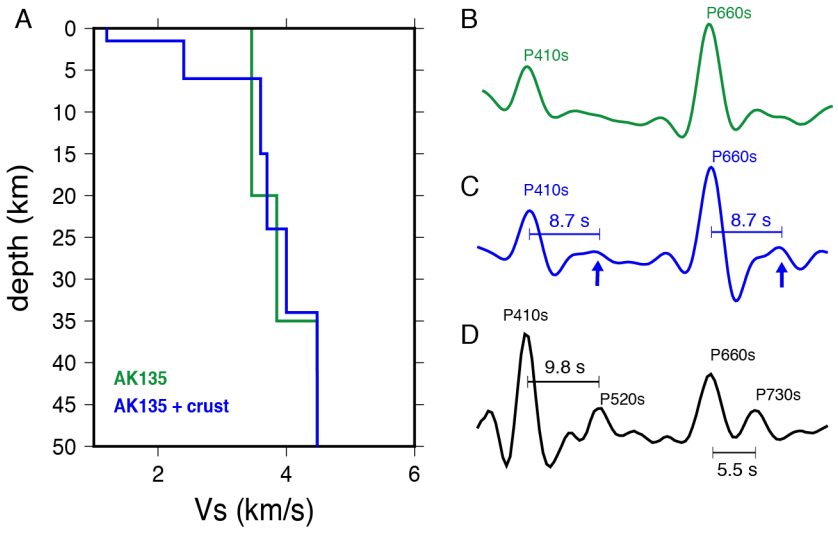

Figure 6.5: Crustal reverberation modeling. A shows the V_S structures of AK135 (in green) and AK135 with a crustal profile DN from CRUST2.0 added (in blue). B and C show synthetic receiver function stacks computed for each profile. In C, weak positive arrivals about 8.7 s after both P410s and P660s (marked with arrows) are crustal reverberations. D shows a vertical profile of the CCP image in the southeast US, near the Gulf of Mexico (a location characterized by DN in CRUST2.0).

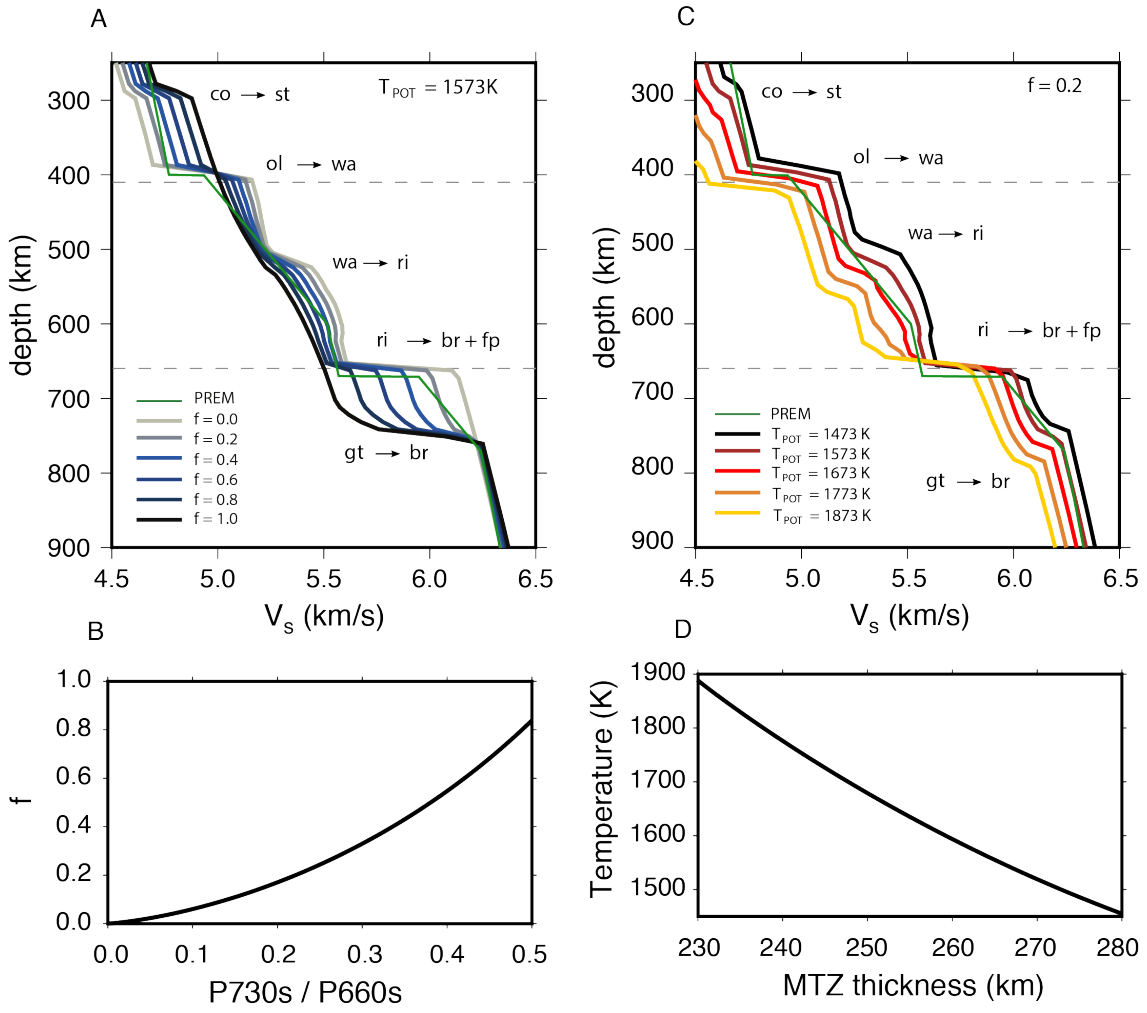

Figure 6.6: (A) Profiles of the shear velocity (V_S) for mechanical mixtures with varying basalt fraction f. Each of the profiles is calculated along an adiabat with a potential temperature of 1573 K. The green line is the V_S profile for PREM. (B) Amplitude ratios of $P730s/P660s$ calculated using the profiles in A. (C) V_S profiles of a pyrolitic composition (i.e., $f = 0.2$) calculated for different adiabats. (D) MTZ thickness as a function of temperature, calculated from the profiles in C. Mineral phase names in A and C are as follows: coesite (co), stishovite (st), olivine (ol), wadsleyite (wa), ringwoodite (ri), brigmanite (br), ferropericlase (fp), majorite garnet (gt). The 300, 410, 520, 660, and 730 correspond to the $co \rightarrow st$, $ol \rightarrow wa$, $wa \rightarrow ri$, $ri \rightarrow br + fp$, and $gt \rightarrow br$ mineral transitions, respectively.

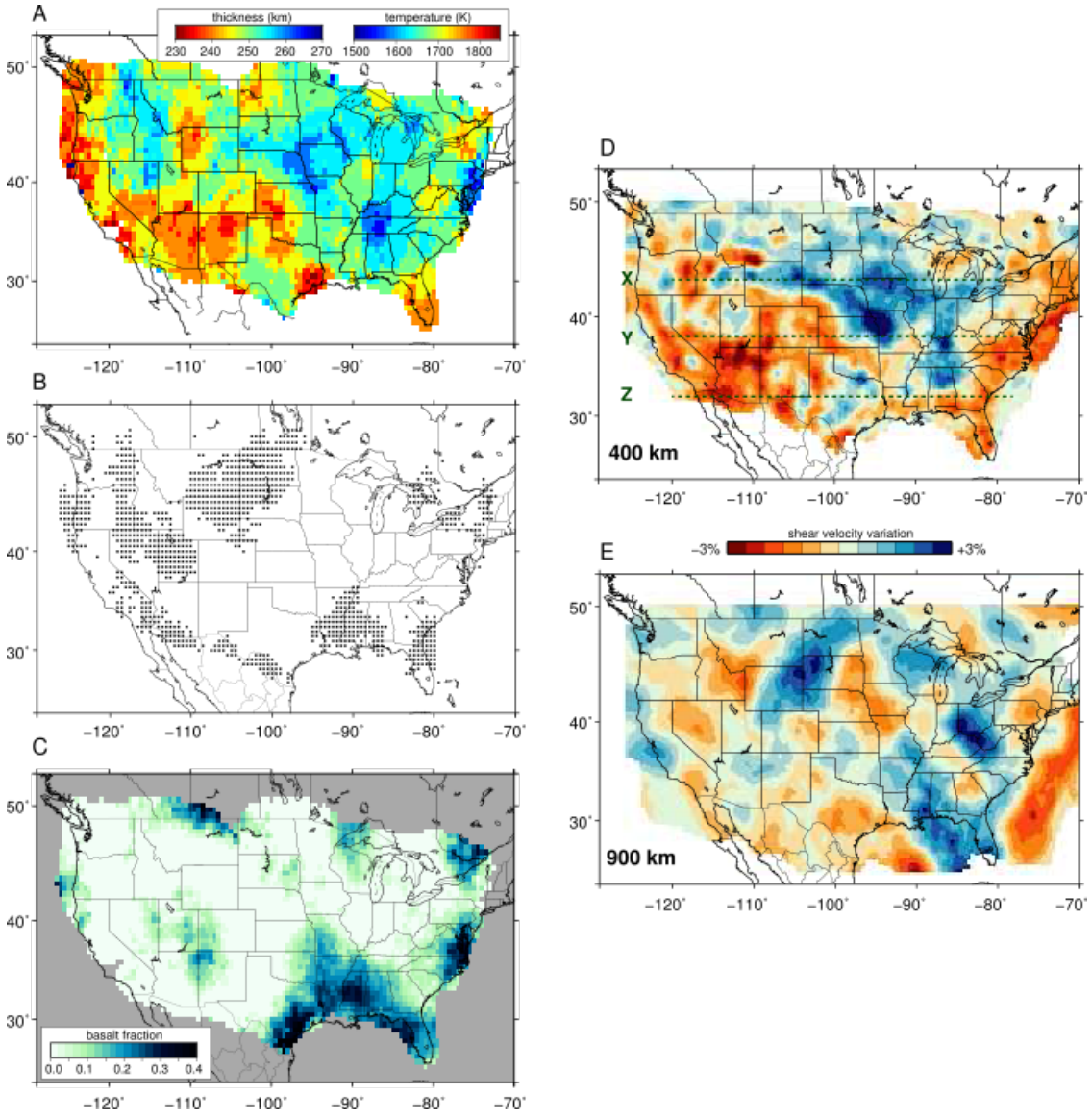

Figure 6.7: The maps on the left show (A) the thickness of the transition zone estimated from $P660s$ - $P410s$ arrival times and the potential temperature as inferred from predicted seismic velocity profiles of MM pyrolite, (B) regions where $P520s$ is detected with an amplitude of at least 20% of $P410s$, and (C) the inferred basalt fraction based on the $P730s$ / $P660s$ amplitude ratio. The maps on the right show shear velocity variations at depths of 400 km (D) and 900 km (E) according to model US-SL-2014. The dashed lines in D indicate the transects X, Y, and Z of the CCP cross sections shown in Figure 6.2.

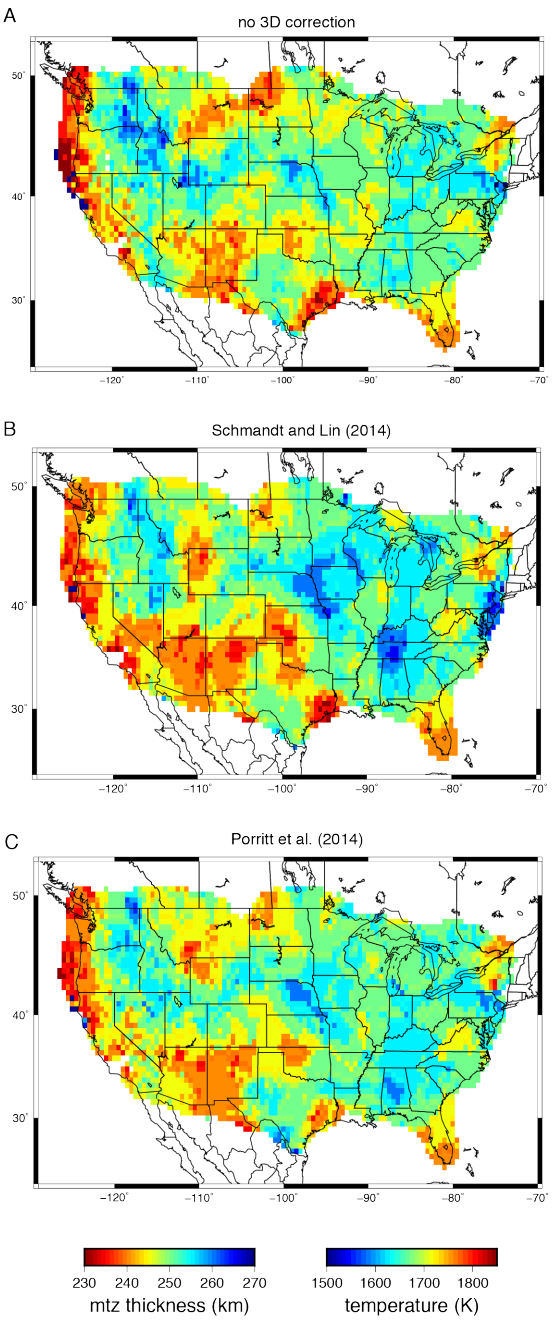

Figure 6.8: Comparison of mantle transition zone thickness maps created assuming different mantle velocity structures. Map A uses AK135 to migrate receiver functions to depth. Maps B and C use 3D tomography models US-SL2014 (Schmandt and Lin, 2014), and DNA13 (Porritt et al., 2014), respectively.

CHAPTER 7

Conclusions

The work presented here demonstrates how experimental and theoretical mineral physics, seismic imaging, and physics-based modeling of mantle flow can be used together to gain insight into the variations of temperature, composition, and mineralogy of Earth's mantle. I focused on using this combined approach to assess the limitations of seismic tomography to resolve small scale heterogeneity, and tested how thermal and compositional mantle models are compatible with seismic observations.

In Chapters 2 and 3, I investigated how thermal plumes rising from the core-mantle boundary affect seismic waves, and how traveltime tomography can constrain their role in mantle convection. I calculated the temperature structure of plumes using a physics-based model of plume formation and ascent, and determined how hot plumes in the deep mantle affect the elastic properties of rock and how much plumes will slow down through going seismic waves. The modeling shows that the plumes may slow down a wave by less than 1 second, which suggests that imaging plume tails is more challenging than is generally recognized. Such small delays are in principle observable but we must understand in detail how other other structures in the mantle could affect the propagation of seismic waves. For example, variations in the thickness of the crust or heterogeneous structures within the lithosphere (i.e. tectonic plates) may also slow down or speed up waves. I also investigated how new networks of seismometers can improve the resolution of small structures, such as relatively narrow plumes, in the deep mantle. I focused on the resolution of a plume beneath Hawaii because it is the textbook example of a group of volcanic islands formed by hotspot volcanism. I find that to most accurately recover structure in the deep mantle, it is necessary to place seismometers on the seafloor far from the Hawaiian islands. Such offshore deployments are extremely expensive and logistically challenging. This work can help set the requirements for future imaging experiments since I investigated optimal imaging scenarios that can recover the most detail at the lowest cost (i.e., fewest seismometers).

I further investigated mantle plume imaging in Chapter 4 by analyzing global tomography images of the mantle beneath the Samoa hotspot. Low seismic wavespeeds, indicative

of an anomalously warm mantle, are observed beneath Samoa nearly continuously from the core-mantle boundary to the surface, with the exception of a narrow region of high wavespeeds below the transition zone. This disruption, referred to as the 'Samoa gap' may imply a break in mantle flow across the 660-km discontinuity. I tested various thermal and petrological models and found that due to competing effects of temperature and composition on seismic wavespeed, the Samoa gap, can be explained by a combination of an elevated 660-km discontinuity and harzburgite enrichment within a hot mantle. The compositionally layered model is consistent with geoydnamic predictions of the segregation of harzburgite and eclogite within plumes at transition zone depths. These results demonstrate that complex patterns of heterogeneity typically observed near 660-km depth in global tomography should not necessarily be interpreted in terms of discontinuous flow structures.

In Chapter 5 I explored the origin of the LLVPs beneath Africa and the Pacific, which are thought to be anomalously warm and compositionally distinct mantle domains, and which could be source regions for mantle plumes. I found that the tomographically observed shear velocity reductions in LLVPs are broadly consistent with piles of recycled oceanic crust that has accumulated at the core. The LLVPs require a temperature anomaly of at least 400 K to match tomography. However, I also found that we are unable to uniquely determine the basalt fraction within piles, and the other compositional models could be permissible.

In Chapter 6 I linked seismic observations of transition zone discontinuities beneath the United States to constraints from mineral physics. I modeled the transition zone as a mechanical mixture of recycled mid-ocean ridge basalt and depleted harzburgite, and made estimates of transition zone composition and thermal structure. My primary results show that the transition zone structure beneath beneath the eastern US is consistent with modification by the recent subduction of the Farallon slab. I found evidence of basalt enrichment at the base of the transition zone in a region where geodynamic modeling has predicted the presence of a subducted oceanic plateau.

Much of the work presented here relies heavily of high-performance computing. Only in recent years, as computational resources have grown, have accurate 3D numerical simulations of wave propagation in realistic Earth models been possible. In the seismic analysis of mantle plume tails, I was limited to modeling seismic waves with a minimum period of 10 s, even with advanced supercomputing resources, while teleseismic traveltime observations can typically be made at frequencies up to 1 Hz. As high-performance computer systems continue to improve, and numerical tools become more efficient, 3D wave propagation simulations encompassing the entire broadband frequency range of teleseismic observations will become routine. These future advances will enable investigation of more

complex Earth models and reveal further aspects of how dynamic structures affect seismic waves.

BIBLIOGRAPHY

Albers, M., and U. R. Christensen (1996), The excess temperature of plumes rising from the core-mantle boundary, *Geophysical Research Letters*, *23*(24), 3567–3570.

Allen, R. M., G. Nolet, W. J. Morgan, K. Vogfjórd, B. H. Bergsson, P. Erlendsson, G. R. Foulger, S. Jakobsdóttir, B. R. Julian, M. Pritchard, S. Ragnarsson, and R. Stefánsson (1999), The thin hot plume beneath Iceland, *Geophysical Journal International*, *137*, 51–63, doi:10.1046/j.1365-246x.1999.00753.x.

Allen, R. M., G. Nolet, W. J. Morgan, K. Vogfjord, B. H. Bergsson, P. Erlendsson, G. R. Foulger, S. Jakobsdottir, B. R. Julian, M. Pritchard, S. Ragnarsson, and R. Stefansson (2002), Imaging the mantle beneath Iceland using integrated seismological techniques, *Journal of Geophysical Research*, *107*(B12), 1–16, doi:10.1029/2001JB000595.

Baker, M. B., and J. R. Beckett (1999), The origin of abyssal peridotites: A reinterpretation of constraints based on primary bulk compositions, *Earth and Planetary Science Letters*, *171*(1), 49–61, doi:10.1016/S0012-821X(99)00130-2.

Ballmer, M., P. E. van Keken, and G. Ito (2015), Hotspots, large igneous provinces, and melting anomalies, in *Treatise on Geophysics*, edited by G. Schubert, 2nd ed., pp. 393 – 459, Elsevier, Oxford, England, doi:https://doi.org/10.1016/B978-0-444-53802-4.00133-0.

Ballmer, M. D., G. Ito, C. J. Wolfe, and S. C. Solomon (2013), Double layering of a thermochemical plume in the upper mantle beneath Hawaii, *Earth and Planetary Science Letters*, *376*, 155–164, doi:10.1016/j.epsl.2013.06.022.

Bijwaard, H., and W. Spakman (1999), Tomographic evidence for a narrow whole mantle plume below Iceland, *Earth and Planetary Science Letters*, *166*(3-4), 121–126, doi:10.1016/S0012-821X(99)00004-7.

Bonnin, M., G. Nolet, A. Villaseñor, J. Gallart, and C. Thomas (2014), Multiple-frequency tomography of the upper mantle beneath the African/Iberian collision zone, *Geophysical Journal International*, *198*, 1458–1473, doi:10.1093/gji/ggu214.

Boschi, L., T. W. Becker, and B. Steinberger (2007), Mantle plumes: Dynamic models and seismic images, *Geochemistry, Geophysics, Geosystems*, *8*(10), 1–20, doi:10.1029/2007GC001733.

Boschi, L., T. W. Becker, and B. Steinberger (2008), On the statistical significance of correlations between synthetic mantle plumes and tomographic models, *Physics of the Earth and Planetary Interiors*, *8*(10), 230–238, doi:10.1029/2007GC001733.

Bossmann, A. B., and P. E. van Keken (2013), Dynamics of plumes in a compressible mantle with phase changes: Implications for phase boundary topography, *Physics of the Earth and Planetary Interiors*, *224*, 21–31, doi:10.1016/j.pepi.2013.09.002.

Bozdağ, E., J. Trampert, and J. Tromp (2011), Misfit functions for full waveform inversion based on instantaneous phase and envelope measurements, *Geophysical Journal International*, *185*(2), 845–870, doi:10.1111/j.1365-246X.2011.04970.x.

Bozdağ, E., D. Peter, M. Lefebvre, D. Komatitsch, J. Tromp, J. Hill, N. Podhorszki, and D. Pugmire (2016), Global adjoint tomography: First-generation model, *Geophysical Journal International*, *207*(3), 1739–1766, doi:10.1093/gji/ggw356.

Brandenburg, J. P., and P. E. van Keken (2007), Deep storage of oceanic crust in a vigorously convecting mantle, *Journal of Geophysical Research: Solid Earth*, *112*(6), 1–15, doi:10.1029/2006JB004813.

Brandenburg, J. P., E. H. Hauri, P. E. van Keken, and C. J. Ballentine (2008), A multiple-system study of the geochemical evolution of the mantle with force-balanced plates and thermochemical effects, *Earth and Planetary Science Letters*, *276*(1-2), 1–13, doi:10.1016/j.epsl.2008.08.027.

Bull, A. L., A. K. McNamara, and J. Ritsema (2009), Synthetic tomography of plume clusters and thermochemical piles, *Earth and Planetary Science Letters*, *278*(3-4), 152–162, doi:10.1016/j.epsl.2008.11.018.

Bunge, H.-P., and S. P. Grand (2000), Mesozoic plate-motion history below the northeast pacific ocean from seismic images of the subducted farallon slab, *Nature*, *405*(6784), 337.

Burdick, L. J., and C. a. Langston (1977), Modeling crustal structure through the use of converted phases in teleseismic body-wave forms, *Bulletin of the Seismological Society of America*, *67*(3), 677–691.

Burdick, S., F. L. Vernon, V. Martynov, J. Eakins, T. Cox, J. Tytell, T. Mulder, M. C. White, L. Astiz, G. L. Pavlis, and R. D. van der Hilst (2017), Model update May 2016: upper–mantle heterogeneity beneath North America from travel–time tomography with global and USArray data, *Seismological Research Letters*, *88*, 319–325, doi:10.1785/0220160186.

Cammarano, F., S. Goes, P. Vacher, and D. Giardini (2003), Inferring upper-mantle temperatures from seismic velocities, *Physics of the Earth and Planetary Interiors*, *138*(3-4), 197–222, doi:10.1016/S0031-9201(03)00156-0.

Charléty, J., S. Voronin, G. Nolet, I. Loris, F. J. Simons, K. Sigloch, and I. C. Daubechies (2013), Global seismic tomography with sparsity constraints: Comparison with smoothing and damping regularization, *Journal of Geophysical Research: Solid Earth*, *118*(9), 4887–4899, doi:10.1002/jgrb.50326.

Chevrot, S., R. Martin, and D. Komatitsch (2012), Optimized discrete wavelet transforms in the cubed sphere with the lifting scheme-implications for global finite-frequency tomography, *Geophysical Journal International*, *191*(3), 1391–1402, doi:10.1111/j.1365-246X.2012.05686.x.

Christensen, U. R., and A. W. Hofmann (1994), Segregation of subducted oceanic crust in the convecting mantle, *Journal of Geophysical Research: Solid Earth*, *99*(B10), 19,867–19,884.

Cobden, L., S. Goes, F. Cammarano, and J. a. D. Connolly (2008), Thermochemical interpretation of one-dimensional seismic reference models for the upper mantle: Evidence for bias due to heterogeneity, *Geophysical Journal International*, *175*(2), 627–648, doi:10.1111/j.1365-246X.2008.03903.x.

Coney, P. J., and S. J. Reynolds (1977), Cordilleran Benioff Zones, *Nature*, *270*, 403–406, doi:10.1038/275464a0.

Connolly, J. a. D. (2005), Computation of phase equilibria by linear programming: A tool for geodynamic modeling and its application to subduction zone decarbonation, *Earth and Planetary Science Letters*, *236*(1-2), 524–541, doi:10.1016/j.epsl.2005.04.033.

Courtier, A. M., and J. Revenaugh (2013), A Water-Rich Transition Zone Beneath the Eastern United States and Gulf of Mexico from Multiple ScS Reverberations, in *Earth's Deep Water Cycle*, pp. 181–193, doi:10.1029/168GM14.

Courtier, A. M., M. G. Jackson, J. F. Lawrence, Z. Wang, C. T. A. Lee, R. Halama, J. M. Warren, R. K. Workman, W. Xu, M. M. Hirschmann, A. M. Larson, S. R. Hart, C. Lithgow-Bertelloni, L. Stixrude, and W. P. Chen (2007), Correlation of seismic and petrologic thermometers suggests deep thermal anomalies beneath hotspots, *Earth and Planetary Science Letters*, *264*(1-2), 308–316, doi:10.1016/j.epsl.2007.10.003.

Crotwell, H. P., T. J. Owens, and J. Ritsema (1999), The TauP Toolkit : Flexible Seismic Travel-time and Ray-path Utilities, *Seismological Research Letters*, *70*, 154–160.

Dahlen, F. A., S.-H. Hung, and G. Nolet (2000), Fréchet kernels for finite-frequency traveltimes–I. Theory, *Geophysical Journal International*, *141*, 157–174, doi:10.1046/j.1365-246X.2000.00070.x.

Dannberg, J., and S. V. Sobolev (2015), Low-buoyancy thermochemical plumes resolve controversy of classical mantle plume concept, *Nature Communications*, *6*, 6960, doi:10.1038/ncomms7960.

Davies, D. R., S. Goes, and H. C. P. Lau (2015), Thermally Dominated Deep Mantle LLSVPs: A Review, in *The Earth's Heterogeneous Mantle: A Geophysical, Geodynamical, and Geochemical Perspective*, edited by A. Khan, pp. 1–530, Springer International, doi:10.1007/978-3-319-15627-9.

Deschamps, F., L. Cobden, and P. J. Tackley (2012), The primitive nature of large low shear-wave velocity provinces, *Earth and Planetary Science Letters*, *349-350*, 198–208, doi:10.1016/j.epsl.2012.07.012.

Deschamps, F., Y. Li, and P. J. Tackley (2015), *Large-Scale Thermo-chemical Structure of the Deep Mantle: Observations and Models*, pp. 479–515, Springer International Publishing, Cham, doi:10.1007/978-3-319-15627-9_15.

Deuss, A. (2009), Global observations of mantle discontinuities using SS and PP precursors, *Surveys in Geophysics*, *30*(4-5), 301–326, doi:10.1007/s10712-009-9078-y.

Deuss, A., S. A. T. Redfern, K. Chambers, and J. H. Woodhouse (2006), The Nature of the 660-Kilometer Discontinuity in Earth's Mantle from Global Seismic Observations of PP Precursors, *Science*, *311*(5758), 198–201, doi:10.1126/science.1120020.

Deuss, A., J. Andrews, and E. Day (2013), Seismic Observations of Mantle Discontinuities and Their Mineralogical and Dynamical Interpretation, in *Physics and Chemistry of the Deep Earth*, edited by S.-i. Karato, 1st ed., Wiley and Sons Ltd.

Dueker, K. G., and A. F. Sheehan (1997), Mantle discontinuity structure from midpoint stacks of converted P to S waves across the Yellowstone hotspot track, *Journal of Geophysical Research*, *102*(B4), 8313, doi:10.1029/96JB03857.

Dziewonski, A. M. (1984), Mapping the lower mantle: Determination of lateral heterogeneity in P velocity up to degree and order 6, *Journal of Geophysical Research: Solid Earth*, *89*(B7), 5929–5952, doi:10.1029/JB089iB07p05929.

Dziewonski, A. M., and D. L. Anderson (1981), Preliminary reference earth model, *Physics of the Earth and Planetary Interiors*, *25*(4), 297–356.

Eagar, K. C., M. J. Fouch, and D. E. James (2010), Receiver function imaging of upper mantle complexity beneath the Pacific Northwest, United States, *Earth and Planetary Science Letters*, *297*(1-2), 141–153, doi:10.1016/j.epsl.2010.06.015.

Efron, B., and R. Tibshirani (1986), Bootstrap methods for standard error, confidence intervals, and other measures of statistical accuracy, *Statistical Science*, *1*(1), 54–75, doi:10.1214/ss/1177013817.

Ekström, G., M. Nettles, and A. M. Dziewoński (2012), The global CMT project 2004 2010 : Centroid-moment tensors, *Physics of the Earth and Planetary Interiors*, *201*, 1–9, doi:10.1016/j.pepi.2012.04.002.

Farnetani, C. G. (1997), Excess temperature of mantle plumes: The role of chemical stratification across D, *Geophysical Research Letters*, *24*(13), 1583, doi:10.1029/97GL01548.

Fee, D., and K. Dueker (2004), Mantle transition zone topography and structure beneath the Yellowstone hotspot, *Geophysical Research Letters*, *31*(18), 1–4, doi:10.1029/2004GL020636.

Flanagan, M. P., P. M. Shearer, and H. Cecil (1998), Global mapping of topography on transition zone velocity discontinuities by stacking SS precursors, *Geophysics*, *103*(97), 2673–2692.

French, S. W., and B. A. Romanowicz (2015), Broad plumes rooted at the base of the Earth's mantle beneath major hotspots, *Nature*, *525*, 95–99, doi:10.1038/nature14876.

Fukao, Y., and M. Obayashi (2013), Subducted slabs stagnant above, penetrating through, and trapped below the 660 km discontinuity, *Journal of Geophysical Research: Solid Earth*, *118*(11), 5920–5938, doi:10.1002/2013JB010466.

Fukao, Y., S. Widiyantoro, and M. Obayashi (2001), Stagnant slabs in the upper and lower mantle transition region, *Reviews of Geophysics*, *39*(3), 291–323.

Gable, C. W., R. J. O. Connell, and B. J. Travis (1991), Convection in Three Dimensions With Surface Plates: Generation of Toroidal Flow, *Journal of Geophysical Research*, *96*(90), 8391–8405.

Gao, S. S., and K. H. Liu (2014), Mantle transition zone discontinuities beneath the contiguous United States, *Journal of Geophysical Research: Solid Earth*, pp. 1–17, doi:10.1002/2014JB011253.1.

Garnero, E. J., A. K. McNamara, and S.-H. Shim (2016), Continent-sized anomalous zones with low seismic velocity at the base of Earth's mantle, *Nature Geoscience*, *9*(7), 481–489, doi:10.1038/ngeo2733.

Goes, S., F. Cammarano, and U. Hansen (2004), Synthetic seismic signature of thermal mantle plumes, *Earth and Planetary Science Letters*, *218*(3-4), 403–419, doi:10.1016/S0012-821X(03)00680-0.

Gokhberg, A., and A. Fichtner (2016), Full-waveform inversion on heterogeneous HPC systems, *Computers and Geosciences*, *89*, 260–268, doi:10.1016/j.cageo.2015.12.013.

Grand, S. P. (1987), Tomographic inversion for shear velocity beneath the North American plate, *Journal of Geophysical Research*, *92*, 14,065–14,090, doi:198710.1029/JB092iB13p14065.

Grand, S. P. (1994), Mantle shear structure beneath the Americas and surrounding oceans, *Journal of Geophysical Research*, *99*(B6), 11,591, doi:10.1029/94JB00042.

Gu, Y. J., and A. M. Dziewonski (2002), Global variability of transition zone thickness, *Journal of Geophysical Research*, *107*(B7), 2135, doi:10.1029/2001JB000489.

Gu, Y. J., A. M. Dziewonski, W. Su, and G. Ekström (2001), Models of the mantle shear velocity and discontinuities in the pattern of lateral heterogeneities, *Journal of Geophysical Research: Solid Earth*, *106*(B6), 11,169–11,199, doi:10.1029/2001JB000340.

Gurrola, H., G. Baker, and J. Minister (1995), Simultaneous time-domain deconvolution with application to the computation of receiver functions, *Geophysical Journal International*, *120*, 537–543.

Herzberg, C., P. Raterron, and J. Zhang (2000), New experimental observations on the anhydrous solidus for peridotite KLB-1, *Geochemistry, Geophysics, Geosystems*, *1*(11), 1051, doi:10.1029/2000gc000089.

Herzberg, C., P. D. Asimow, N. Arndt, Y. Niu, C. M. Lesher, J. G. Fitton, M. J. Cheadle, and A. D. Saunders (2007), Temperatures in ambient mantle and plumes: Constraints from basalts, picrites, and komatiites, *Geochemistry, Geophysics, Geosystems*, *8*(2), doi: 10.1029/2006GC001390.

Hirose, K. (2002), Phase transitions in pyrolitic mantle around 670-km depth: Implications for upwelling of plumes from the lower mantle, *Journal of Geophysical Research: Solid Earth*, *107*(B4), doi:10.1029/2001JB000597.

Houser, C., G. Masters, M. Flanagan, and P. Shearer (2008), Determination and analysis of long-wavelength transition zone structure using SS precursors, *Geophysical Journal International*, *174*(1), 178–194, doi:10.1111/j.1365-246X.2008.03719.x.

Humphreys, E., E. Hessler, K. Dueker, G. L. Farmer, E. Erslev, and T. Atwater (2003), How Laramide-Age Hydration of North American Lithosphere by the Farallon Slab Controlled Subsequent Activity in the Western United States, *International Geology Review*, *45*(7), 575–595, doi:10.2747/0020-6814.45.7.575.

Hung, S.-H., F. A. Dahlen, and G. Nolet (2000), Frénet kernels for finite-frequency traveltimes–II. Examples, *Geophysical Journal International*, *141*(1), 175–203, doi: 10.1046/j.1365-246X.2000.00072.x.

Hung, S.-H., F. A. Dahlen, and G. Nolet (2001), Wavefront healing: a banana–doughnut perspective, *Geophysical Journal International*, *146*, 289–312.

Hwang, Y. K., J. Ritsema, P. E. van Keken, S. Goes, and E. Styles (2011), Wavefront healing renders deep plumes seismically invisible, *Geophysical Journal International*, *187*(1), 273–277, doi:10.1111/j.1365-246X.2011.05173.x.

Irifune, T., and A. E. Ringwood (1993), Phase transformations in subducted oceanic crust and buoyancy relationships at depths of 600-800 km in the mantle, *Earth and Planetary Science Letters*, *117*(1-2), 101–110, doi:10.1016/0012-821X(93)90120-X.

Ishii, M., and J. Tromp (1999), Gravity Constraints on Lateral Variations in Velocity and Density of Earth ' s Mantle, *Science*, *285*(August), 1231–1236.

Jarvis, G. T., and D. P. McKenzie (1980), Convection in a compressible fluid with infinite prandtl number, *Journal of Fluid Mechanics*, *96*(03), 515–583.

Jenkins, J., S. Cottaar, R. S. White, and A. Deuss (2016), Depressed mantle discontinuities beneath Iceland: Evidence of a garnet controlled 660 km discontinuity?, *Earth and Planetary Science Letters*, *433*, 159–168, doi:10.1016/j.epsl.2015.10.053.

Jenkins, J., A. Deuss, and S. Cottaar (2017), Converted phases from sharp 1000 km depth mid-mantle heterogeneity beneath Western Europe, *Earth and Planetary Science Letters*, *459*, 196–207, doi:10.1016/j.epsl.2016.11.031.

Karato, S.-i., and P. Wu (1993), Rheology of the Upper Mantle: A Synthesis, *Science*, *260*(5109), 771–778, doi:10.1126/science.260.5109.771.

Kawakatsu, H., G. Ekström, R. Evans, D. Forsyth, J. Gaherty, B. Kennett, J.-P. Montagner, and H. Utada (2016), Pacific array (transportable broadband ocean floor array), in *EGU General Assembly Conference Abstracts*, vol. 18, p. 2514.

Kind, R., X. Yuan, and P. Kumar (2012), Seismic receiver functions and the lithosphere-asthenosphere boundary, *Tectonophysics*, *536-537*, 25–43, doi:10.1016/j.tecto.2012.03.005.

King, S. D., and J. Ritsema (2000), African hot spot volcanism: small-scale convection in the upper mantle beneath cratons, *Science*, *19*(1), 181–188, doi:10.1177/03063127067078012.

Koelemeijer, P., J. Ritsema, A. Deuss, and H. J. van Heijst (2016), SP12RTS: A degree-12 model of shear- and compressional-wave velocity for Earth's mantle, *Geophysical Journal International*, *204*(2), 1024–1039, doi:10.1093/gji/ggv481.

Koelemeijer, P., A. Deuss, and J. Ritsema (2017), Density structure of Earth's lowermost mantle from Stoneley mode splitting observations, *Nature Communications*, *8*, 15,241, doi:10.1038/ncomms15241.

Komatitsch, D., and J. Tromp (2002), Spectral-element simulations of global seismic wave propagation-I. Validation, *Geophysical Journal International*, *149*, 390–412, doi:10.1046/j.1365-246X.2002.01653.x.

Kumagai, I., A. Davaille, K. Kurita, and E. Stutzmann (2008), Mantle plumes: Thin, fat, successful, or failing? Constraints to explain hot spot volcanism through time and space, *Geophysical Research Letters*, *35*(16), 1–5, doi:10.1029/2008GL035079.

Labrosse, S., J. W. Hernlund, and N. Coltice (2007), A crystallizing dense magma ocean at the base of the Earth's mantle, *Nature*, *450*(7171), 866–869, doi:10.1038/nature06355.

Laske, G., G. Masters, and C. Reif (2001), Crust2. 0: a new global crustal model at $2\times$ 2 degrees, *Institute of Geophysics and Planetary Physics, The University of California, San Diego, website http://mahi. ucsd. edu/Gabi/rem. dir/crust/crust2. html*.

Laske, G., J. A. Collins, C. J. Wolfe, S. C. Solomon, R. S. Detrick, J. A. Orcutt, D. Bercovci, and E. H. Hauri (2009), Probing the Hawaiian hot spot with new broadband ocean bottom instruments, *Eos*, *90*, 362–363, doi:10.1029/2009EO410002.

Lau, H. C. P., J. X. Mitrovica, J. L. Davis, J. Tromp, H.-Y. Yang, and D. Al-Attar (2017), Tidal tomography constrains Earth's deep-mantle buoyancy, *Nature*, *551*(7680), 321–326, doi:10.1038/nature24452.

Lay, T., and B. Buffett (2008), Core–mantle boundary heat flow, *Nature Geoscience*, *1*, 25–32, doi:10.1038/ngeo.2007.44.

Lekić, V., and K. M. Fischer (2017), Interpreting spatially stacked Sp receiver functions, *Geophysical Journal International*, *210*(2), 874–886, doi:10.1093/gji/ggx206.

Leonard, T., and L. Liu (2016), The role of a mantle plume in the formation of Yellowstone volcanism, *Geophysical Research Letters*, *43*(3), 1132–1139, doi:10.1002/2015GL067131.

Li, M., and A. K. McNamara (2013), The difficulty for subducted oceanic crust to accumulate at the Earth's core-mantle boundary, *Journal of Geophysical Research: Solid Earth*, *118*(4), 1807–1816, doi:10.1002/jgrb.50156.

Li, X. H., R. Kind, K. Priestley, S. V. Sobolev, F. Tilmann, X. Yuan, and M. Weber (2000), Mapping the Hawaiian plume conduit with converted seismic waves, *Nature*, *405*, 938–941, doi:10.1038/35016054.

Lin, S.-C., and P. E. van Keken (2005), Multiple volcanic episodes of flood basalts caused by thermochemical mantle plumes., *Nature*, *436*(7048), 250–252, doi:10.1038/nature03697.

Lin, S. C., and P. E. van Keken (2006), Dynamics of thermochemical plumes: 2. Complexity of plume structures and its implications for mapping mantle plumes, *Geochemistry, Geophysics, Geosystems*, *7*(3), doi:10.1029/2005GC001072.

Liu, L., M. Gurnis, M. Seton, J. Saleeby, R. D. Müller, and J. M. Jackson (2010), The role of oceanic plateau subduction in the Laramide orogeny, *Nature Geoscience*, *3*(5), 353–357, doi:10.1038/ngeo829.

Livaccari, R. F., K. Burke, and A. M. C. Sengör (1981), Was the Laramide orogeny related to subduction of an oceanic plateau?, *Nature*, *289*, 276–278, doi:10.1038/289276a0.

Maguire, R., J. Ritsema, P. E. van Keken, A. Fichtner, and S. Goes (2016), P- and S-wave delays caused by thermal plumes, *Geophysical Journal International*, *206*, 1169–1178, doi:10.1093/gji/ggw187.

Maguire, R., J. Ritsema, and S. Goes (2017), Signatures of 660-km topography and compositional heterogeneity in seismic images of upwellings, *Geophysical Research Letters*, pp. 1–19, doi:10.1002/2017GL073120.

Malcolm, A. E., and J. Trampert (2011), Tomographic errors from wave front healing: More than just a fast bias, *Geophysical Journal International*, *185*(1), 385–402, doi:10.1111/j.1365-246X.2011.04945.x.

Mao, Z., J. F. Lin, H. P. Scott, H. C. Watson, V. B. Prakapenka, Y. Xiao, P. Chow, and C. McCammon (2011), Iron-rich perovskite in the Earth's lower mantle, *Earth and Planetary Science Letters*, *309*(3-4), 179–184, doi:10.1016/j.epsl.2011.06.030.

Masters, G., T. H. Jordan, P. G. Silver, and F. Gilbert (1982), Aspherical Earth structure from fundamental spheroidal-mode data, *Nature*, *298*(5875), 609–613, doi:10.1038/298609a0.

McNamara, A. K., and S. Zhong (2005), Thermochemical structures beneath Africa and the Pacific Ocean., *Nature*, *437*(7062), 1136–1139, doi:10.1038/nature04066.

Mercerat, D. E., and G. Nolet (2013), On the linearity of cross-correlation delay times in finite-frequency tomography, *Geophysical Journal International*, *192*, 681–687, doi:10.1093/gji/ggs017.

Montagner, J.-P., and B. L. N. Kennett (1996), How to reconcile body-wave and normal-mode reference earth models, *Geophysical Journal International*, *125*(1), 229–248, doi:10.1111/j.1365-246X.1996.tb06548.x.

Montelli, R., G. Nolet, F. A. Dahlen, G. Masters, E. R. Engdahl, and S.-H. Hung (2004), Finite-frequency tomography reveals a variety of plumes in the mantle., *Science*, *303*, 338–343, doi:10.1126/science.1092485.

Morgan, W. J. (1971), Convection plumes in the lower mantle, *Nature*, *230*, 42–43.

Moulik, P., and G. Ekström (2016), The relationships between large-scale variations in shear velocity, density, and compressional velocity in the Earth's mantle, *Journal of Geophysical Research: Solid Earth*, *121*(4), 2737–2771, doi:10.1002/2015JB012679.

Mrosko, M., M. Koch-Müller, C. McCammon, D. Rhede, J. R. Smyth, and R. Wirth (2015), Water, iron, redox environment: effects on the wadsleyite–ringwoodite phase transition, *Contributions to Mineralogy and Petrology*, *170*(1), 1–12, doi:10.1007/s00410-015-1163-2.

Mulibo, G. D., and A. A. Nyblade (2013), Mantle transition zone thinning beneath eastern Africa: Evidence for a whole-mantle superplume structure, *Geophysical Research Letters*, *40*(14), 3562–3566, doi:10.1002/grl.50694.

Mulyukova, E., B. Steinberger, M. Dabrowski, and S. V. Sobolev (2015), Survival of LLSVPs for billions of years in a vigorously convecting mantle: Replenishment and destruction of chemical anomaly, *Journal of Geophysical Research: Solid Earth*, *120*(5), 3824–3847, doi:10.1002/2014JB011688.

Nakagawa, T., and P. J. Tackley (2014), Influence of combined primordial layering and recycled MORB on the coupled thermal evolution of Earth's mantle and core, *Geochemistry, Geophysics, Geosystems*, *15*(3), 619–633, doi:10.1002/2013GC005128.

Nakagawa, T., P. J. Tackley, F. Deschamps, and J. A. D. Connolly (2010), The influence of MORB and harzburgite composition on thermo-chemical mantle convection in a 3-D spherical shell with self-consistently calculated mineral physics, *Earth and Planetary Science Letters*, *296*(3-4), 403–412, doi:10.1016/j.epsl.2010.05.026.

Nakanishi, I., and D. L. Anderson (1982), Worldwide distribution of group velocity of mantle Rayleigh waves as determined by spherical harmonic inversion, *Bulletin of the Seismological Society of America*, *72*(4), 1185–1194.

Ni, S., E. Tan, M. Gurnis, and D. Helmberger (2002), Sharp sides to the African superplume, *Science*, *296*(5574), 1850–1852, doi:10.1126/science.1070698.

Nissen-Meyer, T., M. Van Driel, S. C. Stähler, K. Hosseini, S. Hempel, L. Auer, a. Colombi, and a. Fournier (2014), AxiSEM: Broadband 3-D seismic wavefields in axisymmetric media, *Solid Earth*, *5*(1), 425–445, doi:10.5194/se-5-425-2014.

Nolet, G., and F. Dahlen (2000), Wave front healing and the evolution of seismic delay times, *Journal of Geophysical Research*, *105*(19), 043–19.

Porritt, R. W., R. M. Allen, and F. F. Pollitz (2014), Seismic imaging east of the Rocky Mountains with USArray, *Earth and Planetary Science Letters*, *402*, 16–25.

Rickers, F., A. Fichtner, and J. Trampert (2012), Imaging mantle plumes with instantaneous phase measurements of diffracted waves, *Geophysical Journal International*, *190*(1), 650–664, doi:10.1111/j.1365-246X.2012.05515.x.

Rickers, F., A. Fichtner, and J. Trampert (2013), The Iceland-Jan Mayen plume system and its impact on mantle dynamics in the North Atlantic region: Evidence from full-waveform inversion, *Earth and Planetary Science Letters*, *367*, 39–51, doi:10.1016/j.epsl.2013.02.022.

Ritsema, J., S. Ni, D. V. Helmberger, and H. P. Crotwell (1998), Evidence for strong shear velocity reductions and velocity gradients in the lower mantle beneath Africa, *Geophysical Journal International*, *25*(23), 4245–4248, doi:10.1029/1998GL900127.

Ritsema, J., H. J. van Heijst, and J. H. Woodhouse (2004), Global transition zone tomography, *Journal of Geophysical Research*, *109*(B2), B02,302, doi:10.1029/2003JB002610.

Ritsema, J., A. K. McNamara, and A. L. Bull (2007), Tomographic filtering of geodynamic models: Implications for models interpretation and large-scale mantle structure, *Journal of Geophysical Research: Solid Earth*, *112*(1), 1–8, doi:10.1029/2006JB004566.

Ritsema, J., A. Deuss, H. J. Van Heijst, and J. H. Woodhouse (2011), S40RTS: A degree-40 shear-velocity model for the mantle from new Rayleigh wave dispersion, teleseismic traveltime and normal-mode splitting function measurements, *Geophysical Journal International*, *184*(3), 1223–1236, doi:10.1111/j.1365-246X.2010.04884.x.

Samuel, H., and D. Bercovici (2006), Oscillating and stagnating plumes in the Earth's lower mantle, *Earth and Planetary Science Letters*, *248*(1-2), 75–90, doi:10.1016/j.epsl.2006.04.037.

Samuel, H., and C. G. Farnetani (2003), Thermochemical convection and helium concentrations in mantle plumes, *Earth and Planetary Science Letters*, *207*(1-4), 39–56, doi:10.1016/S0012-821X(02)01125-1.

Schmandt, B., and F.-c. Lin (2014a), P and S wave tomography of the mantle beneath the United States, *Geophysical Research Letters*, *41*, 6342–6349, doi:10.1002/2014GL061231.

Schmandt, B., K. Dueker, E. Humphreys, and S. Hansen (2012), Hot mantle upwelling across the 660 beneath Yellowstone, *Earth and Planetary Science Letters*, *331-332*, 224–236, doi:10.1016/j.epsl.2012.03.025.

Schmandt, B., S. D. Jacobsen, T. W. Becker, Z. Liu, and K. G. Dueker (2014b), Dehydration melting at the top of the lower mantle, *Science*, *344*(6189), 1265–1268.

Schuberth, B., H.-P. Bunge, and J. Ritsema (2009), Tomographic filtering of high-resolution mantle circulation models: Can seismic heterogeneity be explained by temperature alone?, *Geochemistry, Geophysics, Geosystems*, *10*, doi:10.1029/2009GC002401.

Shearer, P. (2000), Upper mantle seismic discontinuities, in *Earth's Deep Interior: Mineral Physics and Tomography From the Atomic to Global Scale*, pp. 115–131, doi:10.1016/0031-9201(95)03059-6.

Shen, Y., S. C. Solomon, I. Bjarnason, and C. J. Wolfe (1998), Seismic evidence for a lower mantle origin of the Iceland mantle plume, *Nature*, *395*, 62–65.

Sigloch, K. (2012), Mantle provinces under North America from multifrequency P wave tomography, *Geochemistry, Geophysics, Geosystems*, *12*(2), 1–27, doi:10.1029/2010GC003421.

Sigloch, K., and M. G. Mihalynuk (2013), Intra-oceanic subduction shaped the assembly of Cordilleran North America, *Nature*, *496*(7443), 50–56, doi:10.1038/nature12019.

Sigloch, K., N. McQuarrie, and G. Nolet (2008), Two-stage subduction history under North America inferred from multiple-frequency tomography, *Nature Geoscience*, *1*(7), 458–462, doi:10.1038/ngeo231.

Simmons, N. A., and H. Gurrola (2000), Multiple seismic discontinuities near the base of the transition zone in the Earth ' s mantle, *Nature*, *405*, 559–562, doi:10.1038/35014589.

Simmons, N. A., A. M. Forte, L. Boschi, and S. P. Grand (2010), GyPSuM: A joint tomographic model of mantle density and seismic wave speeds, *Journal of Geophysical Research: Solid Earth*, *115*(12), 1–24, doi:10.1029/2010JB007631.

Sleep, N. H. (1990), Hotspots and mantle plumes: Some phenomenology, *Journal of Geophysical Research*, *95*, 6715–6736.

Spakman, W., S. Stein, R. van der Hilst, and R. Wortel (1989), Resolution experiments for NW Pacific subduction zone tomography, *Geophysical Research Letters*, *16*, 1097–1100.

Stixrude, L., and C. Lithgow-Bertelloni (2011), Thermodynamics of mantle minerals - II. Phase equilibria, *Geophysical Journal International*, *184*(3), 1180–1213, doi:10.1111/j.1365-246X.2010.04890.x.

Styles, E., S. Goes, P. E. van Keken, J. Ritsema, and H. Smith (2011), Synthetic images of dynamically predicted plumes and comparison with a global tomographic model, *Earth and Planetary Science Letters*, *311*(3-4), 351–363, doi:10.1016/j.epsl.2011.09.012.

Su, W.-J., R. L. Woodward, and A. M. Dziewonski (1994), Degree 12 model of shear velocity heterogeneity in the mantle, *Journal of Geophysical Research*, *99*(B4), 6945–6980, doi:10.1029/93JB03408.

Tauzin, B., R. D. Van Der Hilst, G. Wittlinger, and Y. Ricard (2013), Multiple transition zone seismic discontinuities and low velocity layers below western United States, *Journal of Geophysical Research: Solid Earth*, *118*(5), 2307–2322, doi:10.1002/jgrb.50182.

Trampert, J. (2004), Probabilistic Tomography Maps Chemical Heterogeneities Throughout the Lower Mantle, *Science*, *306*(5697), 853–856, doi:10.1126/science.1101996.

Trampert, J., and J. Spetzler (2006), Surface wave tomography: Finite-frequency effects lost in the null space, *Geophysical Journal International*, *164*(2), 394–400, doi:10.1111/j.1365-246X.2006.02864.x.

Tsuchiya, T. (2011), Elasticity of subducted basaltic crust at the lower mantle pressures : Insights on the nature of deep mantle heterogeneity, *Physics of the Earth and Planetary Interiors*, *188*(3-4), 142–149, doi:10.1016/j.pepi.2011.06.018.

van der Hist, R., R. Engdahl, W. Spakman, and G. Nolet (1991), Tomographic imaging of subducted lithosphere below northwest pacific island arcs, *Nature*, *353*(6339), 37.

van der Lee, S., and G. Nolet (1997), Seismic image of the subducted trailing fragments of the Farallon plate, *Nature*, *386*(6622), 266–269, doi:10.1038/386266a0.

van Summeren, J. R. G., A. P. van den Berg, and R. D. van der Hilst (2009), Upwellings from a deep mantle reservoir filtered at the 660 km phase transition in thermo-chemical convection models and implications for intra-plate volcanism, *Physics of the Earth and Planetary Interiors*, *172*(3-4), 210–224, doi:10.1016/j.pepi.2008.09.011.

Vinnik, L. (1977), Detection of waves converted from P to SV in the mantle, *Physics of the Earth and Planetary Interiors*, *15*(1), 39–45, doi:10.1016/0031-9201(77)90008-5.

Wang, H., M. Gurnis, and J. Skogseid (2017), Rapid Cenozoic Subsidence in the Gulf of Mexico Resulting From Hess Rise Conjugate Subduction, *Geophysical Research Letters*, *44*(21), 10,930–10,938, doi:10.1002/2017GL074959.

Wang, X., and F. Niu (2011), Imaging the mantle transition zone beneath eastern and central China with CEArray receiver functions, *Earthquake Science*, *24*(1), 65–75, doi:10.1007/s11589-011-0770-x.

Waszek, L., N. C. Schmerr, and M. D. Ballmer (2018), Global observations of reflectors in the mid-mantle with implications for mantle structure and dynamics, *Nature Communications*, *9*(1), 385, doi:10.1038/s41467-017-02709-4.

Weidner, D. J., and Y. Wang (1998), Chemical-and clapeyron-induced buoyancy at the 660 km discontinuity, *Journal of Geophysical Research: Solid Earth*, *103*(B4), 7431–7441.

Weinstein, S. A. (1992), Induced compositional layering in a convecting fluid layer by an endothermic phase transition, *Earth and Planetary Science Letters*, *113*(1-2), 23–39, doi:10.1016/0012-821X(92)90209-E.

Wilson, J. T. (1963), A possible origin of the hawaiian islands, *Canadian Journal of Physics*, *41*(6), 863–870.

Wolfe, C. J., I. T. Bjarnason, J. C. VanDecar, and S. C. Solomon (1997), Seismic structure of the Iceland mantle plume, *Nature*, *385*, 245–247, doi:10.1038/385245a0.

Wolfe, C. J., S. C. Solomon, G. Laske, J. a. Collins, R. S. Detrick, J. a. Orcutt, D. Bercovici, and E. H. Hauri (2009), Mantle shear-wave velocity structure beneath the Hawaiian hot spot., *Science*, *326*(5958), 1388–1390, doi:10.1126/science.1180165.

Woodhouse, J. H., and A. M. Dziewonski (1984), Mapping the upper mantle: Three-dimensional modeling of earth structure by inversion of seismic waveforms, *Journal of Geophysical Research: Solid Earth*, *89*(B7), 5953–5986, doi:10.1029/JB089iB07p05953.

Workman, R. K., and S. R. Hart (2005), Major and trace element composition of the depleted MORB mantle (DMM), *Earth and Planetary Science Letters*, *231*(1-2), 53–72, doi:10.1016/j.epsl.2004.12.005.

Xie, S., and P. J. Tackley (2004), Evolution of helium and argon isotopes in a convecting mantle, *Physics of the Earth and Planetary Interiors*, *146*(3-4), 417–439, doi:10.1016/j.pepi.2004.04.003.

Xu, W., C. Lithgow-Bertelloni, L. Stixrude, and J. Ritsema (2008), The effect of bulk composition and temperature on mantle seismic structure, *Earth and Planetary Science Letters*, *275*(1-2), 70–79, doi:10.1016/j.epsl.2008.08.012.

Xue, J., Y. Zhou, and Y. Chen (2015), Tomographic resolution of plume anomalies in the lowermost mantle, *Geophysical Journal International*, *201*, 979–995, doi:10.1093/gji/ggv067.

Ye, Y., C. Gu, S.-h. Shim, Y. Meng, and V. Prakapenka (2014), The postspinel boundary in pyrolitic compositions determined in the laser-heated diamond anvil cell, *Geophysical Research Letters*, pp. 3833–3841, doi:10.1002/2014GL060060.1.

Zerr, A., and A. Diegeler (1998), Solidus of Earth's Deep Mantle, *Science*, *281*, 243–246, doi:10.1126/science.281.5374.243.

Zhao, C., E. J. Garnero, A. K. McNamara, N. Schmerr, and R. W. Carlson (2015), Seismic evidence for a chemically distinct thermochemical reservoir in Earth's deep mantle beneath Hawaii, *Earth and Planetary Science Letters*, *426*, 143–153, doi: 10.1016/j.epsl.2015.06.012.